Treatment planning in electroporation-based therapies

Enric Perera Bel

DOCTORAL THESIS UPF / year 2021

THESIS SUPERVISORS
Prof. Miguel Ángel González Ballester
Prof. Antoni Ivorra Cano
Department of Information and Communication Technologies

This work was carried out in the Department of Information and Communication Technologies (DTIC) at Universitat Pompeu Fabra (UPF), Barcelona, Spain.

Enric Perera Bel was supported by the Spanish Ministry of Economy and Competitiveness under the Programme for the Formation of Doctors (grant number BES-2017-081164).

The work done within this thesis was supported by the Spanish Ministry of Economy and Competitiveness (grant number TEC2014-52383-C3-2-R) and the María de Maeztu Units of Excellence Programme (grant number MDM-2015-0502), and by the State Research Agency of the Spanish government (grant number PID2019-110120RB-I00 / AEI / 10.13039/501100011033).

Acknowledgments

First of all I would like to express my gratitude to my supervisors Prof. Antoni Ivorra and Prof. Miguel Ángel González Ballester for their help at any time during the thesis, and for keeping me motivated and positive. Their guidance, advice and careful editing have greatly contributed in the production of this thesis.

I would also like to thank my colleagues at SIMBIOSys, BERG, and PhySense research groups for the nice working environment and for the shared moments, physically and virtually. Special thanks to Carlos and Borja, who really helped me at different stages of the PhD.

At last, I would like to thank all my friends, from the ones I have known for years to the ones I met during the PhD, and my family, Júlia, Aurora and Joan. And specially thanks to Marta, who kept me smiling in the good and the bad days.

Abstract

Tissue electroporation is the basis of several therapies. Among others, it is used in treatments of solid tumors. Because electroporation exclusively targets cells and leaves the extracellular matrix unaffected, tumor treatment near vital structures is feasible, which is a clear advantage over other therapies based on physical methods. However, careful treatment planning is required because electroporation is highly dependent on procedure parameters and tissue properties.

This thesis focuses on the development of tools and models for treatment planning in electroporation-based therapies, specifically, for the treatment of internal tumors. The contributions of this thesis are as follows. First, the development of a web platform which illustrates the strong dependence of electroporation on treatment parameters and tissue electrical properties is described. Namely, the dependence on electrode number and positioning, voltage applied between electrode pairs, and tissue electrical conductivity. Second, models which describe cell are presented to predict treatment outcome in cases of treatment overlap with multiple electrode pairs, which are frequent in electroporation-based therapies. This study was performed by first characterizing the cell death models with overlapping treatments, and then, using these models to analyze how the treatment volume was affected in electroporation-based therapies. Third, a platform for treatment planning in electroporation-based therapies is presented. The optimal electrode insertion path can be planned preoperatively by simulating the predicted treatment volume on accurate patient-specific models in an easy-to-use and fast way.

Resum

Diverses teràpies mèdiques es basen en l'electroporació. Entre d'altres, l'electroporació s'usa per al tractament de tumors sòlids. Com que només afecta les cèl·lules i la matriu extracel·lular queda intacta, amb l'electroporació es poden tractar tumors propers a teixits vitals. Tot i aquest clar avantatge respecte d'altres teràpies físiques, els tractaments s'han de planificar amb precisió perquè el resultat és altament dependent dels paràmetres del procediment i de les propietats dels teixits.

Aquesta tesi se centra en el desenvolupament d'eines i models per a la planificació de tractaments amb teràpies basades en electroporació, concretament, per al tractament de tumors interns. A continuació, es relacionen les aportacions d'aquesta tesi. Primer, es descriu el desenvolupament d'una plataforma web que il·lustra la forta dependència de l'electroporació dels paràmetres del tractament i de les propietats elèctriques del teixit, en particular, la dependència del nombre i posició dels elèctrodes, el voltatge aplicat entre parells d'elèctrodes i la conductivitat elèctrica del teixit. Segon, s'estudien models que descriuen la mort cel·lular per predir el volum electroporat en casos de superposició de tractaments amb múltiples parells d'elèctrodes, cosa freqüent en les teràpies basades en electroporació. Per a aquest estudi, es van superposar tractaments per caracteritzar els models de mort cel·lular i, després, aquests models es van usar per analitzar fins a quint punt el volum del tractament es veu afectat en teràpies basades en electroporació. Tercer, es presenta una plataforma per a la planificació de tractaments amb teràpies basades en electroporació. La inserció òptima dels elèctrodes pot ser planificada preoperativament simulant el volum del tractament en models precisos específics per a cada pacient de forma senzilla i ràpida.

Contents

Acronyms and abbreviations

3SE three times the standard error

API application programming interface

AUC area under the curve

Cl^- chloride ion

CT computed tomography

DB data base

DMEM Dulbeccos Modified Eagle Medium

CHO chinese hamster ovarian

CTV clinical target volume

DC direct current

ECT electrochemotherapy

EGT electrogene therapy

E2 electrolytic electroporation

FDM finite differences method

FEM finite elements method

GTV gross tumor volume

GUI graphical user interface

HCC hepatocellular carcinoma

H-FIRE high-frequency irreversible electroporation

IRE irreversible electroporation

K^+ potassium ion

MRI magnetic ressonance imaging

Na^+ sodium ion

NFS network file system

NTIRE non-thermal irreversible electroporation

PET positron emission tomography

PFA pulsed field ablation

PI propidium iodide

PTV planning target volume

RE reversible electroporation

ROC receiver operating characteristic

ROI region of interest

TMV transmembrane voltage

TV treatment volume

VS volume similarity

Chapter 1

INTRODUCTION

1.1 Overview

Cancer is responsible for one out of six deaths worldwide. In 2018, more than 18.1 million cancer cases were diagnosed, causing 9.6 million deaths. Future perspectives are alarming; the number of cases is expected to grow up to 30 million by 2040, as a result of an increase in life expectancy and epidemiological and demographic transitions [1].

In adults, around 90% of cancers manifest as solid tumors [2]. Surgical resection is usually the recommended therapy for this type of cancer. The intervention consists of excising the tumor and a surrounding margin of healthy tissue to ensure full eradication of malignant cells. Typically, it is combined with a secondary adjuvant treatment such as chemotherapy or radiotherapy to maximize success [3, 4]. Unfortunately, it is not uncommon for the tumor to grow near vital structures, making surgery unsuitable. In such cases, patients are simply treated with chemotherapy or radiotherapy, hoping that the tumor will reduce in size so it can latter be resected.

In addition to surgical resection, several focal therapies are used in the treatment of tumors. One of this therapies is thermal ablation. Thermal ablation consists of heating tissues to 50-54°C for 4 to 6 minutes to induce coagulation necrosis of the tumor tissue [5–8]. Alternatively, thermal damage can also be evoked by cooling the tissue to -20°C for a minute in a procedure known as cryoablation [9]. Chemical ablation is another focal therapy in which a cytotoxic substance such as ethanol or acetic acid is introduced in the tumor which causes dehydration followed by tissue necrosis [5, 10].

In these therapies, thin needle-shaped actuators are typically used which allow minimally invasive percutaneous procedures [11, 12]. Compared to surgical resection where open surgery is usually required, ablation procedures are, in general, faster, present less side effects, and the hospital stay is shorter [13–17]. However, neither thermal nor chemical ablation are suitable for tumors adjacent to vital structures such as vessels or bile ducts, as the extracellular matrix (i.e., the tissue) is denatured [8, 18].

Electroporation is a phenomenon that affects the cell membrane by transitorily or permanently increasing its permeability to ions and macromolecules when the cell is exposed to high electric fields. As an alternative to the aforementioned ablation procedures, in electroporation-based therapies, electrical damage is induced to the cell membrane which increases its permeability to ions and macromolecules. Two outcomes can be defined: reversible electroporation, when the membrane recovers after field exposure and the cell remains viable, and irreversible electroporation, which causes cell death due to homeostasis loss, even if the membrane is capable of resealing. Both effects are the basis of therapies for solid tumor eradication. First, in electrochemotherapy (ECT), a chemotherapeutic agent is introduced to the tissue which can then penetrate into the cell thanks to the increased membrane permeability of reversible electroporation [19]. Second, with irreversible electroporation it is possible to ablate the malignant tissue, in a therapy known as non-thermal irreversible electroporation (NTIRE) [20].

Because electroporation exclusively targets the cell membrane, the extracellular matrix is left unaffected [21]. Even if cells that belong to critical structures are ablated, the preservation of tissue allows re-population of healthy cells in a matter of weeks [22, 23]. Thus, electroporation-based therapies are a promising alternative when surgical resection or other ablation therapies are unfeasible.

However, even though electroporation therapies have been around for more than twenty years, they have yet to be included in standard clinical practice for the treatment of internal tumors. Electroporation interventions are complex because they require between 2 and 6 needle electrodes to cover the whole treatment volume, as the electrodes must be placed closely (2 cm) to generate the required high electric fields [24]. In comparison, the same volume can be treated with a single electrode with radiofrequency thermal ablation. In addition, the treatment volume is highly dependent on the number of electrodes, their relative position, the applied voltage, and the type of tissue. Therefore, accurate treatment planning is required to preoperatively assess lesion size and shape in order to ensure treatment efficacy and safety [25, 26].

Patient-specific treatment planning is a multi-step process [27]. First, the target volume must be identified from medical images. From the same images, tissues are delineated (segmented) to generate a heterogeneous 3D model which represents patient anatomy. The actuators are then virtually inserted into the model, the treatment parameters are defined, and the treatment volume is simulated. Finally, it is assessed if the simulated treatment volume is enclosing the target volume. Otherwise, treatment parameter can be modified and the treatment can be simulated again. For practical reasons, it is important that all these steps are included in a single platform. Regrettably, this is rarely the case.

Electroporation-based therapies are a promising alternative to conventional focal ablation procedures when these are unsuitable. The non-thermal action mechanism of electroporation is key to treat tumors near vital structures. In recent years, research in treatment planning has helped

to increase the use of electroporation in clinical practice [25, 28]. However, clinicians have to deal with multiple tools to perform all the steps, which is far from optimal. Within this context, a platform that integrates all the required tools could encourage the use of electroporation-based therapies.

1.2 Research goals

The scope of this thesis was to contribute to the development of treatment planning methodologies and tools for electroporation-based therapies, specifically for tumor ablation with irreversible electroporation.

The volume that will be effectively treated in electroporation-based therapies is typically predicted by computing the electric field distribution and by determining the region whose electric field magnitude surpasses a threshold. This approach has been successfully demonstrated in many studies. However, it is not straightforward to calculate the electric field distribution when using needle electrodes, even if the tissue is considered to be completely homogeneous. The electric field distribution that results when voltages are applied across electrodes is non uniform and highly dependent on the number of electrodes, their position, the voltage applied between pairs of electrodes, and the type of tissue. A first goal of this thesis was to develop an open web platform that provides a good initial estimate of the electric field distribution to illustrate such dependencies for students, researchers and clinicians. This tool assumes that treatment is delivered to a homogeneous tissue.

However, biological tissues are heterogeneous and the field distribution is further modified. In order to accurately predict the treatment volume in electroporation therapies, a more complex model is needed which accounts for the different electrical properties of tumor, healthy tissue, and other surrounding structures. Thus, the main goal of this thesis

was to develop a platform to generate patient-specific models where the treatment volume can be accurately predicted. That is, a platform for treatment planning in electroporation-based therapies.

Treatment of large tumors is achieved in electroporation-based therapies by delivering multiple treatments across pairs of electrodes. Typically, up to six or seven electrodes are required. During the conception of the treatment planning platform, it was noticed that current treatment planning methodologies and tools for electroporation-based therapies consider that there is no interaction between the different electrodes pairs, and that the overall treatment volume can be obtained as the geometric union of individual single-pair treatments. Therefore, a secondary goal of this thesis was to quantify the interaction between pairs, that is, to model treatment overlap in electroporation-based therapies.

1.3 Dissertation outline

Chapter 2 provides an overview of the effects of electric fields on biological tissues and the electroporation phenomenon. The clinical applications of electroporation are presented, and it is explained how treatment planning must be approached for such therapies.

Chapter 3 presents the web-platform that was developed to illustrate how treatment parameters affect the electric field distribution in electroporation-based therapies. Specifically, the dependence on electrode number and location, voltage, and tissue properties.

Next, chapter 4 describes the *in vitro* study where cell death due to treatment overlap in multiple-pair scenarios was characterized. This chapter explores how cell death is influenced by treatment overlap, how it can be modeled, and how the treatment volume is affected in electroporation-based therapies.

The main contribution of this thesis, the platform for treatment planning in electroporation-based therapies, is presented in Chapter 5. With this platform, a heterogeneous, patient-specific, model is generated from medical images, and the electroporation volume is simulated to ensure full coverage of the malignant tissue. An overview of the whole platform is provided, from development to case of use and validation.

At last, chapter 6 overviews the main contributions and conclusions of this thesis and suggests future lines of work.

Chapter 2

BACKGROUND

2.1 Electric fields in biological tissue

Biological tissues are highly complex with highly heterogeneous structures. However, viewed from an physicochemical perspective, tissues can be simplified as cells embedded in an ionic aqueous solution, that is, an electrolyte solution [29]. Under the application of an electric field, an electric force is exerted on the ions. Because ions can freely move in the aqueous solution, an ionic flow (i.e., electric current) is induced [30]. Thus, biological tissues are electrical conductors.

The aqueous solution in which the cells are contained is the main constituent of the extracellular medium. The intracellular medium also mostly consists of an aqueous solution. Whereas the intracellular medium primary contains potassium ions (K^+), in the extracellular medium sodium (Na^+) and chloride (Cl^-) ions prevail [31]. The two media are separated by the cell membrane, which is made of a dual layer of phospholipids facing each other, known as the lipid bilayer. Due to the hydrophobic nature of lipids, the membrane is usually impermeable

to water and ions. Nonetheless, it contains mechanisms that allow water and ion transfer to maintain cell homeostasis [32, 33].

In normal physiological conditions, the extracellular medium contains slightly more positively charged ions than the intracellular medium. This imbalance of charges generates transmembrane voltage (TMV) of a few tenths of millivolts, known as the rest TMV [34]. However, when an external electric field is applied, positively charged ions are driven in the direction of the field, and negative ions in the opposite direction. Because ions cannot cross the cell membrane, charges of opposite sign accumulate at each side. Thus, the membrane polarizes and an abnormal TMV is induced [35].

Artificially increasing the TMV can evoke some physiological responses. Excitable cells, such as neurons, contain ion channels in the cell membrane that are sensitive to the TMV. When a certain TMV threshold is reached (around 20 to 55 mV) the membrane depolarizes and an action potential is induced [36, 37]. Thus, artificially increasing the TMV in neurons can lead to triggering nerve impulses which lead to sensations, including pain, and muscle contractions [38].

The electroporation phenomenon is another possible consequence of increasing the magnitude of the TMV by a high external electric field. This effect is evoked when the magnitude of the TMV surpasses a threshold between 0.2 and 1 V [39]. Electroporation is the phenomenon where cell membrane permeability to ions and macromolecules is increased [40–42]. Although the exact mechanisms of action are not yet fully understood, recent findings support the hypothesis that simple nanometric pores are created in the cell membrane, at least during the first stages of the process [43,44]. Once the electric field ceases, the pores are rapidly resealed, but some membrane defects persist which keeps the permeability high for seconds and even minutes [45–48].

The delivery of electric currents through electrodes to induce electric field in tissues and thus cause electroporation is accompanied by

two physicochemical effects that are relevant for this dissertation: electrochemical reactions and heating.

First, the electric fields are generated by applying a voltage difference between two electrodes. The electric charges flowing through them are electrons, compared to tissue current which is driven by ion movement. When direct current (DC) voltages are applied across electrodes, electrolysis takes place at the electrode-tissue interface, or otherwise, electric current would not flow [49, 50]. In biological tissues, the main reactions that occur at the anode are water decomposition into oxygen gas and hydrogen ions, and chloride ion oxidation which forms chlorine gas.

$$2\mathrm{H_2O} \longrightarrow \mathrm{O_2} + 4\mathrm{H^+} + 4\mathrm{e^-}$$

$$2\mathrm{Cl^-} \longrightarrow \mathrm{Cl_2} + 2\mathrm{e^-}$$

At the cathode, water molecules decompose into hydrogen gas and hydroxide ions.

$$2\mathrm{H_2O} + 2\mathrm{e^-} \longrightarrow \mathrm{H_2} + 2\mathrm{OH^-}$$

These chemical reactions modify the pH: at the anode, oxygen gas acidifies the solution, whereas at the cathode, the medium becomes more alkaline due to the presence of hydroxides. Other oxidation reactions can take place depending on the electrode material, which releases metallic ions [51].

Another reaction that occurs as a consequence of the induced electric currents is Joule heating [52, 53]. Biological tissues, like many other materials, are not perfect electrical conductors. That is, they present an intrinsic resistance to electric current flow. Thus, heat is generated because of charge friction and collision with the media.

2.2 Electroporation

Electroporation is the phenomenon that increases cell membrane permeability to ions and macromolecules when the cell is exposed to high electric fields. Typically, field exposure is brief to prevent excessive Joule heating and it is in the form of pulses. [54]. Two outcomes are defined for the electroporation phenomenon. First, a transient one where the cell membrane recovers after the application of the electric field and the cell remains viable, known as reversible electroporation (RE). Second, irreversible electroporation (IRE) results in cell death due to homeostasis loss, even if the membrane is capable of resealing [55]. Whether the effect is reversible or not depends on the electric field magnitude. RE is induced by surpassing a certain threshold, whereas IRE occurs once a higher threshold is reached. The other characteristics of the exposure, such as the duration of the pulses, the number of pulses, and the repetition frequency modifies such thresholds. Namely, longer pulses, more pulses, or shorter inter-pulse pause, reduce the thresholds for both reversible and irreversible electroporation [56–61].

This section explores the field of electroporation. First, it explains how the cell membrane reacts under electroporation and which physical changes are thought to occur. Second, modeling methods of electroporation are reported for research and for clinical applications. Finally, it is explained how the phenomenon is used in clinical practice.

2.2.1 Electroporation dynamics

As previously explained in section 2.1, electroporation occurs when the cell TMV is artificially increased by means of an external electric field. In general, surpassing a TMV threshold of 0.2 to 1 V is required for electroporation to take place [39]. Such threshold depends on the type of waveform (pulse number, duration and repetiton frequency) that is

applied, and on how electroporation is measured (e.g., by measuring the uptake of a specific molecule or by analyzing cell death) [39]. Although the exact mechanisms of action are not yet fully understood, this section explains the most accepted theories based on recent findings, both experimental and by means of molecular dynamics simulations.

Triggered by the onset of the pulse, charges rapidly accumulate at each side of the membrane (Fig. 2.1 — before electroporation). In a few nanoseconds, electroporation phenomenon takes place and membrane electrical conductiy increases. This first effect is thought to be a simple pore formation due to membrane rearrangement (Fig. 2.1 — during electroporation) [43]. Such pores allow ion trespassing, which increases electrical conductivity. Subsequently, electrical conductivity keeps rising but at a slower pace, as the pore formation gets stabilized. It has been suggested that some of the pores transition into stable pores [44]. In addition, a second population of defects is generated in the membrane due to structural mismatches in the lipid bilayer [62–64]. A possible explanation of these defects is lipid peroxidation [65].

Once the electric pulse ceases, the pores rapidly shrink in microseconds or in very few milliseconds [61, 66]. As a consequence, the electrical conductivity quickly drops in that time span. After the sudden pore shrink, slower resealing processes take place which reduce conductivity to pre-electroporation values [63, 66–68]. Additionally, in tissues, electrical conductivity varies after the application of the pulses, due to osmotic imbalances and cell swelling caused by the increased permeability due to electroporation [39, 69].

Although the conductivity drops rapidly after the electric field ceases, cell membrane remains permeable to molecules for seconds and even minutes [45–48]. In fact, total ion uptake is higher after the pulses [48, 70–77]. After the rapid pore reseal, other membrane structural defects persist which allow molecule diffusion (Fig. 2.1 — after electroporation) [68, 78].

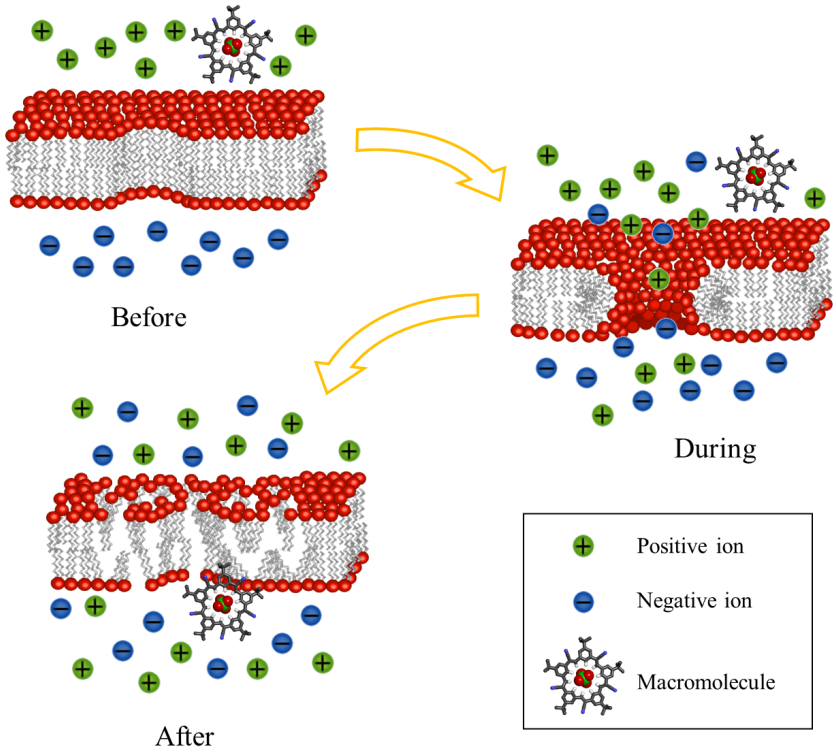

Figure 2.1: Schematic representation of the membrane states before, during, and after electroporation. Before electroporation, the membrane is impermeable to ions and macromolecules. During the application of pulses, the membrane rearranges into pores where ions can cross and the conductivity rises. After the pores reseal, the conductivity drops because ions cannot cross as freely, but membrane defects persist allowing the diffusion of macromolecules. Adapted from "Pore schematic" by MDougM (*https://commons.wikimedia.org/wiki/File:Pore_schematic.svg*).

2.2.2 Electroporation modeling

Electroporation is a phenomenon that occurs at the cell level when a TMV is surpassed. However, in tissues, which are composed of numerous

densely packed cells with complex geometries, it is impractical to evaluate electroporation at the cell level. Instead, it is assumed that the combination of microscopic elements results in homogeneous properties at a macroscopic scale. Thus, tissue electroporation occurs when the macroscopic electric field surpasses a threshold. The field distribution can be simulated with numerical methods [79–81].

Tissue electrical properties for electroporation modeling

As explained in section 2.1, biological tissues can be simplified regarding their passive electrical properties. Cells are embedded in an extracellular aqueous solution, which is electrically conductive. The intracellular medium is also an electrical conductor, but both media are separated by the dielectric cell membrane. Every infinitesimal patch of the extracellular and intracellular media can be represented as a resistance, whereas every infinitesimal paatch of the membrane acts as a capacitance [82]. From circuit theory, all elements can be combined into an equivalent single cell circuit model formed by a resistance (intracellular medium) in series with a capacitance (cell membrane), and these two in parallel with another resistance (extracellular medium) (Fig. 2.2).

This single cell circuit can be extrapolated to a whole tissue. In the same way that the infinitesimal parts of the three components were combined to form an equivalent circuit, multiple single cell circuits can be stacked together [82, 83]. Again, a simplification is obtained thanks to circuit theory, and the same structure as in the single cell model remains (Fig. 2.3). Although the electrical components represent the same elements (i.e., intracellular and extracellular media, and cell membrane), they take different values because they represent the macroscopic properties of the tissue.

The equivalent circuit model represents accurately tissues in most

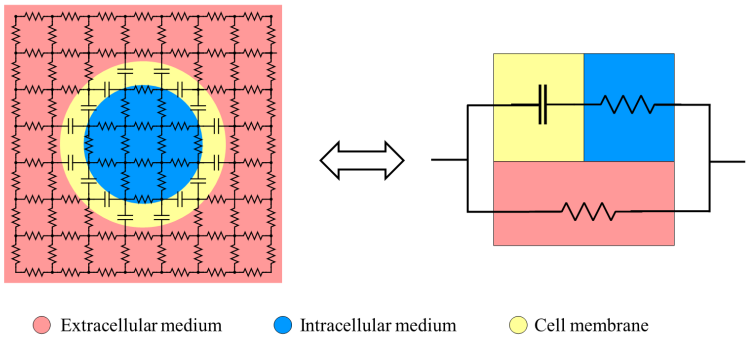

Figure 2.2: Equivalent circuit model of a single cell. All the infinitesimal portions of the extracellular medium are combined in a single resistance. It is in parallel with a capacitance (representing the membrane permittivity) which is in series with a resistance (for the intracellular medium). Adapted from [39].

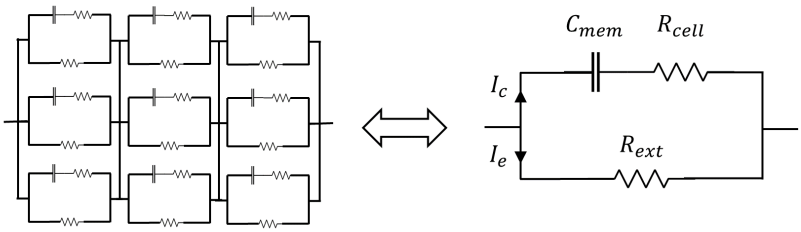

Figure 2.3: Equivalent circuit model of biological tissues. Electric current can either flow through the extracellular medium (I_e) or through cells (I_c). In the former, the properties are only resistive (R_{ext}). Instead, the cell path contains a resistive component (i.e., the intracellular medium, R_{cell}) and a capacitor (i.e., membrane, C_{mem}).

conditions. However, during electroporation, cell membrane becomes permeable, which implies that ions can cross it. That is, the membrane is electrically conductive. To account for this effect, a variable resistance is added in parallel to the membrane capacitor (Fig. 2.4) [84, 85]. The

conductance of this resistance is null in normal conditions, but during electroporation it rises.

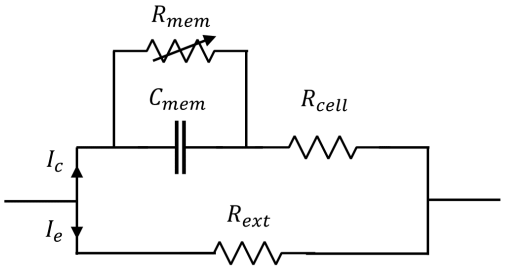

Figure 2.4: Equivalent circuit model of biological tissues accounting for the electroporation phenomenon. Because the cell membrane is conductive during electroporation (i.e., electric current flows through it), a variable resistance R_{mem} is added in parallel to the membrane capacitance C_{mem} (Fig. 2.2). The value of R_{mem} is infinite before electroporation, but it lowers as a function of the number and size of pores.

The behavior of this circuit is frequency dependent due to the presence of the capacitor C_{mem}. Standard electroporation protocols apply a series of short DC square pulses. At the beginning of the pulse, a peak in electric current appears which lasts hundreds of nanoseconds or a few microseconds because of cell membrane charging. For the remaining pulse duration, electric current only flows through the extracellular medium (R_{ext}) and, if electroporation was induced, current also flows through the cell ($R_{cell} + R_{mem}$). Thus, for DC pulses, membrane capacitance behaves as an open circuit [84]. The three remaining resistances are simplified as a single variable resistance ($R_{eq} = (R_{cell} + R_{mem})||R_{ext}$), whose value depends on the electroporation phenomenon [86].

Resistance is a magnitude that depends on material electrical properties (i.e., electrical conductivity) and its geometry. If we consider that R_{eq}

represents an infinitesimal patch of tissue, the resistance can be simply described by tissue electrical conductivity (σ), and, because R_{eq} depends on the electroporation phenomenon, so does its electrical conductivity.

The dependence of tissue conductivity on the electroporation phenomenon can be expressed as a dependence on the applied electric field magnitude, that is $\sigma(|E|)$. For electric fields far below the electroporation threshold (i.e., no electroporation) the electrical conductivity of R_{eq} is that of the extracellular medium. But as cells become electroporated at higher electric fields, the electrical conductivity rises as electric current can additionally flow through cells.

The conductivity of R_{eq} can be experimentally characterized [87, 88]. A pulse with a known voltage is applied and the electric current is measured, from which the electrical conductivity can be derived using Ohm's law. The electric current induced by a pulse is displayed in Fig. 2.5. If the voltage is not high enough to induce electroporation, the electric current stabilizes at a constant value after the initial membrane charging peak (see Fig. 2.5 blue trace). In this situation, current flows exclusively through the extracellular medium (I_e) and the base conductivity can be computed. Instead, if the membrane gets electroporated due to the application of higher voltages, the electric current rises after the initial peak. This is a consequence of electroporation, which allows electric conduction through the cell membrane (I_c). The electric current rapidly increases to the evolution of the electroporation phenomenon but soon exhibits saturation (see Fig. 2.5 orange trace). The saturation current is used to derive the maximum conductivity of the tissue. It has been observed that the electrical conductivity can rise up to three times, although in some tissues, such as skin, it can rise up to 20 times [39, 89–95]. The transition from the base conductivity to its maximum value is usually modeled by a sigmoid function (Fig. 2.6) [25, 84, 96–98], and, although the shape factor can be inferred experimentally as well, it is not as trivial [99].

Finally, electrical conductivity is also affected by tissue temperature. During the application of the pulses, the tissue gets heated as a

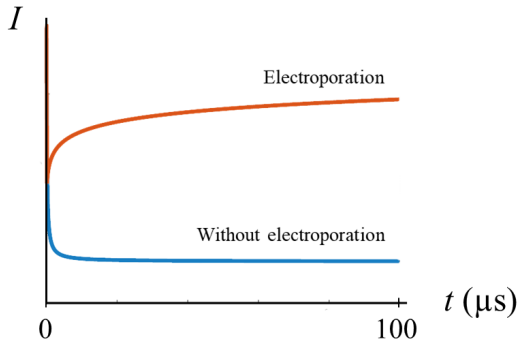

Figure 2.5: Electric current during a 100 μs pulse during electroporation (orange) and without (blue). After the high initial peak due to membrane charging, the current drops and stabilizes when electroporation does not occur. Instead, the current rises logarithmically due to the pore formation during electroporation. Adapted from [39].

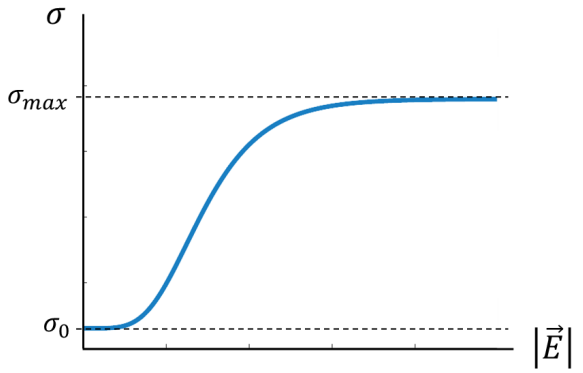

Figure 2.6: Sigmoid approximation of the electrical conductivity of a tissue as a function of the electric field magnitude. Without electroporation, conductivity only flows through the extracellular medium (σ_0). As the electric field increases, the conductivity rises up to σ_{max} because ions can flow through the membrane.

consequence of Joule heating [100]. In electrolyte solutions (e.g., tissues), the mobility of ions is facilitated by higher temperatures, thus, the electrical conductivity rises. For physiological fluids, it is estimated that the conductivity rises 2 % every degree Celsius [101]. In general, the heat generation is small and it can be ignored. However, in IRE, where a large amount of pulses with very high voltages are applied, the temperature increment is not negligible [60]. For needle-shaped electrodes, the heat generation is larger around the electrodes, where the current density is the highest.

Simulation of the electroporation volume

The standard methodology to determine the electroporation volume consists of simulating the stationary electric field distribution to obtain the tissue subjected to an electric field magnitude above an electric field threshold. Typically, numerical models such as finite elements method (FEM) are required to simulate the complex tissues and/or electrode geometries.

The electric field distribution is simulated by solving the Laplace equation for electric currents with charge conservation:

$$\nabla \cdot \sigma \nabla \phi = 0 \tag{2.1}$$

where ϕ is the electric potential, and σ is the electrical conductivity [102]. By solving this equation, the electric field $\vec{E}$ can be obtained from the potential distribution with:

$$\vec{E} = -\nabla \phi \tag{2.2}$$

Notice that eq. (2.1) depends on the electrical conductivity σ. In the previous section it was explained that tissue conductivity during electroporation follows a non-linear sigmoid function which depends on the electric field (see Fig. 2.6). This dependency should not be

overlooked, as the electric field redistribution due to conductivity changes has a major impact on the overall electroporation volume [87,95,99,103]. Then, the electric field must be obtained iteratively, as conductivity and electric field depend of one another.

Dirichlet boundary conditions are used for the active electrodes by setting the corresponding voltage difference. If more than two electrodes are used, the floating potential boundary condition should be used for the inactive electrodes. It imposes that the electric potential at the whole surface of the electrode is constant with the condition that the total net flux through the electrode is zero [104, 105].

The electric field distribution is simulated for each electrode pair. If more than two were simulated, the overall electric field distribution is obtained by combining the maximum computed field from all individual pairs. At last, the electroporation volume is determined by obtaining the tissue whose simulated electric field magnitude surpasses an electric field threshold.

Computing the probability of cell survival

One of the main limitations of the thresholding method is that, for a given tissue, a different threshold exists for every pulsing protocol. Namely, longer pulses, more pulses, or shorter inter-pulse pause, reduce the thresholds for both reversible and irreversible electroporation [56–61]. In addition, the thresholding method can only distinguish between treated and untreated tissue, even if it has been shown that there is a transition from electroporated to unaffected cells. This transition depends mostly on cell type, morphology, age and size [41, 45, 55, 106, 107].

In the field of food processing, statistical models have been widely studied to predict microbial inactivation [108]. In 2010, Golberg and Rubinsky [109] proposed tu use such models to describe cell survival probability with irreversible electroporation, and they successfully fitted the Peleg-Fermi model [110] on experimental data of prostate cancer [111]. Since

then, the Peleg-Fermi model has been widely studied to predict the treatment volume in irreversible electroporation because it characterizes cell survival as a function of the electric field magnitude and the number of pulses [60, 109, 112], compared to other models which only consider one parameter [59]. With this model, the probability of survival S is determined by:

$$S = \frac{1}{1 + \exp\left(\frac{|E| - E_c(n)}{A(n)}\right)} \tag{2.3}$$

where E is the electric field, $E_c(n)$ is the electric field at which half of the cells are dead, and $A(n)$ determines the slope of the transition. E_c and A are exponential decay functions that depend on the number of pulses n:

$$E_c(n) = E_{c0} \cdot \exp\left(-k_1 n\right) \tag{2.4}$$

$$A(n) = A_0 \cdot \exp\left(-k_2 n\right) \tag{2.5}$$

where E_{c0} and A_0 are the initial values, and k_1 and k_2 are the exponential decay coefficients. Notice that these four parameters are tissue specific. This model is not only used to determine the ablation volume as the tissue whose survival probability is below a threshold (between 1 % and 10 %) [113, 114], but it also describes the transition zone from living to dead cells (Fig. 2.7).

The main advantage of this model over the thresholding method is that it can be used for treatments were multiple number of pulses are applied. Due to electroporation generator limitations, it is not uncommon to change pulsing parameters to achieve similar outcomes [58, 115]. The Peleg-Fermi model can be used to compute the probability of survival of each pulsing sequence, and the overall survival probability S_t is obtained as the product of the survival probability of individual treatments S_i.

$$S_t = \prod_i S_i \tag{2.6}$$

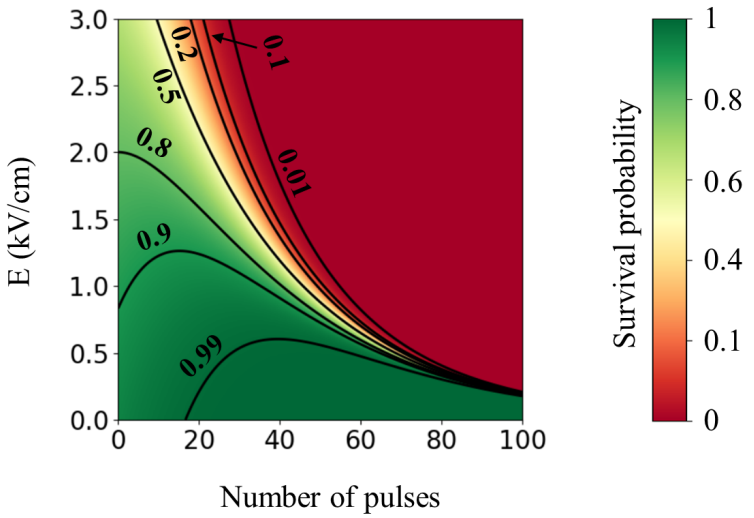

Figure 2.7: Illustration of the survival probability obtained with the Peleg-Fermi model as a function of the number of pulses and the electric field magnitude. Adapted from [60].

Additional modeling considerations: thermal distribution

During the application of the electric pulses, high electric currents are induced which can significantly rise the temperature due to Joule heating. This effect is most prominent in IRE because a high number of pulses (> 70) are applied. This can have two effects on electroporation treatment modeling. First, thermal damage can be assessed, as it is not uncommon to find thermally coagulated tissue around the electrodes [100]. Second, the dependence of the electrical conductivity on temperature can be modeled, as it can have a marked impact on the overall electric field distribution [103, 116]. It is estimated that electrical conductivity rises 2 % every degree Celsius in physiological tissues [101].

Penne's bioheat equation is the thermal model which best describes heat transfer in biological tissues, as it accounts for tissue metabolic heat

generation and blood perfusion (heat sink) [117]. The temperature T is obtained by:

$$\rho c \frac{\partial T}{\partial t} = \nabla \cdot (k \nabla T) - \rho_B \omega_B c_B (T - T_B) + Q_M + Q \tag{2.7}$$

where ρ, c, and k are the tissue density, heat capacity, and thermal conductivity, respectively. The metabolic heat generation is computed from the temperature difference between the tissue (T) and the blood (T_B), where ω_B is the tissue blood perfusion, ρ_B is the blood density, and c_B is the blood heat capacity. Q_m is the metabolic heat generation, and Q is any other heat source. For electroporation modeling, Q is the Joule heating which is derived from the electric currents solution:

$$Q = \nabla \phi \cdot \sigma \nabla \phi \tag{2.8}$$

Again, the electric field, the electrical conductivity and the temperature must be obtained iteratively, as they are dependent of one another. However, the temperature simulation is time dependent because heat is generated at every pulse and diffuses in time. Compared to the electric field simulation which is stationary and only takes a few minutes, solving the heat equation extends the simulation up to several hours [95].

2.2.3 Medical applications of electroporation

Tissue electroporation is the basis of several therapies. Such therapies induce electroporation by applying short monophasic or biphasic pulses, from a few nanoseconds to a few milliseconds, at a repetition frequency that typically ranges from 1 Hz to a few kilohertz. Although electroporation could be induced by a single long pulse, it is divided in shorter and spaced pulses as it has been observed that electroporation efficacy improves [58]. Although this thesis is mostly focused on IRE for tumor eradication, this section overviews all the electroporation-based therapies in clinical use, particularly focusing on the pulsing parameters.

In electrochemotherapy (ECT), an anti-cancer drug can penetrate into malignant cells thanks to the increased permeability obtained during RE. The chemotherapeutic drug (e.g., bleomycin, cisplatin) is inserted into the tissue locally or systemically prior to electroporation [118, 119]. A few minutes after, RE is induced and the molecule passively diffuses into the cell [120, 121], which increases cytotoxicity on the electroporated cells by a factor of 1.1 to several thousand times [122–124]. Typical ECT protocols consist of eight 100 μs pulses applied at 1 Hz. ECT was first used for the treatment of skin cancer. In recent years, preclinical and clinical trials have been investigating its feasibility and short term efficacy for deep seated tumors such as bone [125], liver [126, 127], pancreatic [128], prostate [129], brain [130], head and neck [131], and gastrointestinal [132,133]. It has been possible thanks to an advancement in electrode technology and, mainly, treatment planning [94,98,131,134–137].

Another clinical application of RE is electrogene therapy (EGT). EGT is a non-viral gene delivery method used for applications such as DNA vaccination and gene cancer therapy in multiple tissues [138–141]. A vector is inserted into the tissue (systemically or locally) which transfers into the cells when the membrane becomes permeable during RE. Typically, eight pulses of a few milliseconds are applied to enhance DNA uptake. These longer pulses are required because DNA uptake is driven by electrophoresis [142, 143]. For this same reason, protocols consisting of initial high-voltage pulse, which permeabilize the membrane, followed by low-voltage pulse, which drive DNA due to electrophoresis, have been proposed [142, 144].

Non-thermal irreversible electroporation (NTIRE) is an ablation procedure used for the ablation of solid tumors [20, 21, 145, 146]. In comparison to ECT, higher electric fields, and more pulses are applied to treat the target tumor without the need of an adjuvant drug. Between 70 and 100 pulses of 100 μs are usually applied at 1 Hz repetition frequency. NTIRE has been studied in the past years as an alternative to thermal

ablation of tumors. Its major advantage when compared to other physical ablation techniques is that it can be applied near vital structures such as vessels and bile ducts. Because the damage is non-thermal, only cells are targeted and the extracellular matrix, that is, the tissue scaffold, is left unaffected [21]. Even if cells that belong to such structures are ablated, the preservation of tissue allows re-population of healthy cells in a couple weeks [22, 23]. Nonetheless, due to the high electric fields, Joule heating is inevitable, which mostly concentrates around the electrodes [147]. Thus, it is contraindicated to insert the electrodes closer than 2 mm from a major vessel [7]. NTIRE is being researched for the ablation of liver [148], brain [113, 149], lung [150, 151], pancreas [98, 152, 153] and prostate [154] cancer.

A major issue of NTIRE is that, due to unsought electrical stimulation of excitable tissues, patients must be under general anesthesia and strong muscular relaxants to avoid muscle contractions. In addition, the pulses are synchronized with the refractory period of the heart beat to avoid fibrillation [7, 155]. High-frequency irreversible electroporation (H-FIRE) is a variation of NTIRE where bursts of short biphasic pulses are applied (from hundreds of nanoseconds to a few microseconds) [156–158]. Although higher electric fields are required to generate the same amount of IRE volume, the short pulses practically avoid or minimize muscle contractions [159–161]. H-FIRE pulsing protocols and other high frequency waveforms are being investigated for the treatment of tumors and for cardiac ablation [157, 162–166].

Cardiac ablation based on IRE for treatment of arrhythmias was proposed very early after the conception of NTIRE [167]. However, its development halted due to the risk of stimulating cardiac tissue and causing fibrillation [168]. It was not until H-FIRE was proposed that the research on electroporation for cardiac ablation resumed. Recently, it is being investigated as a promising alternative to radiofrequency ablation in a therapy known as pulsed field ablation (PFA) [166, 169, 170]. PFA can potentially solve many of the issues typically found with thermal ablation

such as treatment efficacy which relies on factors such as contact force and heat sink effect, or post-treatment complications such as esophageal fistula [171].

Another recent methodology for tissue ablation is based on the synergistic effect of electroporation and electrolysis, in a process called electrolytic electroporation (E2) [172]. In E2, cytotoxic electrochemical species are purposely generated, which enter the cell via electroporation. The application of 8 to 10 high voltage pulses of 100 µs induces electroporation, and the consequent low voltage pulses of long duration (a few minutes) induce electrolysis at the electrode interface [173, 174]. Alternatively, exponential decay pulses have also been proposed to generate the same effect. The high initial peak permeabilizes the cell membrane, whereas electrochemical reactions take place during the long tail of the decaying waveform [175, 176].

2.3 Treatment planning

Treatment planning is a process that consists in fine-tuning a therapy for a specific patient to predict treatment efficacy while minimizing side effects prior to the intervention.

In this section it is explored how patient-specific treatment planning is performed in solid tumor physical therapies. First, general traits are explained which are used for a wide range of procedures, from radiotherapy to thermal and non-thermal ablation. Second, the specific workflow and modeling methodologies used for electroporation-based therapies treatment planning are detailed.

2.3.1 Treatment planning in physical therapies for solid tumors

In the context of solid tumor therapies, treatment planning consists in designing the optimal treatment parameters to ensure that the whole tumor can be treated with minimal (or controlled) side effects [177, 178]. For ablative techniques and other focal therapies, treatment planning is a multi-step process. First, the treatment volume is localized from medical images. Second, it is computationally assessed if enough energy/dose can be safely deliviered. Usually, this step requires to create a model of the tissues from the medical images, which is used to simulate the treatment volume according to the delivered energy/dose. Finally, the dose can be adjusted and the treatment volume is simulated again to fine-tune the procedure.

A series of terms are defined in treatment planning for referring to the volume intended to be treated. The visible tumor in medical images (e.g., from computed tomography (CT), magnetic ressonance imaging (MRI), positron emission tomography (PET)) is referred to as the gross tumor volume (GTV). However, tumors present microscopic infiltration which is not observable in the images. A wider volume, known as the clinical target volume (CTV), is estimated to include both visible and microscopic tumor tissue. The CTV is obtained by adding a margin to the gross tumor volume (GTV) based on clinical criteria. Such margin should rather be overestimated to ensure all malignant cells fall within, otherwise the treatment would fail [27, 149, 179]. However, the CTV location in space and time is uncertain. Tumor movements occur between the day of acquisition of the images and the intervention day. The patient lay down position, breathing, and physiological movement of other internal organs can affect CTV location. It has been observed on continuous daily imaging that tumor displacement can be higher than 1 cm. Such uncertainties must be accounted for during treatment planning.

The planning target volume (PTV) accounts for the CTV plus the

convenient margins for tumor displacement [27, 179, 180]. Although this nomenclature is mostly used in radiotherapy treatment planning, these terms are also applicable in other focal therapies, such as electroporation. Figure 2.8 illustrates all these volumes.

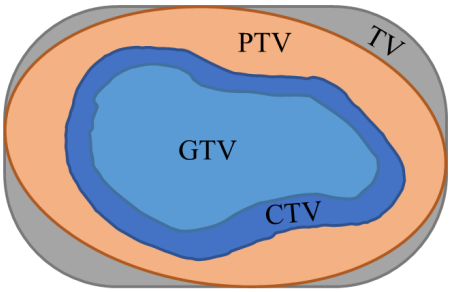

Figure 2.8: Schematic illustration of the different volumes considered for treatment planning: gross tumor volume (GTV), clinical target volume (CTV), planning target volume (PTV), and treatment volume (TV). Adapted from [27].

After obtaining the volume that must be targeted, the treatment volume (TV) is simulated to ensure that the whole PTV is successfully eradicated. The process consists in creating a tissue model, defining the treatment parameters, and simulating the treatment volume. Simple models only consider the properties of the healthy organ were the tumor is located. Nonetheless, more accurate results can be obtained by means of patient-specific modeling. By delineating the different tissues from medical images (tissue segmentation), an accurate patient anatomical model is built and specific properties are assigned to each tissue [12, 28, 94, 98, 113, 181]. Then, the simulation reveals the amount of dose applied to both the PTV and the surrounding healthy tissue. For example, in radiotherapy it is simulated how much ionizing radiation is uptaked, or in thermal ablation the temperature distribution is simulated to asses thermal damage.

The simulation of the TV serves two purposes. First, to asses the feasibility of the treatment [25, 182, 183]. For example, it is possible that

due to tumor location, the ionizing beams in radiotherapy cannot penetrate deep enough to reach the PTV. Or, in thermal ablation, vessels close to the PTV can cool the tissue by the heat sink effect leading to treatment failure. Second, treatment parameters can be adjusted and the treatment volume is simulated again to fine-tune the procedure [114, 184–187].

2.3.2 Treatment planning in electroporation-based therapies

In ECT and NTIRE, treatment efficacy strongly depends on the local electric field magnitude. For the treatment of internal tumors, needle-shaped electrodes are used to generate the field. However, the electric field distribution is very inhomogeneous and it mostly concentrates around the electrodes. In fact, the electric field distribution is highly dependent on the electrodes' position and length, the applied voltage, and the electrical conductivity of the treated tissues. Thus, electroporation treatments must be accurately planned to account for the uncertainties in electrode positioning and tissue properties.

Planning workflow

Treatment planning in electroporation-based therapies in essence consists in simulating the electric field distribution in an anatomical model. As explained in the previous section, accurate patient-specific 3D models can be obtained from the segmentation of the tissues from the medical images. Tissue properties are then assigned, namely, the electrical conductivity. The electrodes are virtually inserted into the model. The quantity and the position are determined as a function of the tumor shape and size. To ensure that the PTV is fully covered, the electrodes are usually placed neighboring to the tumor surface to ensure enough safety margin [28].

High electric fields are required for electroporation to take place, which are generated by applying high voltages. The electric field magnitudes required for ECT range from 100 to 500 V/cm which, for needle electrodes, typically translates into voltage to distance ratios from 1000 to 1500 V per cm [123, 188–191]. For NTIRE, higher electric field thresholds of 500 to 1200 V/cm are required. Such fields are achieved by applying a voltage to distance ratio between needles of 1500 to 2000 V per cm [25, 192–199]. Because commercial electroporation generators are limited to 3000 V, the maximum recommended electrode distance is 2-3 cm [200–202]. The voltage is then set accordingly. Finally, the electric field is simulated as described in section 2.2.2.

The predicted TV is the tissue whose electric field magnitude surpasses a threshold. If the PTV is enclosed by the predicted TV and no critical structures are damaged, the treatment is deemed feasible. The parameters can be further fine-tuned, namely, electrodes' position and voltage. Some algorithms have been proposed which optimize the parameters to ensure TV coverage while minimizing the number of electrodes and the treatment of healthy tissue [91, 114, 185, 203].

Existing software for electroporation treatment planning

Electroporation treatment planning can be divided in two steps: image segmentation and electric field modeling. This section explores the currently available software for these two tasks.

First, image segmentation consists in delineating tissue structures from medical images to extract patient anatomy. Thus, it is latter possible to assign specific properties to each tissue. Segmentation is a very complex process because tissues are highly heterogeneous in shape, size, location, and texture [204]. In addition, the visualization of tissues is also dependent on the imaging modality (e.g., CT, MRI), and generally there is low contrast between tissue types [205]. Whereas it is not too complex

for the trained eye to distinguish the overall shape of a tissue, there can be a high disagreement between clinicians when manually delineating tissue boundaries [206]. For the same reason, automatic algorithms can either roughly approximate textures and shape of multiple tissues, or they can be programmed to accurately segment a single tissue from a specific image modality.

On one hand, general purpose segmentation software generally provides manual and semi-automatic tools for the segmentation of multiple tissues. They are usually easy to use and require user input to some extent, but, because the user provides the algorithm with tissue information (texture, size, location...), they can be used to segment any tissue type from any imaging modality. Some general purpose segmentation platforms, free and paid, are ITK-Snap[1] [207], the Medical Imaging Interaction Toolkit (MITK)[2] [208], 3D Slicer[3] [209], Amira (Thermo Fisher Scientific, Waltham, MA, USA), BioImageXD [210], and Icy [211].

On the other hand, there are accurate algorithms for specific tissue segmentation. Mainly, these are based on recent implementations of deep learning techniques which have been used for a wide variety of tissues such as brain [212–214], liver, [215], lung [216], prostate [217], pancreas [218–220], knee cartilage [221], coronary artery [222], and multiple organs [223, 224]. Although these are much more accurate than general purpose tools, they are limited to the specific tissue and imaging modality they were trained on. In addition, they have been developed for research purposes and are usually difficult to use by the average user.

The second task of electroporation planning consists in simulating the electric field distribution. Typically, available software uses numerical methods to solve the partial differential equations to obtain the electric field distribution (described in section 2.2.2). COMSOL Multiphysics

[1] ITK-Snap: www.itksnap.org
[2] MITK: https://www.mitk.org
[3] 3D Slcier: https://www.slicer.org

(COMSOL AB, Stockholm, Sweden) and other general purpose finite elements method (FEM) and finite differences method (FDM) software, are widely used for modeling the electric field in electroporation-based therapies [23, 60, 225]. However, the use of this sort of tools requires significant expertise in physics and in numerical modeling, and, thus, they are not adequate for clinical users.

There are a few precedents of specific software tools for estimating the electric field distribution in electroporation based therapies which have been developed aiming at clinical users. For instance, the electroporation generator NanoKnife (AngioDynamics, Queensbury, NY, USA), used for NTIRE procedures, includes a simulation tool which approximates the electric field distribution after the user specifies the electrodes arrangement. However, it is quite simple as it assumes a homogeneous tissue, and it only provides an estimation of the electric field in planes perpendicular and/or coplanar to the electrodes. In fact, this tool is not for treatment planning, but rather to confirm *in situ* that the procedure has been well planned. Another example is ApiVizTEP [226] which analytically computes in real time the electric field distribution in a 2D plane, but it is nor a tool for accurately modeling the TV. Instead, it aims at illustrating the electric field distribution as a function of the number of electrodes.

A much more accurate simulation is provided by OpenEP[4] [227], which is a specific software for electroporation-based treatments. With it, not only the electric field distribution is simulated, but it also estimates the electroporation volume and the heat generation (to asses thermal damage), among other electroporation-related variables. Different electrode number and types can be simulated, as well as their arrangement. However, it assumes a homogeneous 3D tissue, which for patient-specific treatment planning is not ideal because it cannot account for complex tissue geometries.

[4] OpenEP: github.com/LSC-UBA/OpenEP

At last, VISIFIELD[5] is a patient-specific web platform for treatment planning of ECT and NTIRE therapies [24, 228]. From medical images, tissue segmentation can be performed manually, or automatically in specific tissues such as liver. The user can virtually insert the electrodes and assign tissue properties, and the electric field distribution is simulated in the cloud. A treatment plan summary can be downloaded after a satisfactory electric field simulation. This platform has been used to successfully plan liver [25] and canine brain tumor therapies [113]. Nonetheless, since its publication, recent studies have shown the importance of modeling considerations which were not available at the time. For example, the electrodes cannot be positioned in a non-parallel fashion, nor inserted at different depths. This can be an issue for planning the incision of percutaneous deep seated tumors where critical structures force electrodes insertion at different angles [225]. Failing to model the electric field in the same conditions that will be met during the intervention will probably lead to treatment failure. Moreover, it does not model the dependence of the electrical conductivity on the temperature. As it has been reported in some numerical studies, the temperature increase can have a marked impact in the overall treatment volume, mostly in IRE procedures due to the high number of applied pulses [103, 116].

[5] VISIFIELD: www.visifield.com

Chapter 3

AN ELECTRIC FIELD VISUALIZATION WEB PLATFORM FOR ELECTROPORATION MODELING

Adapted from:
Perera-Bel E, Yagüe C, Mercadal B, Ceresa M, Beitel-White N, Davalos RV, González Ballester MA, Ivorra A. EView: An electric field visualization web platform for electroporation-based therapies. *Computer Methods and Programs in Biomedicine*. 2020; 197:105682.
DOI: 10.1016/j.cmpb.2020.105682
Available at: *https://doi.org/10.1016/j.cmpb.2020.105682*

3.1 Introduction

In recent years, computational treatment planning has greatly improved prognosis in all branches of medicine. It is already a common practice in radiotherapy [183, 229, 230], and it is starting to be implemented in other therapies such as radiofrequency ablation [12, 231] and electroporation based treatments [28, 185].

Planning for electroporation procedures relies on defining the electrode setup (number of electrodes and voltage pairs) and simulating the electric field distribution in the corresponding tissue [101, 232]. It is generally accepted that, for a given tissue and a given pulsing protocol, electroporation is effective where the electric field magnitude caused by the pulses is above a certain threshold. Tissue electrical conductivity cannot be considered constant in electroporation treatments; because of the permeability increase to ions during electroporation, conductivity rises, an effect which is approximated by modeling the conductivity as a function of the electric field magnitude [87, 96, 99]. Additionally, the electric field distribution is very susceptible to electrode setup. Thus, if the conductivity is incorrectly modeled, or the electrodes fail to be positioned according to the planning, the tumor will not be fully treated during the intervention. Being able to model and to account for multiple, plausible, scenarios (considering these uncertainties) will help in predicting the outcome even when the intervention setup differs from the planned one.

COMSOL Multiphysics (COMSOL AB, Stockholm, Sweden) and other general purpose simulation tools based on the FEM or the FDM are widely used for electroporation modeling in scientific studies [23, 60, 95, 225]. However, the use of this sort of tool requires significant expertise in physics and in numerical modeling. Thus, they are not adequate for clinical users.

There are a few precedents of specific software tools for estimating the

electric field distribution in electroporation based therapies which have been developed aiming at clinical users.

For instance, the NanoKnife (AngioDynamics, Queensbury, NY, USA) system for IRE includes a simulation tool to approximate the electric field distribution once the electrodes are implanted. However, this tool simply assumes that the electrodes are placed in parallel and displays an approximation of the volume that will be treated in planes perpendicular and/or coplanar to the electrodes. Another example is the educational tool ApiVizTEP [226], which is used to visualize the electric field distribution using up to twelve electrodes on a 2D domain representing an anatomical tissue. A more advanced example is the platform VISIFIELD developed by a team of the University of Ljubljana, Slovenia. VISIFIELD is an electroporation planning web platform that allows a patient specific modeling based on patient medical images [97, 228]. It provides tools to manually and automatically perform image segmentation, to manually insert the electrodes, to compute the electric field distribution and visualize it. It has already been used in studies focusing on liver tumors, and on canine brain tumors [25, 113]. The use of VISIFIELD implies the execution of multiple semi automatic processes with lots of steps. Its authors report that only the segmentation process takes between 6 minutes and an hour.

VISIFIELD is a powerful tool that can be used for realistic patient specific treatment planning. COMSOL and other FEM/FDM solvers can also be used for that same purpose if coupled with external segmentation tools [98, 225]. However, to account for different scenarios (e.g., electrodes positioning and length of exposure, applied voltage and electrical conductivity of the treated tissues) that can differ between planning and intervention, these tools lack adaptability as they are too complex and computationally expensive. That is, these tools are too cumbersome to use when a rapid estimation is desired. On the other hand, the built-in modeling of NanoKnife and the educational tool ApiVizTEP are much more adaptable as they provide a near real time simulation of the electric

field for any electrode configuration, but they perform too simplistic modeling, considering only a 2D tissue with a constant electrical conductivity. We have created the tool presented here, EView, trying to fill the gap between the two approaches for electroporation modeling. That is, with EView we try to provide a new balance between ease of use and accuracy. On one hand, compared to the more simple tools, EView adds 3D modeling in homogeneous tissues with non-linear electrical conductivity, which provides a much realistic simulation. On the other hand, it does not evaluate the interaction between different conducting tissues, such as tumor and healthy organ, that the patient-specific tools provide, but EView improves user-friendliness and drastically reduces computation time. Thus, the goal is to provide a good initial estimate of the electric field distribution and to illustrate the dependencies on electrodes'positioning, orientation and length, on the applied voltage, and on the electrical conductivity of the treated tissues. EView aims to be the first step for students, researchers and clinicians that want to enter the electroporation field or that want to understand better how the electric field behaves in electroporation therapies.

We have validated our implementation comparing, for different scenarios, the computed electric field distribution by EView with that computed with COMSOL Multiphysics. In addition, we have performed a load test to ensure a reliable operation and we report the simulation times as a function of the number of electrodes used.

EView is available at *https://eview.upf.edu*.

3.2 Materials and methods

3.2.1 Platform design

EView has been developed with the aim of facilitating the understanding of how the electric field distribution depends on the geometry of the electrode setup and the applied voltage. The user simply needs to: 1) specify tissue conductivity (which for the cases of hepatic and pancreatic tissue is pre-specified), 2) insert the electrodes, and 3) specify the voltage that will be applied across electrode pairs. The electric field is simulated according to the specified configuration and the electric field is displayed. This platform is free to use, but it is required to register beforehand in order to be able to execute a simulation. Non-registered users can visualize an example and interact with the electric field distribution, as well as experience with electrode configurations. A tutorial is also provided to aid new users getting started, and clear explanations are available for all the steps.

User workflow

Fig. 3.1 displays the workflow to obtain the simulated electric field distribution. Upon web page loading, a void scenario is presented, representing a homogeneous volume. The background is simply black. The user can select a tissue, place the electrodes in this scenario and define the voltages that will be applied between the electrode pairs. Additionally, previous simulation configurations can be loaded and modified. This way, the electric field distribution can be compared between slightly modified setups. By simply defining these three parameters (electrodes's positioning, voltage pairs and tissue) the simulation can be computed. The modeled electric field is displayed on the current scenario, and the electric field is projected around the

electrodes. Alternatively, a medical image can be loaded. Thus, the electrodes can be placed according to anatomical landmarks and a tissue can be selected according to the region of interest of the image. The simulated electric field is visualized as an overlay on the medical image.

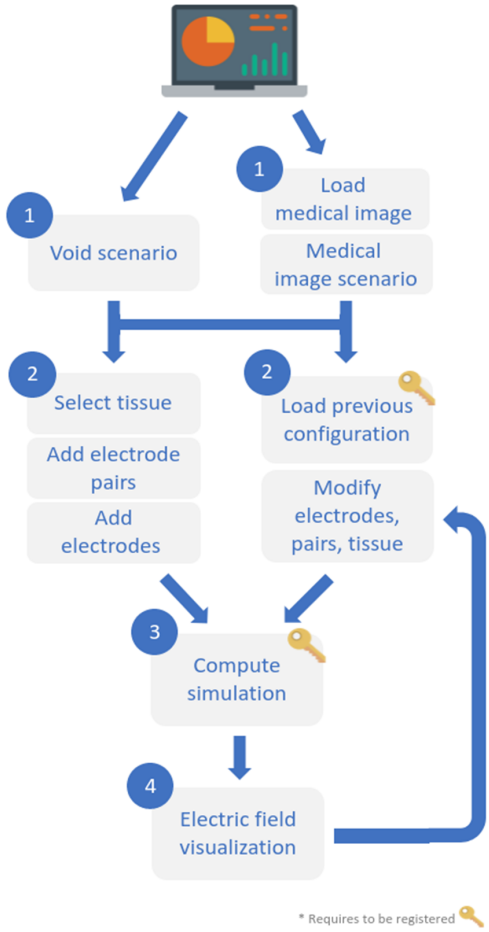

Figure 3.1: Workflow diagram of EView for the simulation and visualization of the electric field. Some of the icons used in this fugure are made by Smashicons from *www.flaticon.com*.

User interface

The main content of the web page is a viewer. A thin sidebar can be found at the right of the screen, containing the necessary menus and tools for setting up the electrode configuration, running the simulation and visualizing the electric field. The viewer is composed of four different views: a 3D window, and axial, sagittal and coronal views (Fig. 3.2).

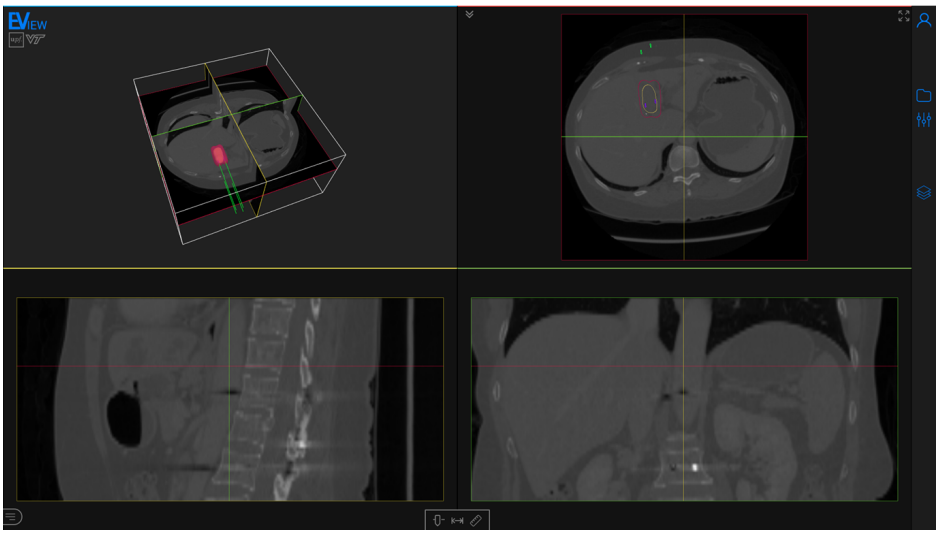

Figure 3.2: Screenshot of the webpage with a computed electric field distribution. The page is composed mainly of the viewer, and a toolbar (right) containing all the tools for preparing the model and for the visualization. The displayed medical image is an abdominal CT with a hepatocellular carcinoma (yellow). Four electrodes (green) are inserted and the isosurface corresponding to an electric field of 600 V/cm is visualized (red). Medical image from 3D-IRCADb-01 database from IRCAD, France.

The accepted image formats are Neuroimaging Informatics Technology Initiative (NIfTI), Nearly Raw Raster Data (Nrrd), and Digital Imaging and Communications in Medicine (DICOM). Brightness and contrast can

be adjusted in the bottom toolbar of the viewer. The images are never uploaded to the server, they are only displayed on the client web browser, and are erased from the browser upon reloading/closing the session.

The configuration of the setup (tissue selection, electrode insertion and definition of voltage pairs) is performed through the Electroporation menu (Fig. 3.3.a). A tissue can be selected from the pre-specified ones (liver or pancreas) or it can be user-defined. Up to six monopolar electrodes can be inserted, with independent exposure lengths between 5 and 40 mm. The separation of the electrodes can be measured and all electrodes can be automatically oriented in parallel to a specific one. The voltage has to be indicated for each electrode pair within the range from 50 V to 3000 V at 50 V steps. There can be a maximum of $N(N-1)/2$ pairs for monopolar electrodes, where N is the number of inserted electrodes. Alternatively, a single bipolar electrode can be defined. The length of both exposed parts and the insulator in between can be set independently between 5 and 20 mm.

The electric field magnitude distribution is simulated considering the specified setup. The result is represented as a field magnitude isosurface (isoline in the 2D views) whose value (i.e., threshold) can be selected from 50 V/cm to 2000 V/cm at 50 V/cm steps (Fig. 3.3.b). If multiple electrode pairs are specified, the resulting isosurface corresponds to the geometrical union of the isosurfaces computed for each electrode pair.

Framework

The platform has been designed as a client-server application. On one hand, the client contains the tools needed for creating the electrode configuration and to render the electric field distribution. On the other hand, the simulation is executed on the server. By using this approach, the most computationally expensive task is left to the server, freeing the client from a computational burden.

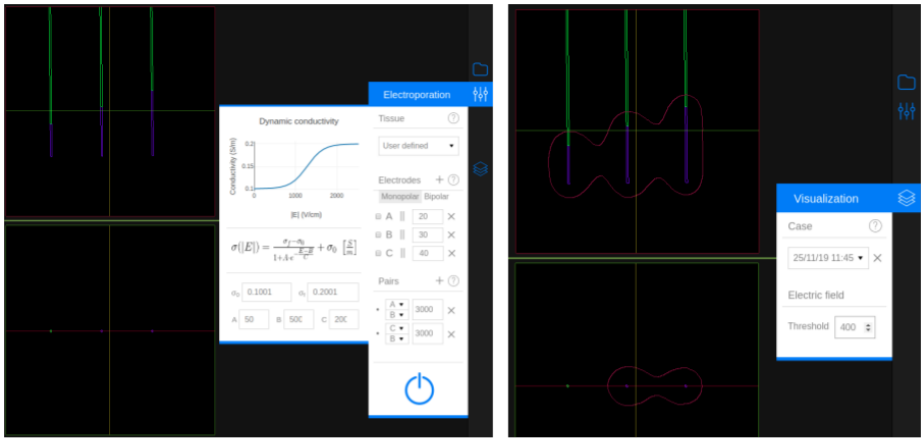

(a) (b)

Figure 3.3: A configuration with three electrodes and two pairs. (a) Inserted electrodes and the Electroporation menu. The menu contains three sections: Tissue, Electrodes, and Pairs. The dynamic (non-linear) conductivity plot is displayed when the selected tissue is User defined. The Electrodes section shows a list of all the defined electrodes. Each element has, from left to right, the distance combobox (to measure separation between electrodes), the electrode label, the parallel button, the exposed length, and the delete button. The Pairs section shows a list of the specified pairs, showing the labels of the two selected electrodes and their voltage. At the bottom of the menu there is a button to execute the simulation. (b) Visualization of the electric field distribution at 400 V/cm and the Visualization menu. In this menu a simulation (case) can be selected and the electric field threshold can be specified.

Fig. 3.4 depicts the framework contained in the server. It contains two application programming interfaces (APIs) for communication between the client and the server, a data base (DB), a network file system (NFS), and a computation engine. The client can only communicate via HTTPS to the APIs: API AUTH and API SIMULATIONS. The former is used for user registration (sign up) and login. The latter receives the electrode setup parameters from the client, interacts with the server to store the parameters in the DB and executes the simulation in the

computation engine. The result of the simulation is stored in the NFS. API SIMULATIONS also notifies the client when a simulation is finished, and the simulation is downloaded from the NFS into the client.

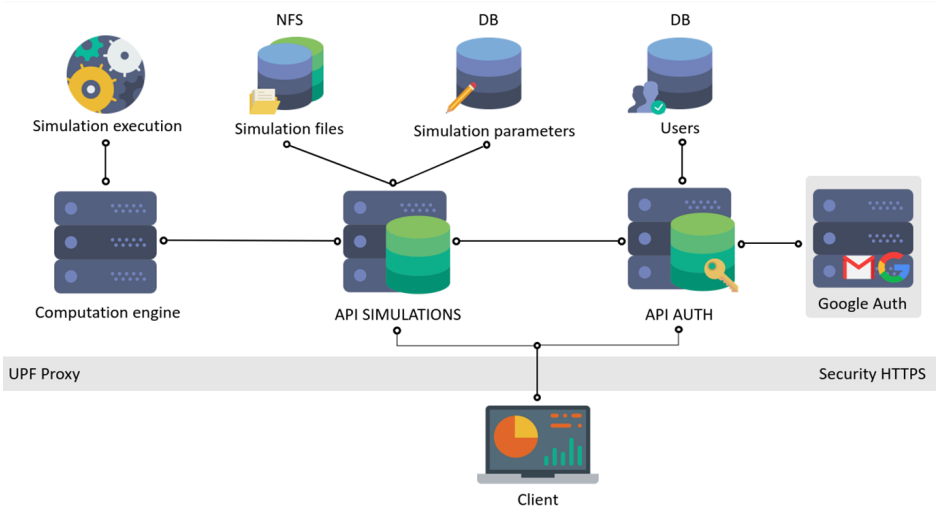

Figure 3.4: Framework diagram of EView. The client communicates to the server via HTTPS to two APIs, AUTH for authentication of the user (sign up and log in), and SIMULATIONS to execute a simulation on the server. A DB stores electrode configuration and the NFS stores the simulation output. The simulation is executed in a computation engine. Some of the icons used in this figure are made by Smashicons from *www.flaticon.com*.

Only open access software has been used for the development of EView. Fig. 3.5 shows all the technologies used for the client and for the server. The web (i.e., client) has been developed with html, css and Javascript. Additionally, React[1] was used as the main graphical interface framework. Three.js[2] is a 3D library and ami.js (AMI, Medical Imaging Javascript Toolkit)[3] is a toolkit for medical image web rendering based on Three.js. Both were used for the visualization of images and the rendering of the

[1] React: https://reactjs.org
[2] Three.js: https: //threejs.org
[3] ami.js; https://github.com/FNNDSC/ami

electric field. The electric field distribution is computed in the server using Elmer[4]. The mesh is created using The Visualization Toolkit (VTK)[5] [233] and The Computational Geometry Algorithms Library (CGAL)[6] [234, 235].

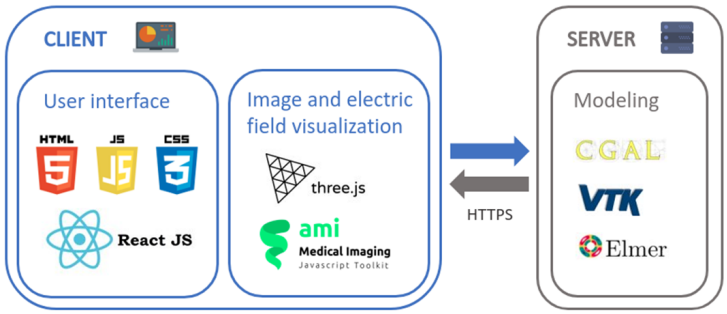

Figure 3.5: Technological stack diagram used in the development of the client (electrode and tissue setup) and the server (modeling). Some of the icons used in this figure are made by Smashicons from *www.flaticon.com*.

3.2.2 Electric field modeling

Tissue model

A 3D homogeneous FEM mesh is built using VTK and CGAL according to the setup specified by the user. A linear tetrahedra mesh is built which contains up to six monopolar electrodes, or a single bipolar electrode. We performed a mesh convergence study by initially simulating the electric field on a coarse mesh and then doubling the mesh density iteratively until the change in the solution was less than 1%. Only the active parts of the

[4] Elmer: https://www.csc.fi/ web/elmer
[5] VTK: https://www.vtk.org
[6] CGAL: https://www.cgal.org

electrodes are considered. Monopolar electrode length can be set from 5 mm to 40 mm. With a bipolar electrode, the length of both exposed segments and the insulator in between can be set independently between 5 mm and 20 mm. Both electrode types have a diameter of 1 mm.

The electrodes are meshed in a spherical domain (Fig. 3.6). The size of the outer sphere was determined by computing the same simulation on a domain 10 times larger and verified that the Dice score on the extracted isosurfaces was higher than 95%. The size is set according to the bounding box containing the electrodes:

$$r_{BS} = \frac{d_{BB}}{2} + 3d_{BB} \tag{3.1}$$

$$d_{BB} = \max(d_x, d_y, d_z) \tag{3.2}$$

where r_{BS} is the radius of the spherical domain, and d_{BB} is the maximum size of the bounding cube containing all the electrodes, with d_x, d_y, and d_z as its three orthogonal sizes. However, the product $3d_{BB}$ is limited to a minimum of 30 mm and a maximum of 120 mm, which allows to have enough space between electrodes and the boundary when using short electrodes, and limits the creation of meshes that are unnecessarily big when longer electrodes are used.

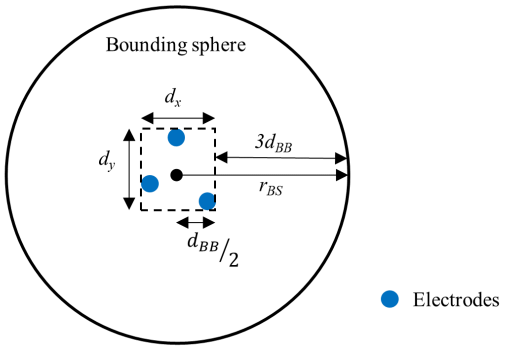

Figure 3.6: Schematic 2D representation of the size of the bounding sphere.

A constrained Delaunay triangulation is computed to generate the tetrahedral mesh [236]. An adaptive criteria is followed to define tetrahedron size, using a Weibull distribution to place finer elements around the electrodes and coarser ones near the outer boundary:

$$r = r_{max} - (r_{max} - r_{min}) \exp\left(-\left(\frac{d}{\lambda}\right)^{\kappa}\right) \tag{3.3}$$

where r is the upper bound of the tetrahedron circumradius of the Delaunay triangulation, r_{max} and r_{min} are the maximum and minimum radii, respectively, λ is the scale parameter, κ is the shape parameter, and d is the distance between a point in the mesh and the closest electrode. The minimum and maximum circumradii are set to 1 mm and 15 mm, respectively, to allow fine elements in the regions of interest and coarser ones near the outer boundary. The shape and scale parameters, $\lambda = 50\,\mathrm{mm}$ and $\kappa = 2$, are established to keep a high density of tetrahedra near the electrodes and to provide a good transition towards the end of the boundary. Using this approach, the mesh contains around $(80-220)\times10^3$ tetrahedra depending on the number of electrodes, their position, and the length of exposure.

Simulation of the electric field distribution

The electric field is simulated using Elmer by solving the governing equations for electric currents:

$$\nabla \cdot \sigma \nabla \phi = 0 \tag{3.4}$$

$$\vec{E} = -\nabla \phi \tag{3.5}$$

where, ϕ is the electric potential, σ is the electrical conductivity and $\vec{E}$ is the electric field. Electrical conductivity is known to increase during electroporation; non-linear models have been widely studied and they provide quite a good estimation of the electric field distribution

[25, 60, 84, 87, 95–99, 113, 225, 228]. We adopt the symmetric sigmoid function model used in [87]:

$$\sigma(E) = \sigma_0 + \frac{\sigma_{max} - \sigma_0}{1 + A \exp\left(-\frac{|E|-B}{C}\right)} \tag{3.6}$$

where $|E|$ is the magnitude of the electric field, σ_0 is the static conductivity (i.e., conductivity for field 0 V/cm), σ_{max} is the maximum conductivity that can be reached during the electroporation pulse, and A, B and C are the parameters that define the shape of the sigmoid. This sigmoid was fitted to ex vivo data for liver and pancreatic porcine tissue reported in [88] (Table 3.1).

Tissue	σ_0 (S/m)	σ_{max} (S/m)	A	B (V/cm)	C (V/cm)
Liver	0.188	0.289	80.03	613.1	252.2
Pancreas	0.214	0.307	0.007	978.1	150.3

Table 3.1: Electrical conductivity of the tissues included in the platform.

Due to the strong non-linear behavior of electrical conductivity, the solution to eq. (3.4) is obtained iteratively with an initial electrical conductivity $\sigma^0 = \sigma_0$. However, this is not sufficient for the algorithm to converge and would lead to oscillations. Thus, a relaxation mechanism is included to the computation of the new electric potential:

$$\phi_k^* = \gamma \phi_k + (1 - \gamma)\, \phi_{k-1} \tag{3.7}$$

where γ is the relaxation factor and ϕ_k is the new approximation of the electric potential, given the current ϕ_{k-1} and the previous iteration ϕ_{k-1} potentials. Convergence is reached when the L^2-norm of change of both the electric potential and the electric field are smaller than 10^{-5}. The relaxation factor for liver and pancreas has been set to $\gamma = 0.875$ and $\gamma = 0.972$, respectively, to boost convergence while avoiding oscillations.

The electrical conductivity can also be manually defined by the user. For constant conductivity (i.e., $\sigma_0 = \sigma_{max}$), the relaxation mechanism is not

required. For non constant conductivities (i.e., $\sigma_0 < \sigma_{max}$), C is the parameter which has the greatest influence on the non-linear behavior of the conductivity because it characterizes the sharpness of the transition from σ_0 to σ_{max} (see eq. (3.6)). Thus, a very non-linear case ($C = 50\,\mathrm{V/cm}$) has been used to determine the relaxation factor for user defined conductivities.

$$\begin{aligned} 1 < \sigma_{max}/\sigma_0 \leq 2 &\rightarrow \gamma = 0.75 \\ 2 < \sigma_{max}/\sigma_0 \leq 3 &\rightarrow \gamma = 0.65 \\ 3 < \sigma_{max}/\sigma_0 \leq 4 &\rightarrow \gamma = 0.55 \end{aligned} \tag{3.8}$$

With these relaxation values we ensure convergence for all scenarios, although cases with a weaker non-linear nature are slightly penalized with extra iterations and, thus, computation time. Notice that a rise in conductivity above 3 and sharper transitions ($C < 50\,\mathrm{V/cm}$) are not expected in biological tissues. Therefore, these parameters have been limited at 4 and at 50 V/cm, respectively.

A simulation is computed for every electrode pair with the specified voltage. The outer boundary of the mesh is set as insulating. In multiple pair scenarios (more than two electrodes), the inactivated electrodes are modeled with a floating potential boundary condition, which is that the boundary has an unknown constant potential but the net current through it is zero, defined by:

$$\int_{\partial\Omega_F} -\vec{n} \cdot J \,\mathrm{d}S = 0 \tag{3.9}$$

where $\vec{n}$ is the normal vector, J is the current, and it is integrated over the boundary surface $\mathrm{d}S$. This boundary condition is solved in Elmer using the virtual homogeneous boundary condition method [164]. It is implemented on the discrete level (i.e., directly on the matrix), by solving the problem $Ax = b$, with $x = \phi_F$ (unknown floating potential) at the boundary Ω_F nodes. First, all the nodes i in Ω_F are identified. Second, a representative node j from Ω_F is chosen. Third, all the rows i are summed to row j. This step can be motivated if we think that the basis

function is composite of all nodes (with the same unknown potential). Fourth, all the rows i are replaced with identity (i.e., a $ii = 1$) and a ij is set to -1, thus $x_i = x_j = \phi_F$.

Once all the simulations have been computed, electric field isosurfaces are extracted from 50 to 2000 V/cm in 50 V/cm steps. If more than one electrode pair is simulated, the isosurfaces are obtained by computing the geometrical union between simulations.

3.2.3 Validation

To validate the accuracy of our implementation for multiple setups, we compared the electric field obtained with EView to the one computed with COMSOL Multiphysics, a generic FEM software platform frequently used in treatment planning of electroporation-based treatments [23, 60, 95]. Eleven different configurations using two electrodes with variable lengths, separation, and angles were analyzed using constant ($\sigma = 0.1$ S/m) and non-linear ($\sigma_0 = 0.1$ S/m, $\sigma_f = 0.3$ S/m, $A = 100$, $B = 100$ V/cm, $C = 50$ V/cm) electrical conductivities, computing a total of 22 simulations. A voltage of 3 kV was applied in all the cases. We extracted electric field isosurfaces at 700 V/cm and compared both implementations by computing the Dice coefficient, Jaccard index and volume similarity (VS).

$$\text{Dice} = \frac{2|X \cap Y|}{|X| + |Y|} \tag{3.10}$$

$$\text{Jaccard} = \frac{|X \cap Y|}{|X \cup Y|} \tag{3.11}$$

$$\text{VS} = \frac{|X - Y|}{|X| + |Y|} \tag{3.12}$$

where X and Y are the volume contained inside each surface.

In order to evaluate workflow performance, a stress test was conducted, requesting the server to run a new simulation every minute for over 18 hours, which were also used to analyze and report simulation time. Each simulation was configured randomly with constraints to mimic plausible scenarios. The following criteria was used:

- Between 2 and 6 electrodes, with lengths from 5 mm to 40 mm and placed in a sphere with a radius of 30 mm.
- Between $N - 1$ and $N(N - 1)/2$ pairs (N being the number of electrodes), with voltages from 1000 V to 3000 V.
- Electrical conductivity with σ_0 from 0.01 S/m to 0.6 S/m and σ_{max} between σ_0 and $3\sigma_0$. A was set between 10 and 1000, and B and C from 10 V/cm to 1000 V/cm.

3.3 Results and discussion

3.3.1 Modeling accuracy

We compared the electric field obtained with EView to the one computed with COMSOL. With eleven different configurations with constant and non-linear electrical conductivities, we obtained a Dice coefficient, Jaccard index and VS of $98.3 \pm 0.4\,\%$, $96.7 \pm 0.7\,\%$, and $99.0 \pm 0.6\,\%$, respectively. These results show that the two implementations yield the same results. The small differences arise from different meshing methods and slightly different solver convergence criteria. In addition, the graphic representation of the results (Fig. 3.7) clearly illustrates the importance of including the non-linear behavior of electrical conductivity. In all cases it can be observed that the electric field between the electrodes is higher with the non-linear model. Additionally, Fig. 3.8 shows a smooth

convergence of the non-linear problem for all 11 cases, and that the proposed stopping criterion for both the electric potential and the electric field is necessary because they do not converge at the same iteration (green and red lines). The proposed iterative method (eq. (3.7)), prevents the appearance of oscillations and proves to be consistent even for the most non-linear cases ($C = 50\,\mathrm{V/cm}$).

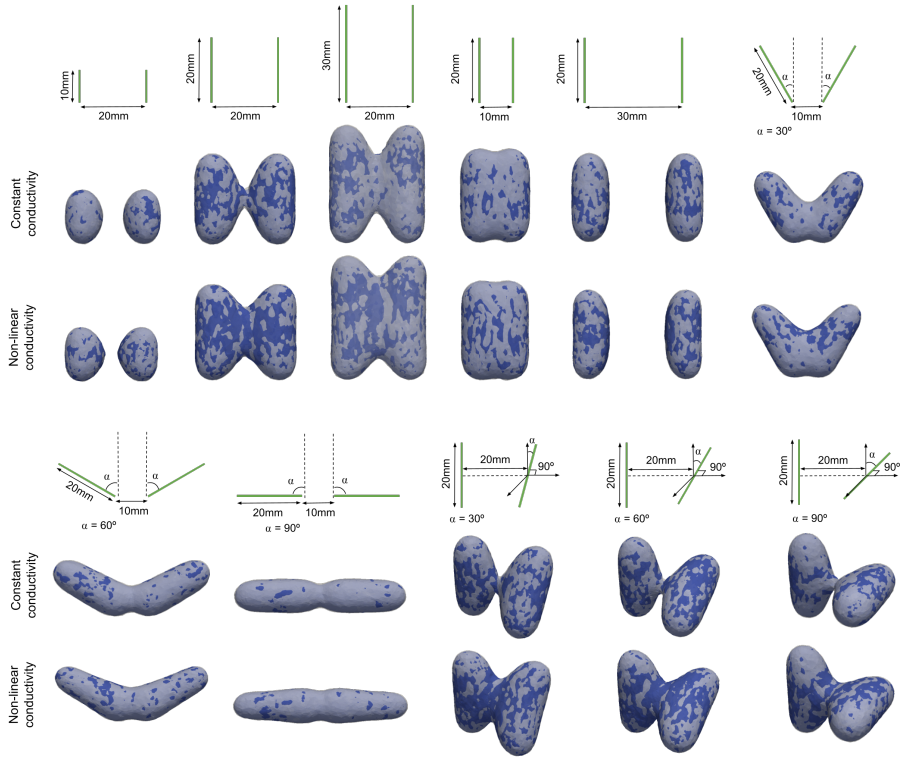

Figure 3.7: Configurations of the electrodes used for comparing the results provided by EView and those provided by COMSOL. Each configuration is represented schematically, and the simulation is shown under each scheme. An isosurface at 700 V/cm is represented (EView in white and COMSOL in blue).

The resulting isosurface for multiple electrode pairs corresponds to the union of the isosurfaces computed for each pair. The union is an

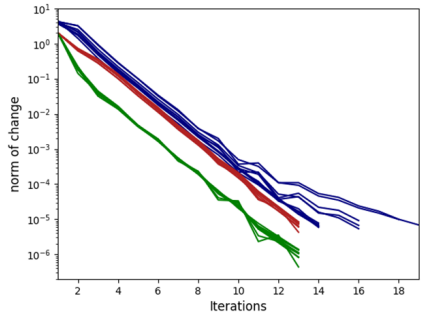

Figure 3.8: Convergence (L^2-norm) of the non-linear system for all 11 configurations for EView (green is the electric potential and red is the electric field) and COMSOL (blue).

approximation of the treated volume, as each electrode will experience a different pulse sequence depending on the generator, and the electric field distribution can be also affected due to Joule heating.

3.3.2 Performance analysis

A stress test was conducted to evaluate workflow performance. A total of 1092 simulations were executed over 18 h, with only 6 simulations (0.5 %) failing (due to server overload). However, load prediction for normal circumstances is expected to be much lower than during the performed test. Thus, we do not expect server overload during normal use. The remaining 1086 simulations were used to analyze simulation time. From Fig. 3.9.a it is observed that the median time and the variability increase with the number of electrodes. This is an obvious consequence of the fact that more electrodes allow more pairs. It is explained considering that for N electrodes, the minimum number of pairs is $N - 1$ and the maximum is $N(N - 1)/2$ (e.g., three electrodes can have between 2 and 3 pairs, whereas six electrodes can have between

5 and 15 pairs). From Fig. 3.9.b, a large dispersion in computation times for any electrode pair number is observed. We mentioned earlier that the mesh is built adaptively, with the finest elements around the electrodes. Therefore, more electrodes and longer exposures require more elements in the mesh, leading to a more expensive computation.

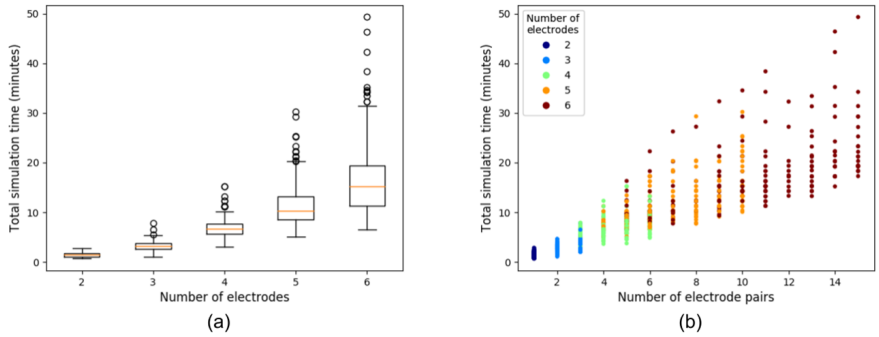

Figure 3.9: (a) is a boxplot of the total simulation time as a function of the number of electrodes and (b) shows the total execution time as a function of quantity of electrode pairs, and colored according to the number of electrodes.

The overall simulation process (i.e., since the user sends the simulation to the server until the result files are stored in the NFS) can be divided in three parts: meshing, simulating and pre/postprocessing tasks. One one hand, pre/post-processing takes an average of 0.59 minutes with 2 electrodes and rises linearly up to 1.13 minutes with 6 electrodes, and meshing rises similarly from 0.37 minutes on 2 electrodes to 0.93 minutes on 6 electrodes. On the other hand, simulation follows an exponential fashion, with an average of 0.47 minutes on 2 electrodes up to 14.78 minutes on 6 electrodes. From Fig. 3.10 it is observed that on low number of electrodes (2 and 3), pre/post processing and meshing occupy around half of the total time, but using more electrodes (hence requiring more pairs) increases the overall weight of the simulation, up to an 85 % with 6 electrodes.

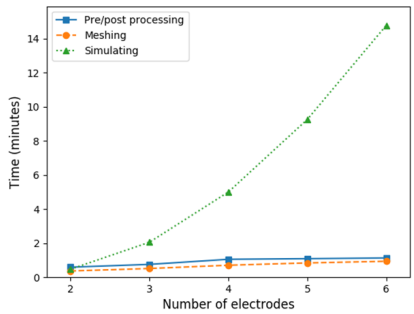

Figure 3.10: Average computation time of the different steps of the simulation pipeline, pre/post processing, meshing and simulating as a function of the number of electrodes.

Although the computation times to obtain the electric field for two electrodes (around 2 minutes) are acceptable, it is clear that with four or more electrodes the waiting time increases (more than 5 minutes). Current hardware and FEM software are capable of multithreaded and even GPU computation. At present, EView does not take advantage of parallel processing yet and the whole workflow is executed sequentially on a single thread.

3.3.3 Limitations and lines of improvement

To prioritize a user friendly system that rapidly computes an estimation of the electric field, the mesh in EView is generated with linear tetrahedra. Although to model non-linear problems, such as conductivity changes due to electroporation, quadratic elements should be preferred, we verified that the error is minimal. When comparing the results of both methods, we obtained an average Dice coefficient of $97.4 \pm 1.5\,\%$ for all the extracted isosurfaces, with a minimum value of $94.8\,\%$. This error is negligible if we consider that EView scope is to provide an initial

estimate. In contrast, the computation time was heavily penalized when using quadratic elements; the simplest cases took more than five minutes and the longest more than two hours.

EView computes the electric field given some arbitrarily positioned electrodes and non-linear tissue properties on a homogeneous 3D domain. Moreover, the electrodes can be positioned according to anatomical landmarks of a loaded medical image. This image is only used for visualization purposes and is not considered during the simulation. Although this is an improvement over the educational tool ApiVizTEP [226], it does not evaluate the effect of the presence of tissues with different conductivities (e.g., tumor, healthy organ, vessels) that is known to be the cause of failure in some IRE treatments [104]. However, the goal of EView is to provide a good initial estimate of the electric field distribution, and multiple tissue scenarios, which require of accurate image segmentation, are out of the current scope. We plan, however, to provide a dual domain model (e.g., organ and tumor) in future releases.

Lately, IRE is being investigated as a promising cardiac ablation procedure [166, 170, 237]. However, with EView it is not possible to model cardiac IRE scenarios because a reliable simulation should at least consider myocardium and blood due to the high difference in conductivities. Nonetheless, with the inclusion of dual tissue modeling on future releases, we will analyze the feasibility of adapting EView to cardiac ablation.

3.4 Conclusions

We have developed a web-based platform with the aim of illustrating the dependence of the electric field distribution on the geometry of the electrode configuration and the applied voltage in a given tissue. Currently available platforms for simulating the electric field in

electroporation-based therapies either require much more sophisticated models, both computationally and in terms of the required user expertise (e.g., patient specific planning), or they provide approximate results based on too simplistic models. With EView we provide the end user with a simple electroporation simulation workflow that is powerful enough to analyze complex geometries. We intentionally excluded the possibility of modeling heterogeneous tissues because that requires image segmentation and a more complex meshing process, both of which require expert user interaction and validation.

The approach of implementing EView as a web-server platform allows expert and non-expert electroporation users to rapidly obtain the electric field distribution in a computationally inexpensive manner. The implemented model has been validated against similar software. Execution times and server reliability have been reported, ensuring that the end user can obtain the electric field distribution in just 2 min (in the most simple cases).

Future versions of the platform will include a wider list of pre-specified tissues, as well as typical electrode configurations in clinical practice. Because, IRE produces considerable heat due to the Joule effect, tissue conductivity rises and leads to a slight increase of the treatment volume. We are planning on computing this margin and displaying it alongside the threshold isosurface. The possibility of including a two domain scenario (e.g., organ and tumor) to form a heterogeneous model will be explored. However, let us remark that this is supposed to be a platform with a straightforward workflow. Thus, simplicity will be prioritized. In addition, parallel computation will be assessed to reduce computation time.

Chapter 4

MODELING METHODS FOR IRREVERSIBLE ELECTROPORATION TREATMENT OVERLAP

Perera-Bel E, Mercadal B, García-Sánchez T, González Ballester MA, Ivorra A. Modeling methods for treatment planning in overlapping electroporation treatments. *IEEE Transactions on Biomedical Engineering*. 2021.
DOI: 10.1109/TBME.2021.3115029
Available at: *https://doi.org/10.1109/TBME.2021.3115029*

4.1 Introduction

Planning electroporation procedures consists in finding an electrode configuration that generates an electric field that surpasses the electric field threshold in the target tissue [94, 135, 238, 239]. It is common to use up to 6 electrodes to be able to reach the whole target tissue. In such scenarios, planning consists of simulating the electric field distribution for each electrode pair, and the overall treatment volume (TV) is estimated as the superposition (i.e., geometrical union) of treatments by each individual pair. That is, if the tissue receives sufficient electric field from at least one pair it is considered to be treated, otherwise it is assumed to be left unaffected [25, 225].

It is known that with longer pulses, more pulses, or shorter inter-pulse pause, electroporation occurs at lower electric fields [56–59]. Typically, protocols apply 10 to 100 consecutive pulses between each electrode pair to reduce the required field magnitude that induces electroporation. For a given protocol, the threshold is determined by comparing numerical simulations to experimental data. However, most of the findings are based on 2-electrode setups, in contrast to actual treatments that can use up to 6 electrodes to cover the whole target tissue [94, 135, 238, 239]. It is disputable that data obtained for 2-electrode setups can be directly translated for different configurations. By using more than one electrode pair, some regions of the tissue are treated multiple times with overlapping exposures (i.e., the tissue is treated with twice the pulse number, or more). Campelo *et al*. [198] characterized irreversible electroporation thresholds for prostate cancer tissue and found lower values than in similar studies that used less pairs. Among other reasons, they hypothesized that the lower field thresholds obtained were due to treatment overlap.

In a study involving irreversible electroporation in canine brain patients, Garcia *et al*. [113] proposed to model treatment overlap by, first, computing a scalar field of cell survival probability for each pair and, then, obtaining the field of probability of cell survival for the overall treatment

by combining the individual fields by multiplication. In particular, they used a statistical model known as Peleg-Fermi equation to compute the cell survival probability as a function of the number of pulses [109]. This multiplication approach is not possible when treatment characterization is based on an electric field threshold because in this situation the outcome is binary (i.e., cells are intact below the threshold and treated above it). Instead, the Peleg-Fermi model characterizes the transition from dead (i.e., treated) to living cells (i.e., untreated). This same methodology for modeling overlapping treatments has been used in a numerical study for treatment planning optimization [114].

Whereas the Peleg-Fermi model has been validated for various cell lines and tissues with single pair setups (i.e., 2 electrodes) [59, 109, 112, 240], there are no reports validating the overlapping model based on the multiplication of cell survival probabilities in a controlled environment, nor it has been proven that it is better than the simpler method based on the geometrical union of TVs.

The goal of this work is to quantify cell death due to treatment overlap in electroporation-based therapies, and to explore and evaluate methodologies for predicting TV for such scenarios. We performed an in vitro study on a layer of chinese hamster ovarian (CHO) cells covered with agarose gel. The study was divided into two phases. The characterization phase consisted of characterizing the electric field threshold and the cell death probability for pulsing protocols equivalent to those conventionally used for ECT and NTIRE with two overlapping treatments. In the validation phase we created a 2D treatment scenario where we compared and validated the accuracy of three different methods in predicting cell death for overlapping treatments.

4.2 Materials and methods

4.2.1 Cellular preparations

CHO cells were cultured in a T75 flask in Dulbeccos Modified Eagle Medium (DMEM) supplemented with 10 % fetal bovine serum and 1 % penicillin/streptomycin. Cells were grown in a humidified incubator at 37 °C and 5 % CO_2.

For preparing the samples for the assays, cells were initially washed with 2 ml of phosphate buffer saline (PBS). After a 2-minute trypsinization in 2 ml Trypsin at 37 °C, 4 ml of complete DMEM were added and centrifuged at 1200 rpm for 5 minutes. Supernatant was removed and cells were resuspended in culture medium at concentration of 50×10^3 cells/ml. Cells were seeded in a 24-well plate at a concentration of 50×10^3 cells/well. After 24 hours, a thin layer of low gelling temperature agarose (1 % in DMEM) was deposited on top of each cell monolayer. Agarose was heated at 70 °C to 80 °C to melt it and, subsequently, it was let to cool to 35 °C. Then, culture medium from the plates containing the cells was replaced by 300 µl of agarose solution per well and the plate was stored in a fridge (7 °C) for 5 minutes to ensure full solidification of the gel. Consecutively, 100 µl of DMEM were added to the wells and the plate was reintroduced in the incubator for 1 hour. The purpose of the agarose layer was to immobilize living and dead cells to the bottom of the culture plates. Otherwise, cells dying during the upcoming electroporation treatments would float in the medium and displace.

Before the electrical treatments, the wells were rinsed twice (500 µl per rinse) with low conductivity buffer (250 mM sucrose, 10 mM glucose, 10 mM NaCl, 5 mM KCl, 2 mM MgCl2, 10 mM HEPES, 1.8 mM $CaCl_2$, with pH 7.17, 2.5 mS/cm electrical conductivity, and osmolarity of 305 mOsm) to minimize electrolysis and thermal damage. The remaining buffer was removed, leaving only the adhered cells covered with the thin

layer of agarose gel during pulsing. After the treatment, 360 µl of DMEM were added to the well and the plate was stored at the incubator for 3 hours.

All assays were repeated at least three times on different days to account for experimental variations.

4.2.2 Pulsing protocols

Fig. 4.1.a displays the electrode configuration for the characterization phase. Each electrode setup consisted of two short-circuited sets of 4 stainless steel needles with a diameter of 1 mm arranged in line (2.67 mm separation between consecutive needles). The two linear needles arrays were obliquely arranged; the closest needles were separated 4 mm and the two furthest 7 mm. A CNC machined polycarbonate structure was glued to a 3D printed template to aid in needle placement (Fig. 4.1.d). This setup generated a linear electric field gradient along the horizontal axis in the central region between the two sets of electrodes. An 8 mm$\times$1 mm region of interest (ROI) along this x-axis was analyzed, hence, making it a 1D model (see Fig. 4.1.b and 4.1.c).

We defined two pulsing protocols equivalent to those typically used in ECT (trains of 10 pulses) and NTIRE (trains of 100 pulses). The pulses were applied at repetition frequency of 1 Hz and had a duration of 100 µs. Two trains of pulses (i.e., two treatments) were consecutively delivered. For each protocol, assays were performed with either a pause of 10 s or a pause of 1 minute between the two trains. These inter-train pauses were chosen according to what occurs during electroporation-based therapies with multiple pairs; between the activation of two consecutive pairs, it is required to wait for the generator to recharge (around 10 s), whereas non-consecutive pairs can be triggered one minute later (or more) after the first pair is completed.

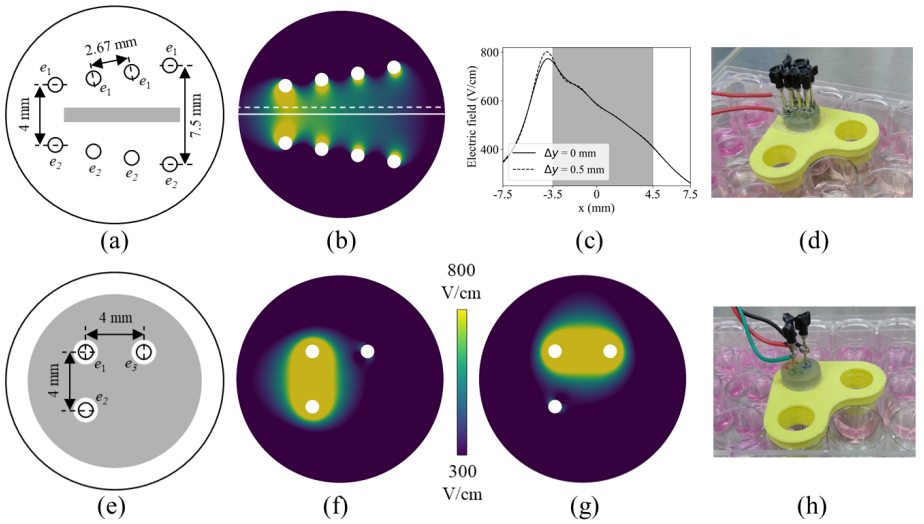

Figure 4.1: Electrode configurations for the characterization (a, b, c, d) and the validation (e, f, g, h) phases. (a), (e): Sizing and disposition of the electrodes. The shaded region corresponds to the analyzed ROI. (b): Electric field simulation at 300 V and (c) its distribution alongside the x-axis (solid line) and at 5 mm (dashed line). The analyzed ROI (8 mm×1 mm, shaded) shows an almost linear electric field gradient. (f), (g): Electric field simulation at 500 V between e_1 and e_2, and between e_3 and e_1, respectively. (d), (h): photo of the electrodes and their 3D printed holders.

In clinical electroporation procedures, it is typical to apply the same voltage-to-distance ratio across the different electrode pairs. Each portion of tissue then receives overlapping electric fields of different magnitudes (one magnitude per pair). Because the 1D model consisted of only one pair, we applied different voltages at each pulse train to generate two different electric fields. We applied a higher voltage in the first train and a lower voltage on the second (H+L), and vice versa (L+H). For each high voltage train, we applied a low voltage train at a ratio of 0, 0.25, 0.5, 0.75, and 1. For example, for a high voltage of 300 V, the voltage for a 0.25 ratio (25 %) corresponds to 300×0.25 = 75 V. Since the relationship between the applied voltage and electric field is linear

for a setup with constant electrical conductivity, these proportions can be directly translated to electric field magnitude. We refer as E_H and E_L to the electric field magnitudes generated with the high and low voltage trains, respectively. Notice that 0 % indicates that no low pulse train was applied, i.e., 100%+0% and 0%+100% are the same case. Three different high voltages were assayed for each protocol to account for experimental variability (Table 4.1).

Phase	Pulses per train	Voltage (100%)		
Characterization	10	240 V	300 V	360 V
	100	160 V	220 V	300 V
Validation	10	400 V	500 V	600 V

Table 4.1: Pulsing parameters.

This previous 1D model served to characterize the effects of treatment overlap, but it did not represent nor quantified the implications on real treatments. Thus, we validated the characterized models in a more realistic geometry. The validation assays consisted of a 2D setup with three needle electrodes in a right-angled triangle pattern. The electrode distance was 4 mm and the diameter 1 mm (Fig. 4.1.e). The same voltage was applied in both pulse trains (100%+100%), but electrode activation was changed, treating first across e_1 and e_2 (Fig. 4.1.f), and the then across e_3 and e_1 (Fig. 4.1.g). A 12 mm diameter circle delimited the ROI. In addition, within 0.8 mm radius from the center of the electrode, we observed clear signs of electrolysis (gas bubbles and in some cases a bit of gel disruption) in the protocols with the highest voltages. We discarded this region where non-IRE damage was evident, plus a 0.4 mm safety margin (0.8+0.4=1.2 mm radius, Fig. 4.1.e). We only report validation results for the 10 pulse protocols because we did not observe any significant increase in cell death between one and two consecutive 100 pulse treatments in the characterization phase.

Needles were replaced if visual inspection revealed signs of corrosion.

4.2.3 Imaging and Segmentation

Three hours after pulsing, the cells were co-stained for an hour at room temperature with calcein AM at 1 µM and with propidium iodide (PI) at 15 µM. The cells were imaged in a Zeiss Cell Observer fluorescence microscopy station (Carl Zeiss, Oberkochen, Germany). Two-channel images were obtained; calcein AM (green) for living cells and PI (red) for dead cells. Since the treated area was larger than the microscope field of view, the region was divided in tiles which were later stitched together (Figs. 4.2.a and 4.3.a).

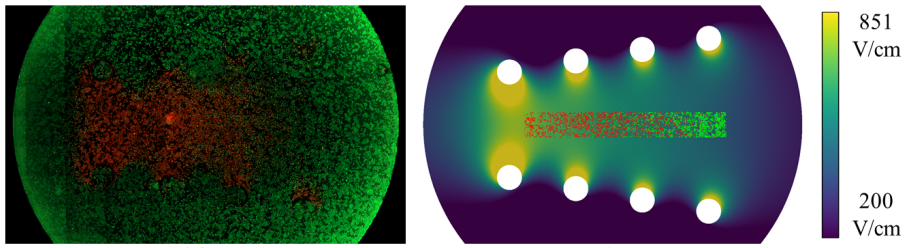

Figure 4.2: Fluorescence images and segmentations of the characterization setup. (a): fluorescence image of a treatment with two trains of 10 pulses at 300 V each with 10 s inter-pulse period with (b) the mapping of the segmented ROI to the electric field simulation. The 851 V/cm magnitude corresponds to the electric field threshold of a single 10 pulse train (found in this study).

The images were segmented using Fiji ImageJ [241–243]. The green channel was binarized automatically by local thresholding using Bernsen's method [243, 244], and the red channel by the robust automatic threshold selection algorithm [245]. The watershed filter was applied to the binary images to separate adjacent cells, and an opening operation removed remaining small particles. Lastly, the cells were filtered by size.

We numerically modeled the electric field. The segmented cell centroids were mapped to their corresponding locations in the simulated model to compare the state of the cell (alive/dead) with the received electric field

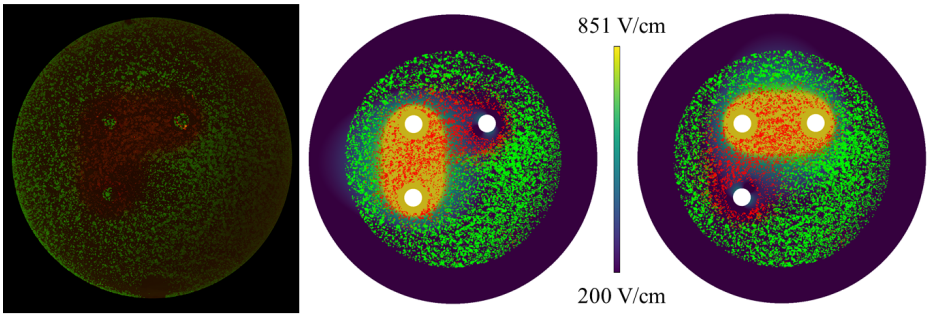

Figure 4.3: Fluorescence images and segmentations of the validation setup. (a) fluorescence image of a treatment with 10 pulse trains, 10 s protocol at 500 V with the segmented ROI overlayed on the electric field of the first pair (b) and of the second pair (d). The green channel corresponds to calcein AM staining (living cells) and the red channel to PI staining (dead cells). The 851 V/cm magnitude corresponds to the electric field threshold of a single 10 pulse train (found in this study).

(Fig. 4.2.b, and Fig. 4.3.b and 4.3.c). The electric field distribution was simulated with Elmer, with the methodology described in [246] under the assumption of constant electrical conductivity.

4.2.4 Characterization of cell survival

The standard electroporation model consists of simulating the electric field distribution to classify the electroporated tissue as the region with an electric field magnitude that surpasses a specific threshold. If multiple pairs are modeled, the electroporated tissue is simulated for each pair, and the overall TV is computed as the geometrical union of all the individual pairs.

Alternatively, cell death due to irreversible electroporation has been previously characterized using probabilistic models [59]. The probability

of cell survival (or cell death) is modeled as a function of the electric field magnitude and describes the transition from living to dead cells. The Peleg-Fermi model has been widely used because it not only parametrizes the dependence with the field magnitude but also allows expressing cell survival S as a function of the number of pulses [109]:

$$S = \frac{1}{1 + \exp\left(\frac{|E| - E_c(n)}{A(n)}\right)} \tag{4.1}$$

where E is the electric field magnitude, $E_C(n)$ is the electric field at which $S = 0.5$, and $A(n)$ is the factor which determines the slope of the transition of the curve. E_C and A are exponential decay functions dependent on the number of pulses n.

$$E_c(n) = E_{c0} \cdot \exp\left(-k_1 n\right) \tag{4.2}$$

$$A(n) = A_0 \cdot \exp\left(-k_2 n\right) \tag{4.3}$$

E_c describes the critical electric field at which 50 % of cells are dead, with E_{c0} being its initial magnitude and k_1 its exponential decay coefficient. A determines the transition from living to dead cells, with an initial value A_0 and a decay coefficient k_2.

However, since in the present work we independently evaluated protocols with a fixed number of pulses (either 10+10 or 100+100), the dependence on the number of pulses could be ignored. E_c and A become constants and the Peleg-Fermi model becomes a logistic regression:

$$S_t = \frac{1}{1 + \exp\left(-\left(\beta_0 + \beta_1 E\right)\right)} \tag{4.4}$$

with

$$\beta_0 = \frac{E_c}{A} \quad , \quad \beta_1 = \frac{-1}{A} \tag{4.5}$$

where, coarsely, β_0 determines the field magnitude at which the transition from living to dead cells occurs and β_1 describes its slope. Cell death probability is then defined as $1 - S_t$.

Based on the above, we characterized cell survival in the cases in which two overlapping treatments were applied. We fitted eq. (4.4) with the experimental data from the characterization (1D) setup for each of the *H+L* and *L+H* pulsing sequences independently. We used `R` (R Core Team) [247] with the generalized linear models (glm) [248] function to fit the data.

For every protocol, we derived the electric field threshold, which we determined to be the magnitude at which 95 % of cells were dead according to the fitted logistic regression. We also obtained a confidence interval of three times the standard error (3SE) of the logistic regression parameters (β_0 and β_1), which represented 99.7 % of the deviation. We considered that two protocols were different if the 3SE intervals did not overlap.

Second, we modeled survival probability as a function of the two overlapping treatments. Garcia *et al.* [113] proposed to evaluate treatment overlap as the joint probability of individual treatments, i.e., the probability of survival was computed for each treatment independently and multiplied:

$$S_{overlap} = \prod_i S_{t,i} \tag{4.6}$$

In their work, they used the Peleg-Fermi model to obtain the survival probability for each treatment of spontaneous malignant glioma. However, the Peleg-Fermi model is only calibrated on a single treatment, which ignores any dependency between the overlapping electric fields. For this reason, we adapted the logistic regression eq. (4.4) to also account for the overlapping treatment. A new parameter β_2 was added to characterize the influence of the second electric field in the survival probability. The adapted logistic model of overlapping treatments defines the survival probability (S_{tt}) as:

$$S_{tt} = \frac{1}{1 + \exp\left(-\left(\beta_0 + \beta_1 E_i + \beta_2 E_j\right)\right)} \tag{4.7}$$

where E_i is the electric field generated in treatment i and E_j is the electric

field from the other treatment j. The contribution of all treatments is combined again with eq. (4.6). For the present study with two treatments

$$S_{overlap} = \prod_i S_{tt,i} = S_{tt,1} \cdot S_{tt,2i}$$

$$S_{tt,1} = \frac{1}{1 + \exp\left(-\left(\beta_0 + \beta_1 E_1 + \beta_2 E_2\right)\right)} \tag{4.8}$$

$$S_{tt,2} = \frac{1}{1 + \exp\left(-\left(\beta_0 + \beta_1 E_2 + \beta_2 E_1\right)\right)}$$

We fitted this equation to characterize cell death as a function of the two overlapping electric fields. We used the data from all the *H+L* and *L+H* protocols, which contained all possible combinations of E_H and E_L fields. We only report fittings for the 10 pulse protocols since we did not observe any significant difference regarding cell survival between treatments consisting of one train or two trains of 100 pulses in the 1D configuration.

4.2.5 Assessment of predictive accuracy

We used the validation (2D) setup to analyze the predictive accuracy in overlapping treatments for three modeling methodologies: A) to model treatment overlap by obtaining the overall treatment volume (surface in this case) as the geometrical union of the individual treatments (as predicted by the field threshold criterion), B) to model treatment overlap by computing the field of cell survival probability as the product of the survival probability of individual treatments (S_t) (eq. (4.6)), and C) to model treatment overlap by computing the field of cell survival probability as the product of the adapted logistic model of overlapping treatments S_{tt} (eq. (4.8)). Methods A and B are known, and method C is the new method we propose here. For method A we used the electric field thresholds obtained from the 100%+0% protocols. For method B we

used the survival curve of the 100%+0% protocol. Method C was fitted with all the characterization data. The methods were only evaluated for the 10 pulse protocols.

For each method, we computed the precision and miss rate metrics, as well as the Dice similarity coefficient:

$$\text{Precision} = \frac{TP}{TP + FP} \tag{4.9}$$

$$\text{Miss rate} = \frac{FN}{FN + TP} \tag{4.10}$$

$$\text{Dice} = \frac{2TP}{2TP + FP + FN} \tag{4.11}$$

TP is the true positive, TN the true negative, FP the false positive and FN the false negative. Additionally, we computed the area under the curve (AUC) of the receiver operating characteristic (ROC) curve to evaluate the overall classification accuracy regardless of the threshold [249]. Because we were predicting cell death, we considered dead cells as positives and living cells as negatives. For method A, a cell was classified as dead if it received an electric field above the IRE threshold. For methods B and C, a cell was classified as dead if its simulated probability of survival was below 5 %.

4.2.6 Estimation of overlap implications in tissues

We performed some preliminary 3D simulations to extrapolate the findings of the 2D cell culture assays to scenarios resembling actual electroporation-based treatments. We compared the predicted TVs in overlapping treatments with the three studied methodologies for 10-pulse treatments. Three electrode configurations typically used in electroporation-based therapies, and in particular in NTIRE procedures, were simulated, and the ablated volume (irreversibly electroporated)

was obtained. Three setups were considered: 4-SQ) four electrodes in a square pattern at 15 mm separation, 20 mm length and 1 mm diameter, 6-RECT): two parallel lines of three electrodes in parallel (forming a rectangle) at 15 mm separation, 20 mm length and 1 mm diameter, and 7-HEX) six electrodes forming a hexagon with one electrode in the center at 7.3 mm separation, 20 mm length and 0.7 mm diameter.

Two voltage to distance ratios were considered for the treatments: 1000 V per cm and 1500 V per cm between active electrodes. We limited the voltage to 3000 V, which is the maximum in most commercial generators. See the simulated voltages in Table 4.2.

	Voltage/distance ratio (V per cm)	Voltage (V)	
		In-line pairs	Diagonal pairs
4-SQ	1000	1500	2121
	1500	2250	3000
6-RECT	1000	1500	2121
	1500	2250	3000
7-HEX	1000	730	
	1500	1095	

Table 4.2: Simulated voltages.

As it has been demonstrated that tissue electrical conductivity rises during electroporation, which affects the overall electric field distribution, here, for higher verisimilitude, the simulation was performed on a 3D homogeneous domain assuming a non-linear electrical conductivity. The conductivity profile followed a symmetric sigmoid function and had been fit to *ex vivo* porcine liver data [87, 88].

$$\sigma(E) = \sigma_0 + \frac{\sigma_{max} - \sigma_0}{1 + A \exp\left(-\frac{|E|-B}{C}\right)} \tag{4.12}$$

where E is the electric field magnitude and σ_0 is the (static) conductivity

when no electric field is applied (0.188 S/m), σ_f is the maximum conductivity that can be reached during electroporation (0.289 S/m), and A (80.03), B (613.14 V/cm) and C (252.2 V/cm) are shape parameters.

Impact on field distribution that preceding treatments can have on subsequent treatments due to conductivity changes caused by electroporation

In addition to simulating the in-pulse conductivity, we modeled the static conductivity to be influenced by the preceding pulses. It has been observed that after a sequence of pulses, the static conductivity is larger than it was before the treatment [39]. This phenomenon has not been previously modeled, but, as an extreme upper bound to this effect, we defined the static conductivity ($\sigma_{0,i}$) to be the average between σ_0 and the previous pair conductivity $\sigma_{i-1}(E)$:

$$\sigma_{0,i} = \frac{\sigma_0 + \sigma_{i-1}(E)}{2} \tag{4.13}$$

Notice that this is an extreme assumption, thus, the effect in real scenarios should be much lower. Eq. (4.12) is then modified:

$$\sigma(E) = \sigma_{0,i} + \frac{\sigma_{max} - \sigma_0}{1 + A \exp\left(-\frac{|E|-B}{C}\right)} \tag{4.14}$$

4.3 Results

4.3.1 Model characterization

We first modeled cell survival as a function of the electric field eq. (4.4) for a single pulse train (100%+0%) and for two consecutive trains at E_H

(100%+100%) (Fig. 4.4 and Table. 4.3). On one hand, applying a second sequence of 10 pulses substantially reduced the electric field threshold from 851 V/cm to 773 V/cm with a 1 minute resting pause. The drop was even more accentuated with a 10 s pause, reaching 711 V/cm. This reduction was still observed considering the 3SE interval. On the other hand, no significant differences were observed in the 100 pulse protocols, with a single train threshold of 613 V/cm, and two train thresholds of 621 V/cm and 606 V/cm for 1 minute and 10 s inter-train pauses, respectively.

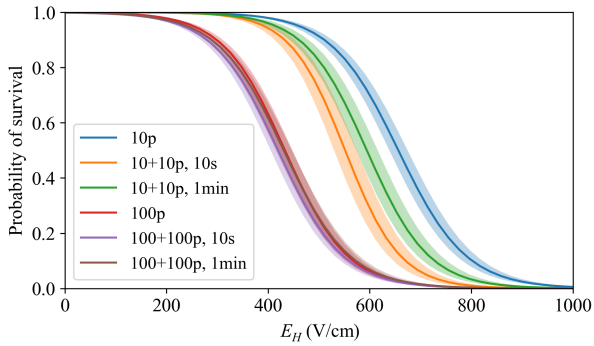

Figure 4.4: Characterization of cell survival probability as a function of the electric field magnitude (1) when exposed to a single or two trains of 10 or 100 pulses. The assays were performed with three different voltages (Table 4.1). In the cases of two trains, the voltage for both sequences was the same. The shading corresponds to $\pm$3SE.

For the 10 pulse protocol, we characterized treatment overlap with two different electric fields by applying *H*+*L* and *L*+*H* trains. The results are presented in Table. 4.3 and Fig. 4.5. In the 10 s group with *H*+*L* pulsing, there is a tendency of higher cell death with E_L of 50% and 75% (thresholds of 807 V/cm and 790 V/cm, respectively). However, the 3SE region of the 50% case overlaps with the 0% one. A similar trend is found with the 1 minute *H*+*L* protocols, but the intervals for all the combinations overlap with the 100%+0%. In the 10 s *L*+*H* case only E_L=75% presents a higher death ratio, and no effect is observed with

Pulses	Period	Voltage strength	Threshold (V/cm)	+3SE (V/cm)	-3SE (V/cm)
10 + 10	10 s	100%+0%	851	876	828
		100%+25%	877	920	837
		100%+50%	807	846	771
		100%+75%	790	824	757
		100%+100%	711	741	682
		100%+0%	851	876	828
		25%+100%	844	882	807
		50%+100%	846	883	810
		75%+100%	796	831	763
		100%+100%	711	741	682
	1 min	100%+0%	851	876	828
		100%+25%	877	920	837
		100%+50%	839	878	802
		100%+75%	807	846	770
		100%+100%	803	843	765
		100%+0%	851	876	828
		25%+100%	805	838	773
		50%+100%	816	850	784
		75%+100%	831	867	798
		100%+100%	773	802	745
100 + 100	—	100%+0%	613	634	593
	10 s	100%+100%	606	628	586
	1 min	100%+100%	621	643	599

Table 4.3: Electric field thresholds for two trains of variable voltage at 10 s and 1 minute inter-pulse period. The thresholds were determined to be the magnitude at which 95 % of cells were dead according to the logistic regressions. See Figures 4.4 and 4.5 for the logistic curves.

a 1 minute pause. These same findings can be observed in Fig. 4.5.a and 4.5.b where below E_L=50% the survival distribution does not change, but at 75% and 100% cells are killed at lower electric fields. The fitting parameters of the logistic regression (eq. (4.4)) for all *H*+*L* and *L*+*H* protocols are displayed in Table 4.4.

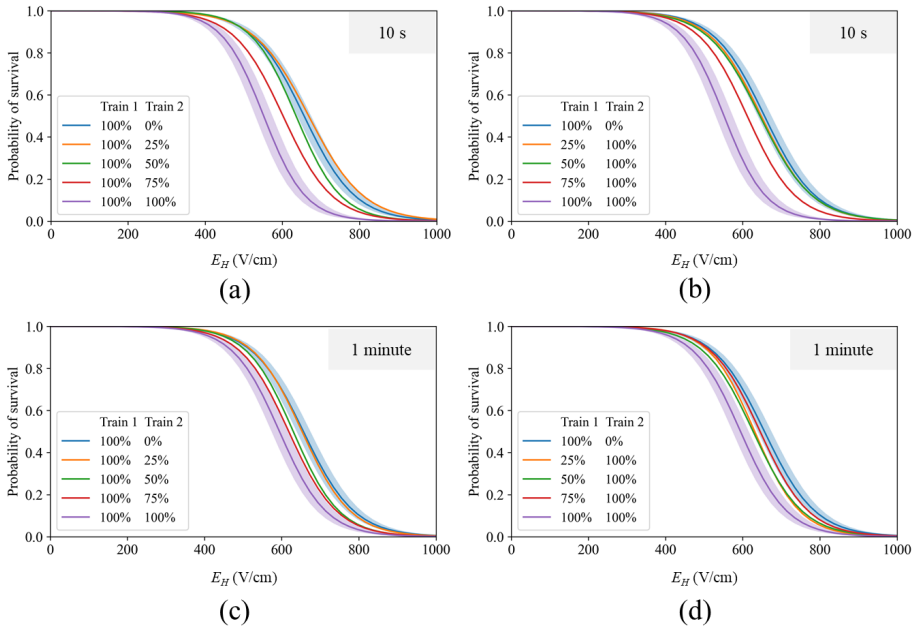

Figure 4.5: Fitting of the survival probability of *H*+*L* (a, c) and *L*+*H* (b, d) trains (10 pulse trains). Inter-pulse period of 10 s (a, b) and 1 minute (c, d). The notation 0 % is just to indicate that no voltage was applied. The shading corresponds to ± interval of the fitting, and they are only represented in the 100%+0% and 100%+100% cases to ease image interpretation. All 3SE intervals are displayed in Table. 4.3.

Fig. 4.6 displays a heatmap representation of survival probability for all the *H*+*L* and *L*+*H* protocols (colored stripes) and the predicted contours using the three proposed methods. It can be observed that the method we propose here, C (dashed line), which truly models the effect of overlapping treatments (S_{tt}), fits the experimental data better than the

method proposed by Garcia *et al.*, B (solid line), in which the probability of survival for the overall treatment is computed as the product of the probability of survival of the individual treatments (S_t).

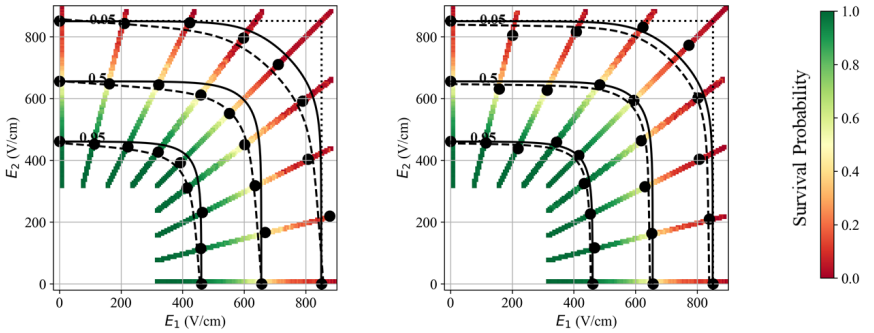

(a) (b)

Figure 4.6: Representations of experimental and modeled cell survival probabilities of the data from the characterization phase for the 10 pulse protocols at 10 s (a) and 1 minute (b) inter-pulse pauses. Each of the colormap stripes corresponds to experimental data from a *H*+*L* or *L*+*H* protocol, with the black circles being their probability of survival at 0.95, 0.5 and 0.05. The dotted line indicates the boundary for ensuring cell death (probability of survival = 0.05) according to the electric field threshold criterion (method A). The solid lines indicate isocontours of the probability of survival computed as the product of the survival probabilities of the two individual treatments (method B). Notice that method B is the same for 10 s and 1 minute pause treatments. The dashed lines indicate isocontours of the probability of survival computed as the product of the adapted logistic model of overlapping treatments (method C).

Coefficients of the models

Table 4.4 shows the coefficients of the logistic regression fittings (eq. 4.4) for all the *H*+*L* and *L*+*H* curves displayed in Figures 4.4 and 4.5. For method B, the coefficients are the ones displayed of the 100%+0% protocol (bold). The coefficients of method C are displayed in Table 4.5.

Pulses	Period	Voltage strength	β_0			β_1 (cm/V)		
			Mean	±3SE		Mean	±3SE	
10 + 10	10 s	100%+0%	**9.913**	**9.782**	**10.046**	**-1.51·10^{-2}**	**-1.53·10^{-2}**	**-1.49·10^{-2}**
		100%+25%	9.409	9.204	9.617	-1.41·10^{-2}	-1.44·10^{-2}	-1.38·10^{-2}
		100%+50%	10.895	10.663	11.131	-1.71·10^{-2}	-1.75·10^{-2}	-1.68·10^{-2}
		100%+75%	9.435	9.244	9.627	-1.57·10^{-2}	-1.60·10^{-2}	-1.53·10^{-2}
		100%+100%	10.204	10.002	10.410	-1.85·10^{-2}	-1.89·10^{-2}	-1.81·10^{-2}
		100%+0%	9.913	9.782	10.046	-1.51·10^{-2}	-1.53·10^{-2}	-1.49·10^{-2}
		25%+100%	9.746	9.543	9.952	-1.50·10^{-2}	-1.54·10^{-2}	-1.47·10^{-2}
		50%+100%	9.438	9.245	9.633	-1.46·10^{-2}	-1.50·10^{-2}	-1.43·10^{-2}
		75%+100%	9.759	9.563	9.958	-1.60·10^{-2}	-1.63·10^{-2}	-1.56·10^{-2}
		100%+100%	10.204	10.002	10.410	-1.85·10^{-2}	-1.89·10^{-2}	-1.81·10^{-2}
	1 min	100%+0%	9.913	9.782	10.046	-1.51·10^{-2}	-1.53·10^{-2}	-1.49·10^{-2}
		100%+25%	10.327	10.113	10.544	-1.58·10^{-2}	-1.62·10^{-2}	-1.55·10^{-2}
		100%+50%	10.493	10.263	10.727	-1.67·10^{-2}	-1.70·10^{-2}	-1.63·10^{-2}
		100%+75%	9.863	9.638	10.091	-1.60·10^{-2}	-1.63·10^{-2}	-1.56·10^{-2}
		100%+100%	9.795	9.625	9.968	-1.65·10^{-2}	-1.68·10^{-2}	-1.62·10^{-2}
		100%+0%	9.913	9.782	10.046	-1.51·10^{-2}	-1.53·10^{-2}	-1.49·10^{-2}
		25%+100%	10.673	10.473	10.876	-1.69·10^{-2}	-1.73·10^{-2}	-1.66·10^{-2}
		50%+100%	9.764	9.578	9.952	-1.56·10^{-2}	-1.59·10^{-2}	-1.53·10^{-2}
		75%+100%	10.189	9.992	10.389	-1.58·10^{-2}	-1.61·10^{-2}	-1.55·10^{-2}
		100%+100%	9.795	9.625	9.968	-1.65·10^{-2}	-1.68·10^{-2}	-1.62·10^{-2}
100 + 100	—	100%+0%	7.087	6.970	7.206	-1.64·10^{-2}	-1.66·10^{-2}	-1.61·10^{-2}
	10 s	100%+100%	6.599	6.485	6.714	-1.57·10^{-2}	-1.60·10^{-2}	-1.55·10^{-2}
	1 min	100%+100%	6.679	6.559	6.801	-1.55·10^{-2}	-1.58·10^{-2}	-1.52·10^{-2}

Table 4.4: Coefficient (mean±3SE) of the the *H*+*L* and *L*+*H* models (eq. (4.4)). The coefficients of method B are highlighted in bold.

Protocol	β_0			β_1 (cm/V)			β_2 (cm/V)		
	Mean	±3SE		Mean	±3SE		Mean	±3SE	
10+10 10 s	9.648	9.461	9.835	-1.47·10^{-2}	-1.50·10^{-2}	-1.44·10^{-2}	-1.10·10^{-3}	-1.20·10^{-3}	-1.00·10^{-3}
10+10 10 min	9.919	9.732	10.105	-1.53·10^{-2}	-1.56·10^{-2}	-1.50·10^{-2}	-2.00·10^{-4}	-2.90·10^{-4}	-1.11·10^{-4}

Table 4.5: Coefficients (mean±3SE) of the adapted logistic regression of overlapping pairs (method C).

4.3.2 Model validation

After the characterization of the three models, we used a 2D setup to analyze their predictive accuracy of the studied models. Fig. 4.7 shows heatmap representations of the survival density of the validation experiments. The results replicate the findings from the characterization models. Cells that received overlapping treatments with $E_L \geq 75\%$ showed a lower survival density, and a higher death ratio was accomplished with 10 s pause than with 1 minute pause.

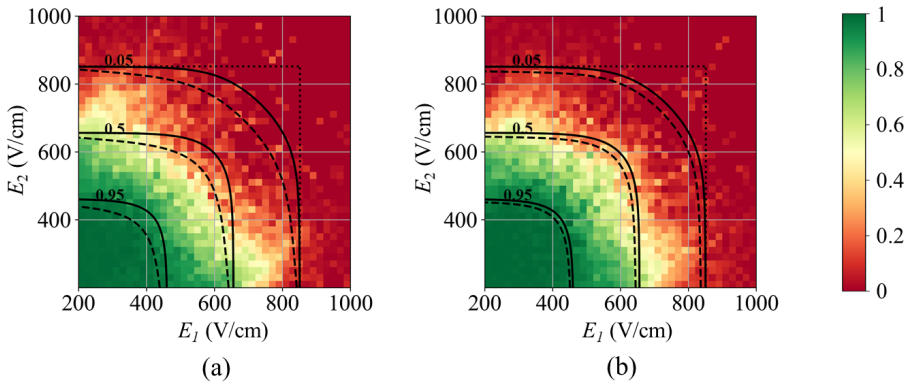

Figure 4.7: Heatmap representations of cell survival density of the validation phase as a function of the field magnitudes of the two overlapping treatments. Treatment protocols of 10+10 pulses at 10 s (a) and at 1 minute (b) inter-train pauses. E_1 corresponds to the electric field generated between e_1 and e_2 (Fig. 4.1.f) and E_2 is the field between e_3 and e_1 (Fig 4.1.g). The heatmap is divided in 20 V/cm bins. The dotted line displays the electric field threshold (method A). The 5 %, 50 %, and 95 % survival probabilities are represented in the solid and dashed lines for method B and C, respectively (same curves as in Fig. 4.6).

The predictive accuracy of the three methods for modeling treatment overlap is shown in Table 4.6. All methods are equally good in classifying dead cells, with all of them having a precision >0.982 and

a maximum difference of 0.004. However, methods B and C classify slightly better the living cells over A, indicated by lower miss rate, which leads to an increased Dice score (0.009 percent points for B and 0.023-0.030 for C). Overall, all methods are very accurate at classifying the state of cells (alive or dead), with an AUC>0.961 (and less than 0.003 difference between methods). These differences in classification are also displayed in Fig. 4.8 were we computed the predicted treatment area.

Protocol	Method	Precision	Miss rate	Dice	AUC
10+10 10 s	A	0.986	0.343	0.788	0.961
	B	0.986	0.331	0.797	0.962
	C	0.982	0.300	0.818	0.964
10+10 10 min	A	0.990	0.353	0.782	0.967
	B	0.989	0.341	0.791	0.968
	C	0.987	0.321	0.805	0.969

Table 4.6: Metrics of the predictive power of the three proposed methods. a) electric field threshold, b) product of individual pairs, c) product of the adapted logistic model of overlapping electric fields.

In the 100 and 100+100 pulses protocols we observed signs of electrolysis around the needles, both in needles acting as anodes and in the needles acting cathodes. DMEM contained phenol red, which colored the surroundings of the electrodes in yellow (around the anode) and pink (around the cathode) due to pH change. We also observed gas bubbles. These signs were mild with a single treatment, but much noticeable with two consecutive trains. Additionally, we monitored the applied voltage and the electric current. No significant changes were observed in any treatment.

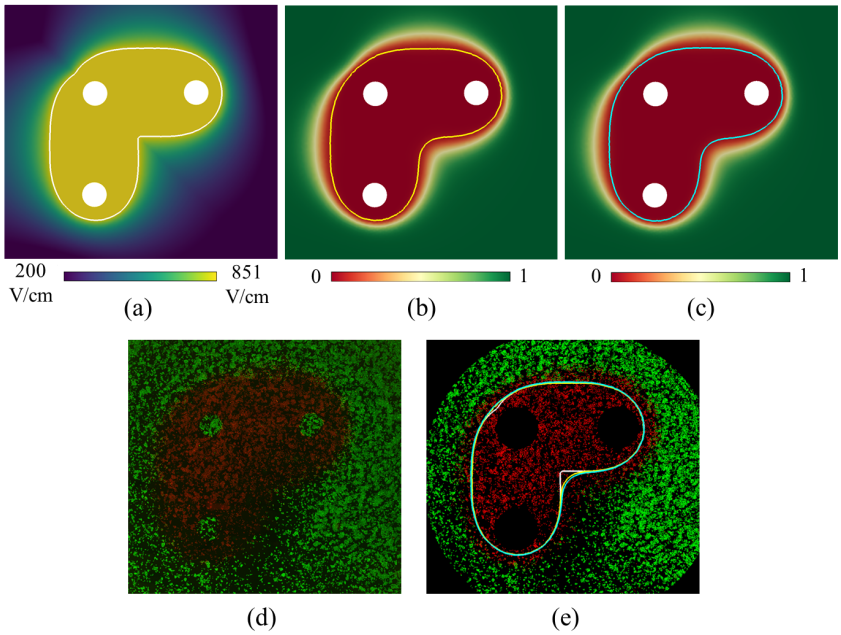

Figure 4.8: Predicted treated area with the three analyzed methods for a protocol of two trains of 10 pulses at 600 V, 1 minute pause. (a) electric field distribution (white contour at the irreversible electric field threshold of 851 V/cm). (b) probability of survival of the product of individual pairs (yellow contour at 95 % cell death). (c) probability of survival of the adapted logistic model of overlapping electric fields (cyan contour at 95 % cell death). (d): original image with calcein AM in the green channel (living cells) and PI in the red channel (dead cells) (e): segmentation of the ROI with an overlay of the isocontours at the defined critical values for the three methods (same colors as in (a), (b) and (c)).

4.3.3 Predicted treatment volume in th 3D tissues

We performed 3D simulations on electrode configurations typically found in actual electroporation-based treatments to compare the predicted IRE volume with the three studied models. For method A, an electric field threshold of 851 V/cm was used (corresponding to 95 % of cell death

of a single treatment of 10 pulses). For methods B and C, the ablated volume was set to be that which had a survival probability of 5 % or lower. Because method C was calibrated only for two overlapping treatments, the survival probability was only computed using the two trains that generated the highest electric fields (at each mesh node).

The predicted volumes are reported in Table 4.7 and are displayed in Figs. 4.9, 4.10, and 4.11. Using method A as a baseline, an increment in the overall volume of 13.7 ± 5.5 % was found with method B. Method C showed a slightly larger volume, 15.3 ± 5.8 % with 1 minute pause and 22.9 ± 8.6 % with 10 s pause, both with respect to A.

Electrode configuration	Voltage/distance ratio (V per cm)	Predicted TV (cm^3)			
		A	B	C (1 minute)	C (10 s)
4-SQ	1000	4.80	5.27	5.44	5.85
	1500	10.77	12.32	12.51	13.17
6-RECT	1000	7.42	8.52	8.63	9.32
	1500	17.03	20.00	20.11	21.17
7-HEX	1000	1.69	2.04	2.08	2.29
	1500	5.10	5.34	5.35	5.50

Table 4.7: Predicted treatment volume with the three studied methods for the different electrode configurations and pulsing parameters.

In addition to simulating the in-pulse conductivity, we also modeled the impact on field distribution that preceding treatments can have on subsequent treatments due to conductivity changes caused by electroporation (eq. 4.14) to analyze if it can further influence treatment overlap. The predicted volumes are reported in Table 4.8 and are displayed in Fig. 4.12. The effect was minimal, with an average difference of 0.7 %.

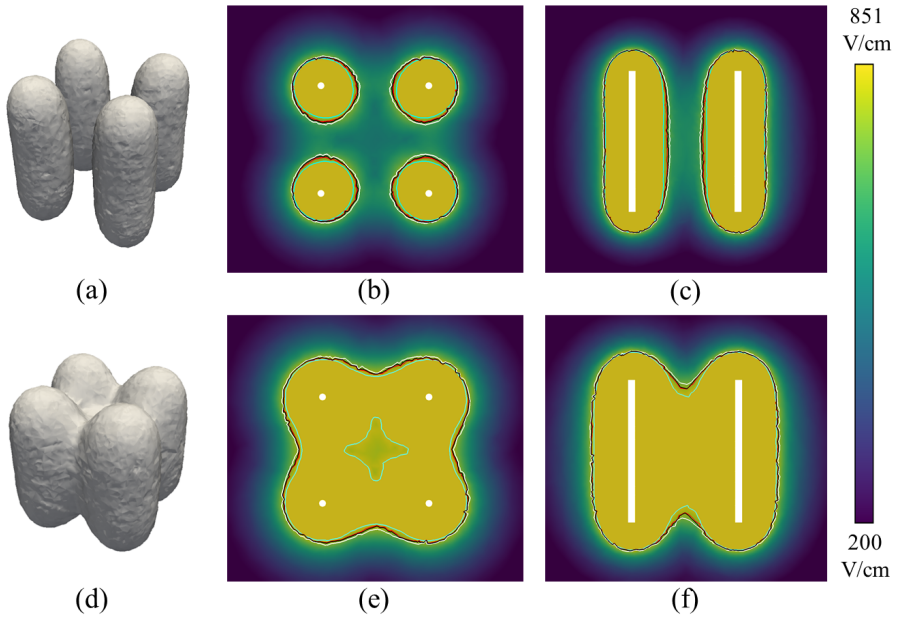

Figure 4.9: Predicted ablated volume in the 4-SQ setup. Electrode spacing is 15 mm and the diameter is 1 mm. (a), (b), and (c) correspond to the treatment at 1000 V per cm voltage to distance ratio, and (d), (e), and (f) correspond to the simulation with 1500 V per cm. (a) and (d) display the predicted volume for method C at 10 s inter-treatment pause. (b) and (e) are the transversal cross section and (c) and (f) are the longitudinal cross section with the simulated electric field distribution. The contours correspond to the predicted TV for method A (cyan), method B (red), method C for 1 minute inter-treatment pause (black), and method C for 10 s pause (white).

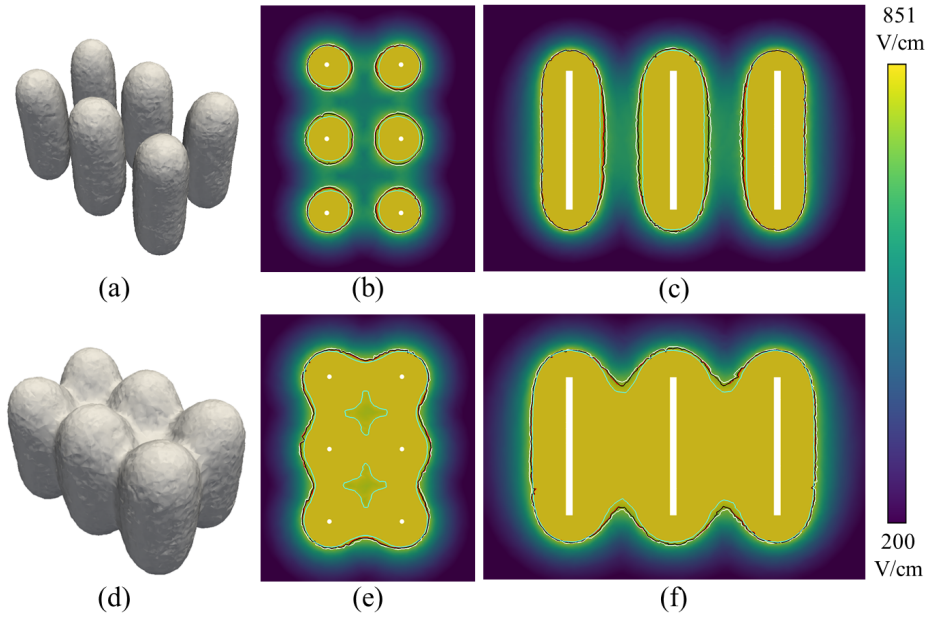

Figure 4.10: Predicted ablated volume in the 4-SQ setup. Electrode spacing is 15 mm and the diameter is 1 mm. (a), (b), and (c) correspond to the treatment at 1000 V per cm voltage to distance ratio, and (d), (e), and (f) correspond to the simulation with 1500 V per cm. (a) and (d) display the predicted volume for method C at 10 s inter-treatment pause. (b) and (e) are the transversal cross section and (c) and (f) are the longitudinal cross section with the simulated electric field distribution. The contours correspond to the predicted TV for method A (cyan), method B (red), method C for 1 minute inter-treatment pause (black), and method C for 10 s pause (white).

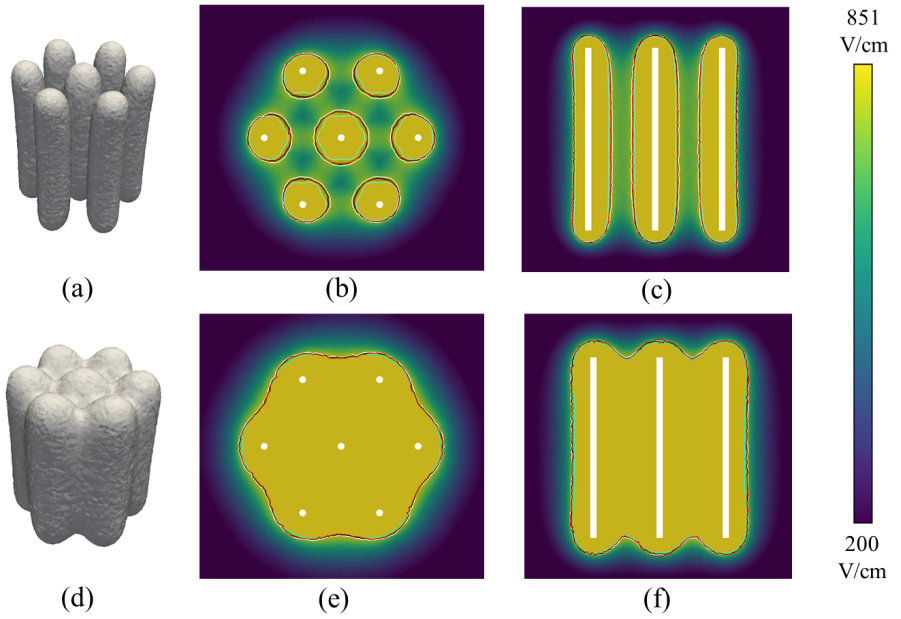

Figure 4.11: Predicted ablated volume in the 7-HEX setup. Electrode spacing is 7.3 mm and the diameter is 0.7 mm. (a), (b), and (c) correspond to the treatment at 1000 V per cm voltage to distance ratio, and (d), (e), and (f) correspond to the simulation with 1500 V per cm. (a) and (d) display the predicted volume for method C at 10 s inter-treatment pause. (b) and (e) are the transversal cross section and (c) and (f) are the longitudinal cross section with the simulated electric field distribution. The contours correspond to the predicted TV for method A (cyan), method B (red), method C for 1 minute inter-treatment pause (black), and method C for 10 s pause (white).

Electrode configuration	Voltage/distance ratio (V per cm)	Difference in predicted TV (%)			
		A	B	C (1 minute)	C (10 s)
4-SQ	1000	0.23	0.44	0.43	0.47
	1500	0.16	0.22	0.20	0.21
6-RECT	1000	0.27	0.47	0.43	0.47
	1500	0.19	0.20	0.17	0.17
7-HEX	1000	0.97	1.23	1.28	1.36
	1500	0.26	0.32	0.30	0.32

Table 4.8: Difference of the predicted TV obtained with and without considering the impact on field distribution that preceding treatments can have on subsequent treatments due to conductivity changes caused by electroporation.

4.4 Discussion

According to the obtained results, and as expected, treatment overlap can substantially increase irreversible electroporation damage. Cell death rises when two high electric field treatments were sequentially applied.

It is known that a higher number of pulses reduces the irreversible electric field threshold, which tends to saturate at around 70 to 100 pulses [59]. In the 10 pulse protocols, the saturation point was not reached, as we observed that a second train reduced cell viability. Instead, in the 100 pulse protocol, the second train did not add to cell death.

Another factor which reduces the electric field threshold is inter-pulse pause. It has been reported that cell membrane needs from seconds to a few minutes to recover from electroporation. However, if a pulse is applied before the membrane has fully recovered, the membrane is further electroporated [57]. Although we were studying the pause between two trains (instead of pulses), the general effect also applies. This explains

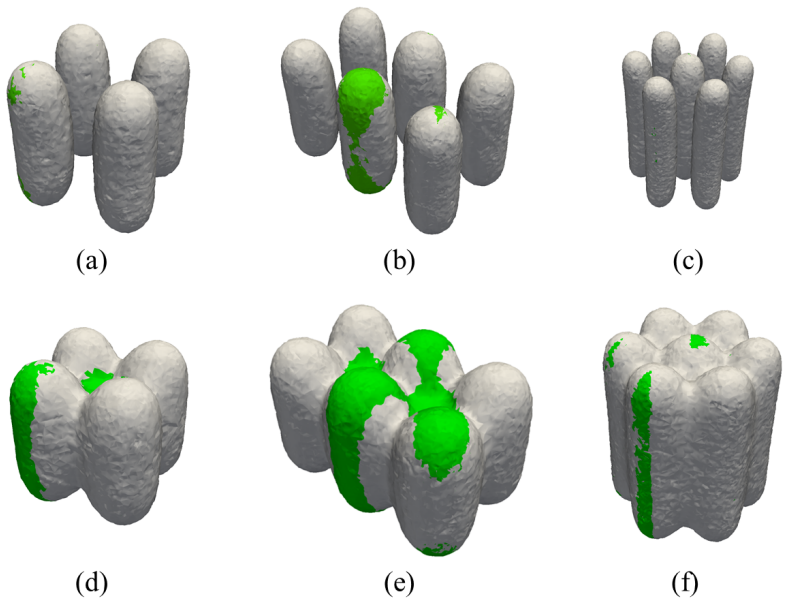

Figure 4.12: Predicted IRE volume (method C at 10 s pause) using two different electrical conductivities. The green isosurface corresponds to the simulation with only in-pulse conductivity changes (eq. 4.12) and the white isosurface represents the simulation that also considers the preceding pair conductivity change (eq. 4.14). The two surfaces are overlayed on top of each other, and it can be observed that the differences are minimal. The top row (a, b and c) are the simulations at 1000 V per cm voltage to distance ratio, and the bottom row (d, e and f) are at the simulation with 1500 V per cm. The electrodes configurations are 4-SQ (a, d), 6-RECT (b, e), and 7-HEX (c, f).

why lower survival probabilities were found with the 10 s pause compared to 1 minute pause.

Interestingly, the order of the treatments (i.e., whether the higher field treatment is first or second) did not produce observable differences in the outcome. Yao *et al*. [250] found that applying short high voltage pulses (a few kV/cm for a couple of microseconds) before a standard 80 NTIRE pulses generated a larger ablation area than with the standard NTIRE

protocol on potato tuber. Pulsing the other way around did not increase the treated area. The voltage to distance ratios they used for the high pulses were of the order of 3-4 kV/cm, which were up to 10 times larger than the low fields. In our study, we did not surpass 1.5 kV/cm for the high pulses, and proportionally the low electric fields were not as low (25 % ratio). These lower fields could explain why we did not observe any difference between *H*+*L* and *L*+*H* protocols, i.e., the order of the overlapping fields did not add to cell death.

Three different methods were compared to predict cell death in overlapping treatments: A) the geometrical union of the individual treatments, B) the method proposed by Garcia *et al*. [113] in which the overall treatment is obtained by multiplying the fields of probability of cell survival from the individual treatments, and C) our adapted logistic model of overlapping treatments. We computed precision (eq. (4.9)), miss rate (eq. (4.10)) and Dice (eq. (4.11)) metrics, after classifying the state of the cell with a threshold of 851 V/cm (IRE threshold) for method A, and a 5 % cell survival probability for methods B and C. A precision of 1 indicates that the predicted treatment region contains only dead cells, whereas lower values reveal the proportion of remaining living cells. In this regard, we found that all the methods perform equally well, with a precision ≥ 0.982 and a maximum difference of only 0.4 percent points. On the other hand, the miss rate revealed differences between the methods. This metric represents the proportion of dead cells that fall outside the treatment region. Higher scores indicate a larger transition of living/dead cells. In this case, we found that methods B and C perform slightly better than the electric field threshold criterion (1.2 to 4.3 percent points lower), with C marginally outperforming B by up to 3.1 points. This reduction in miss rate is also reflected in the Dice score. In addition, the AUC metric reveals how accurate a classifier is regardless of the threshold. It confirms that all the methods perform great (AUC > 0.961), with method B and C taking the lead by a minimal margin.

These slight improvements can be graphically understood by observing

the shape of the ablation area that our 2D setup generated (L-shaped). It can be seen in Fig. 4.8.e that the isocontour provided by the electric field threshold criterion (method A) presents a sharp angled corner, whereas that same corner is smoother with the other two methods. Despite the slight accuracy improvements offered by methods B and C, these results suggest that, considering other sources of uncertainty typically present in electroporation treatment (e.g., placement of the electrodes), overall, the electric field threshold method can be considered as accurate as the probabilistic models in predicting the treatment region.

This suggests that for NTIRE procedures, which typically apply between 70 and 100 pulses per pair, treatment overlap does not play a significant role (we only observed an increase in cell death with overlapping treatments with 10 pulse protocols, and not with 100 pulses). However, this study only contemplated two overlapping pulse trains, contrary to actual procedures which can present more overlapping treatments, although marginal differences can be presumed.

On the other hand, ECT aims to reversibly electroporate the tissue so the therapeutic drug can penetrate into the cells, but it is not uncommon to find damage due to IRE near the electrodes. Due to the lower pulse count per train (8 to 10 pulses), overlapping treatments can slightly enlarge the irreversibly treated tissue around the electrodes, according to our results. This can be further confirmed by some preliminary 3D simulations, where the predicted IRE lesion volume was increased by $13.7 \pm 5.5\,\%$ (mean$\pm$standard deviation) with B, and up to $22.9 \pm 8.6\,\%$ with C when compared to A (Table 4.7).

It must be pointed out that the modeling methods do not fit the validation data as well as they fit the characterization data. In the 1D setup, the reduced cell viability due to overlapping fields follows a curved shape (Fig. 4.6), but that shape appears straighter when looking at the data from the validation phase (Fig. 4.7). Although this effect can be partially accounted by experimental uncertainty (we are reporting a 3SE interval of around ± 30 V/cm), this effect could also be a consequence of the highly

different electric field distributions between the two setups. While in the characterization assays the electric field in the two treatments had the same direction, in the validation setup we applied two fields at different angles (up to 90 degrees). Membrane polarization mostly occurs at the surfaces which are perpendicular to the electric field [251]. This implies that in the 1D setup the cell membrane was always polarized in the same region. Instead, in the 2D assays, the first and second trains polarized the membrane in different directions. Thus, there was a larger polarized area in the 2D setup. This suggests that cells in the validation setup presented a larger electroporated membrane area [75], which could add to cell death [252].

Another limitation of the assays is that cell death does not reach 100 %, even well above the electric field threshold (Fig. 4.7). This is reflected in the precision metric where no method surpasses 97.5 %. In some images, we observed noise speckles in the calcein AM channel. We filtered the cells by size, but some of the noise bypassed it. We also observed living cells within the ablation zone in most of the images. However, such cells were no longer adhered to the well surface. It is likely that these cells were still in an apoptotic process after the 3-hour period we analyzed. It has been reported that 24 hours is a better interval for evaluating apoptosis due to IRE [158, 253, 254], but we found in preliminary assays that cell proliferation overtook the treatment zone after 24 hours.

Finally, the present study is not considering the possible impact of conductivity changes caused by electroporation. In the cell models used here the conductivity changes due to electroporation are likely to be negligible as the thin layer of cells is embedded in a relatively much bulkier ionic medium. However, it has been demonstrated that in tissues, where cells are densely packed, the conductivity changes caused by electroporation can have a substantial impact on the electric field distribution and hence on the TV [99]. Therefore, for thoroughly studying treatment overlap, it would be judicious to analyze the impact on field distribution that preceding treatments can have on subsequent

treatments due to conductivity changes caused by electroporation. (Sophisticated mathematical constructs have been proposed to model such effect [80, 141, 227, 255–258].) Nevertheless, it must be taken into account that whereas conductivity changes within each pulse (in-pulse conductivity) can be very high (and that is why they can have a significant impact on the field distribution), this in-pulse conductivity is only slightly influenced by the preceding pulses or sequences of pulses [39]. In the preliminary 3D simulations (Table 4.8 where we coarsely approximated this effect considering worst-case assumptions, we found minimal consequences ($<$1.36 % difference). Therefore, we conclude that the impact of conductivity changes does not modify the qualitative conclusions reached here.

4.5 Conclusions

Treatment overlap is present in almost every electroporation procedure but, to the best of our knowledge, its impact had not yet been quantified. We found that, as expected, overlapping treatments can substantially reduce the electric field threshold needed to induce cell death and thus increase the efficacy of the overall treatment. However, in terms of TV, we deduce that the impact of overlapping treatments will be minor in typical NTIRE procedures in which trains of 70 or more pulses are applied through multiple electrode pairs. Importantly, the overall ablation volume will be predicted with a reasonable level of accuracy by simply performing the geometric union of the ablation volumes predicted for each electrode pair. Although this study did not evaluate treatment overlap in vivo, we presume that the method used in most NTIRE pre-clinical and clinical studies is adequate. We also confirmed that the model proposed by Garcia *et al*. [113] is valid for predicting treatment overlap, as well as the adapted logistic model introduced here. At last, even if this study does not explicitly contemplate ECT, it can be inferred that the same general conclusions apply to treatment overlap in ECT procedures.

Chapter 5

A PLATFORM FOR TREATMENT PLANNING IN ELECTROPORATION-BASED THERAPIES

Adapted from:
Perera-Bel E, Aycock KN, Salameh ZS, Davalos RV, Ivorra A, González Ballester MA. A platfrom for patient-specific treatment planning in electroporation-based therapies. [In preparation]

5.1 Introduction

Treatment planning in solid tumor therapies consists of modeling the treatment volume (TV) preoperatively to ensure full tumor eradication while preserving surrounding vital structures. Specifically, in electroporation-based therapies, treatment planning consists of simulating the electric field distribution that will be applied to the target tissues by means of electrode pairs. Given a pulsing protocol, the TV is the region whose electric field magnitude is above a threshold.

The electric field distribution is highly dependent on treatment parameters. Namely, the number of electrodes, their position, and the voltage applied between pairs of electrodes. The electrodes are typically inserted in parallel, evenly spaced, and at the same depth. However, anatomical constraints are present in the treatment of deep seated tumors which forbid this strict parallel configuration [225]. For example, percutaneous treatment of liver tumors must avoid electrode insertion through bone and vital vessels.

Another factor which strongly influences the electric field distribution is tissue electrical conductivity [93]. Because of the increased membrane permeability induced by electroporation, ions can flow through electroporated cells, which at a macroscopic scale translates as an increase in electrical conductivity. This behavior is tissue-specific, and it is typically modeled as a non-linear function which depends on the electric field magnitude [87, 95, 99, 259]. In addition, tissue conductivity is also dependent on temperature, which in physiological tissues is estimated to rise around 2 % every degree Celsius [101].

Therefore, preoperatively predicting the treatment volume in electroporation-based therapies is a complex process. First, a heterogeneous model which represents tissue geometry and electrical properties is required. Second, planning involves the evaluation of different

configurations of position, angle, depth and number of electrodes, to decide on the final plan for the intervention.

Current treatment plans are typically performed using medical imaging software to extract the anatomical structures from patient medical images, which are then imported to general purpose finite elements method (FEM) where the electrodes are inserted and the electric field is simulated [60, 225]. These tools are versatile and accurate models can be built, but they require of significant expertise in physics and numerical modeling. In addition, modeling patient-specific heterogeneous tissues is complex as fine anatomy details must be preserved. From a clinical point of view, these systems are impractical: clinicians can rarely dedicate the required several hours, neither have the technical knowledge necessary to manipulate such complex tools.

Although there are some dedicated tools for electroporation modeling [226, 227, 246], to the best of our knowledge, there is only one dedicated system for treatment planning of electroporation procedures, VISIFIELD [24, 228]. It is a web platform for patient-specific treatment planning with an easy workflow for non-technical users such as clinicians. It provides manual and automatic segmentation tools and includes typical electrode arrays. The electric field distribution is simulated in the cloud and a treatment plan summary can be downloaded after a satisfactory simulation. Nonetheless, since its publication, recent studies have shown the importance of modeling considerations which were not deemed significant at the time. For example, the electrodes cannot be positioned in a non-parallel fashion, nor inserted at different depths. This can be an issue for planning the incision of percutaneous deep seated tumors where critical structures force electrodes insertion at different angles. Failing to model the electric field in the same conditions that will be met during the intervention will probably lead to treatment failure. Moreover, it does not model the dependence of the electrical conductivity on the temperature. As it has been reported in some numerical studies, the temperature increase can have a marked impact in the overall treatment

volume, mostly in IRE procedures due to the high number of applied pulses [103, 116].

Here, we present PIRET, a Platfom for Irreversible and Reversible Electoporation Therapies, focused on the treatment of solid tumors. An advanced visualization of medical images and 3D reconstruction of tissues is provided to help in tissue segmentation, electrode insertion, and treatment volume assessment. An easy-to-use and fast workflow has been designed to, hopefully, allow clinicians and other non-technical users generate treatment plans in clinical practice. Importantly, the treatment volume is simulated using novel methodologies which not only consider electrical conductivity non-linearities due to the electroporation phenomenon, but also due to thermal effects. A detailed description of the platform is reported including the user workflow, the technological stack, the implementation of the modeling method, and the user workflow. A pilot validation study is reported where this platform was used to successfully retrospectively model the treatment volume of three canine liver tumors.

5.2 Materials and methods

5.2.1 Platform design

Treatment planning workflow

PIRET has been developed to generate patient-specific treatment plans in electroporation-based therapies. An easy-to-use workflow with few steps is provided to facilitate clinicians and non-technical users perform the treatment plan, which is divided in four steps: image segmentation, treatment setup preparation, modeling of the electric field, and assessment of the treatment plan (Fig. 5.1). Namely, image segmentation is required

to extract the anatomical geometry of the patient to which the electrodes are virtually inserted. A 3D heterogeneous model is built and the electric field distribution is simulated according to the applied voltage between pairs of electrodes. Finally, the predicted TV can be evaluated.

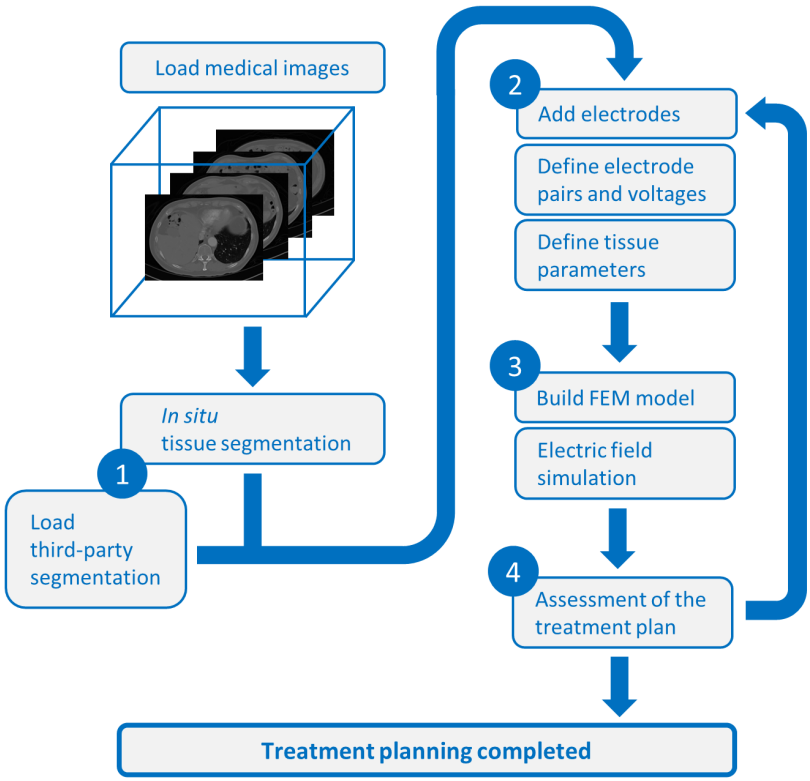

Figure 5.1: Workflow diagram of the platform. The steps are: 1) segmentation of the target tissues, 2) definition of the treatment setup, 3) numerical modeling of the electric field distribution, and 4) assessment of the plan.

Step 1 — Image segmentation

In order to build a patient-specific model, the target tissues must be identified, that is, the tissues must be segmented from the medical images. Typically, the tumor and the surrounding healthy organ are required, but

other nearby organs and blood vessels should also be included [225]. Manual, semi-automatic and automatic segmentation tools are included in the platform.

Step 2 — Treatment setup

The plan continues by setting up the treatment parameters, that is, the arrangement of electrodes, the voltage applied between pairs, and the properties of the modeled tissues. First, up to 7 monopolar or bipolar needle-shaped electrodes can be inserted into the target volume in one of the predefined arrays (Fig. 5.2). The distance between the electrodes in the arrays can be adjusted, as well as the needle diameter and electrode exposure. Individual electrodes can be manually displaced from the predefined configuration.

The electrode pairs are already defined for the predefined arrays (Fig. 5.2), and the voltage between pairs is automatically set according to a user-defined voltage to distance ratio. More electrode pairs can be added or removed, and the voltage can be individually modified for each pair.

To finish the treatment setup, tissue properties must be assigned to the different segmentations included in the model.

Step 3 — Electric field modeling

A patient-specific model is built from the selected segmentation images and the virtually inserted electrodes. The electric field is simulated for all the defined pairs and the overall contribution is obtained by combining the maximum computed electric field magnitude from the individual simulated pairs. The whole process is fully automatic.

There are two simulation methodologies. The fastest method considers the dependence of tissue electrical conductivity on the electric field. Alternatively, the thermal distribution can be also computed to model the conductivity dependence on the temperature and to assess thermal

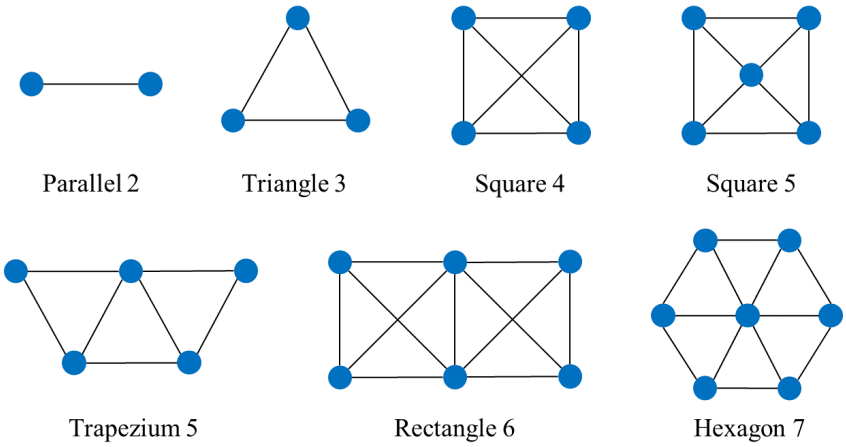

Figure 5.2: Schematic illustration of the predefined electrode arrays. The naming conventions is "Pattern X", where the first word indicates the relative arrangement and X is the number of electrodes. All the electrodes are evenly spaced. The lines connecting the electrodes indicate the default pairs.

damage, but it is considerably slower. In the case if IRE, the latter should be preferred because the high number of applied pulses generate considerable heat [7, 103], although an initial estimation can be obtained with the former.

Step 4 — Assessment of the predicted treatment volume

In radiotherapy treatment planning, there is a nomenclature to distinguish between the tumor that is visible in the medical images and the volume which must be treated to ensure treatment efficacy [27]. Although this classification has not been previously used for electroporation planning, the concept also applies. First, the visible tumor in medical images is referred as the gross tumor volume (GTV). However, tumors present microscopic infiltration that remain unseen in the images and a margin is added, which is known as clinical target volume (CTV). Further uncertainties arise due to differences in patient position between the

imaging and the treatment, breathing, and physiological movements of internal organs. In the case of electroporation, numerical inaccuracies due to tissue conductivity variability should also be accounted for. For these reasons, a margin is added to the CTV, known as the planning target volume (PTV) [149, 179, 180]. Therefore, treatment planning consists of finding the right parameters which successfully treat the PTV while preserving nearby critical structures.

The TV can be initially visually assessed as the electric field is overlayed on top of the medical images. In addition, treatment efficacy can be quantified with the provided tools that display the degree of coverage of the PTV and the volume of treated healthy tissue. If the plan is unsatisfactory, either by an insufficient volume fraction or by an over-treatment of non-pathological tissue, the electric field can be recomputed by fine-tuning treatment parameters in step 2.

A summary of the electrode pairs, the applied voltage and the simulated electric current is also presented. Because electroporation generators are limited to an electric current of 50 A, pairs which predict a higher current should be avoided. Either lowering the voltage, placing the electrodes closer together, or reducing the exposure, will reduce the required electric current.

Graphical user interface

The platform has been designed to have an intuitive and clear interface for non-technical users (Fig. 5.3). Its main feature is a medical image viewer so users can easily visualize the anatomy and the pathological tissues. This viewer is composed of the three orthogonal planes, axial, sagittal, and coronal, and a 3D render window. To facilitate the visualization of the tissues, image contrast can be adjusted. Some of the accepted image formats are Digital Imaging and Communications in Medicine

(DICOM), Neuroimaging Informatics Technology Initiative (NIfTI), and Nearly Raw Raster Data (Nrrd). Accepted formats for surface meshes are VTK PolyData (VTK, VTP) and Stereolithography (STL).

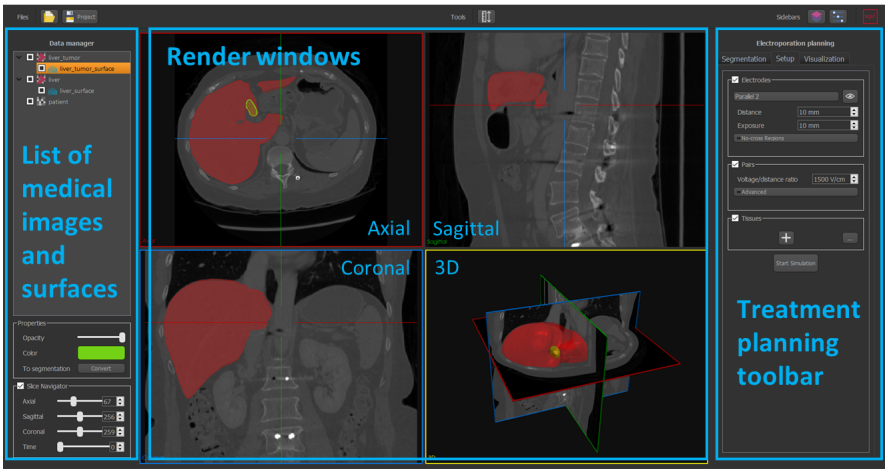

Figure 5.3: Overview of the platform. It is divided in three main components. On the middle there is the image and surface meshes viewer, with axial, sagittal, and coronal 2D views, and a 3D render window. On the left, there is the "Data manager", with a list of the loaded images and surface meshes, and some tools to edit them and navigate through the slices. On the right, there is the "Electroporation planning" toolbox for treatment planning. Medical image and surface meshes obtained from 3D-IRCADb-01 database from IRCAD, France.

Each of the steps that require user interaction to generate the treatment plan has its own controls which are found in the *Electroporation planning* toolbar, on the right of the viewer. First, there is the *Segmentation* toolbox (Fig. 5.4.a). Although third party segmentation images and surface meshes can be loaded, the platform provides general automatic and semi-automatic segmentation tools. Alternatively, manual segmentation is also possible on 2D slices. For these cases, an interpolation tool, based on the radial basis function interpolation [260] and Laplacian smoothing [261], is provided to generate a 3D volumes from sparsely segmented 2D slices.

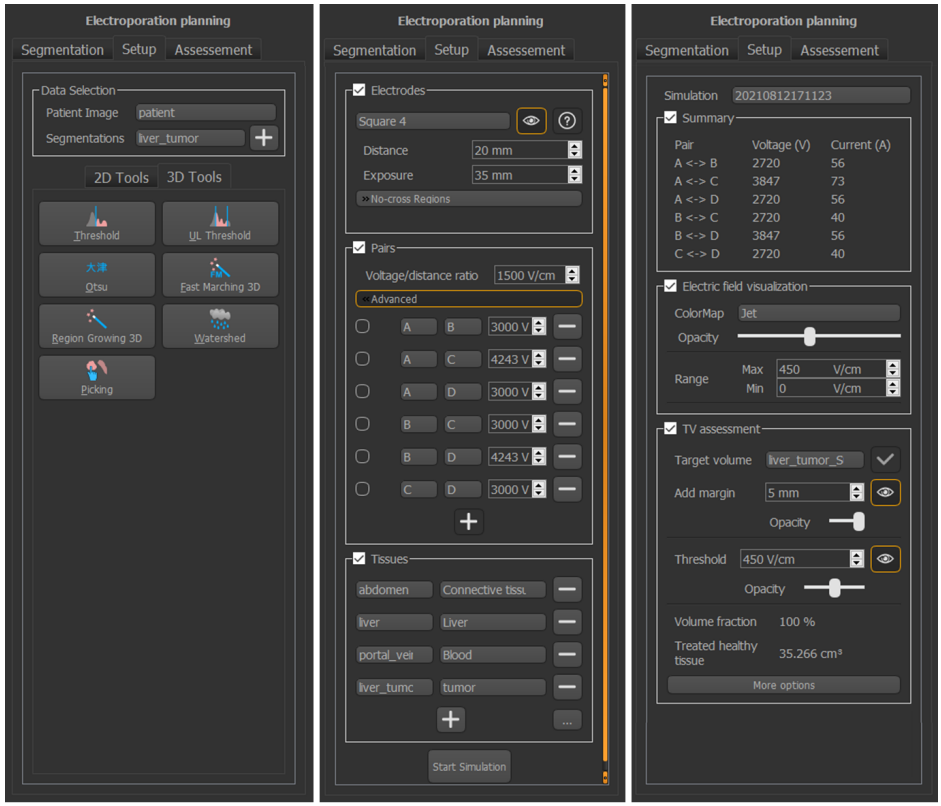

(a) (b) (c)

Figure 5.4: Toolboxes for treatment planning. (a) Segmentation, (b) Setup, and (c) Assessment

The electrodes are inserted using the *Setup* toolbox (Fig. 5.4.b). Monopolar and bipolar needle electrodes are available in 7 different predefined arrays (Fig. 5.2), with the selected diameter and length of exposure. In the case of bipolar electrodes, the length of both exposed parts and the insulator in between can be set independently. Although the electrodes in the array are uniformly distributed with a user-defined separation, individual electrodes can be manually displaced. Additionally, it is possible to define some regions which cannot be

crossed by the electrodes, such as bone or critical vessels. The selected segmentations are converted into surface meshes which are used to find intersection points with the electrodes. In case of collision, electrodes are highlighted in red.

The *Setup* toolbox is also used to define the voltage across electrode pairs and to assign tissue properties to the different segmentations included in the model. Predefined tissues are available with both electrical and thermal properties.

Finally, the tools for assessing the electric field and determining the treatment volume are included in the *Assessement* toolbox (Fig. 5.4.c). Although the treatment volume can be visually analyzed as the electric field is overlayed on top of the medical images, we provide tools to quantify treatment efficacy. That is, by comparing the predicted TV with the PTV.

The TV is obtained by setting the electric field threshold of the corresponding tumor tissue. The PTV is derived by expanding the segmentation of the GTV a few millimeters (user-defined) in all directions to account for planning uncertainties. The portion of PTV that is covered by the TV (volume fraction, VF) is computed, as well as the portion of treated healthy tissue (THV).

$$\mathrm{VF} = \frac{\mathrm{TV} \cap \mathrm{PTV}}{\mathrm{PTV}} \tag{5.1}$$

$$\mathrm{THV} = (\mathrm{TV} \cup \mathrm{PTV}) - \mathrm{TV} \tag{5.2}$$

The volume fraction must be 100 % for treatmente efficacy, while the THV should be minimized.

5.2.2 Implementation

Technological stack

The platform has been developed in C++ using proven open-access libraries. It is based on The Medical Imaging Interaction Toolkit (MITK)[1] [208, 262], which is a library for medical imaging processing and visualization. Specifically, MITK includes The Insight Toolkit (ITK)[2] [263,264] for image processing, The Visualization Toolkit (VTK)[3] [233] for image and volume processing and visualization, and Qt[4] for the graphical user interface (GUI). The Computational Geometry Algorithms Library (CGAL)[5] [234, 235] is used to generate the FEM model, and Elmer[6], a mulitphysics FEM solver, is in charge of the electric field simulation.

Simulation of the electric field distribution

A 3D FEM mesh is built from the segmented tissues to accurately represent patient anatomy. The electrodes are then included according to the specified coordinates and insertion angle. The mesh is built with tetrahedron elements following an adaptive criteria with smaller elements around the electrodes and coarser ones farther away. Finer elements are also placed in the boundaries between two tissues to preserve the anatomical details. For further details see our previous work in section 3.2.2.

[1] MITK: https://www.mitk.org
[2] ITK: https://www.itk.org
[3] VTK: https://www.vtk.org
[4] Qt: https://www.qt.io
[5] CGAL: https://www.cgal.org
[6] Elmer: https://www.csc.fi/ web/elmer

The electric field distribution is simulated using FEM by solving the Laplace equation for electric currents with charge conservation:

$$\nabla \cdot \sigma \nabla \phi = 0 \tag{5.3}$$

$$\vec{E} = -\nabla \phi \tag{5.4}$$

where ϕ is the electric potential, σ is the electrical conductivity, and $\vec{E}$ is the electric field [102].

It is known that during electroporation, the electrical conductivity rises due to the increased membrane permeability, an effect typically modeled as a dependency on the electric field magnitude [60, 96, 97, 99, 265]. Here, we implement the symmetric sigmoid function introduced by Šel *et al.* [87]:

$$\sigma(E) = \sigma_0 + \frac{\sigma_{max} - \sigma_0}{1 + A \exp\left(-\frac{|E|-B}{C}\right)} \tag{5.5}$$

where $\sigma(E)$ is the electrical conductivity which depends on the electric field E, σ_0 is the static conductivity, and σ_{max} is the maximum conductivity that is reached when the whole tissue is electroporated.

Because of the strong-non-linear relationship between conductivity and electric field, a relaxed iterative solver is used to ensure convergence.

$$\phi_k^* = \gamma \phi_k + (1 - \gamma)\, \phi_{k-1} \tag{5.6}$$

where γ is the relaxation factor and ϕ_k^* is the new approximation of the electric potential, given the current ϕ_k and the previous ϕ_{k-1} potentials. Convergence is reached when the L^2-norm of change of both the electric potential and the electric field are smaller than 10^{-5}. A strong non-linear case ($C = 50\,\mathrm{V/cm}$) was used to determine the relaxation factor as a function of the rise in electrical conductivity:

$$\begin{aligned} \sigma_{max}/\sigma_0 = 1 &\rightarrow \gamma = 1 \\ 1 < \sigma_{max}/\sigma_0 \leq 2 &\rightarrow \gamma = 0.65 \\ 2 < \sigma_{max}/\sigma_0 \leq 3 &\rightarrow \gamma = 0.45 \\ 3 < \sigma_{max}/\sigma_0 &\rightarrow \gamma = 0.3 \end{aligned} \tag{5.7}$$

The relaxation factor is determined by the modeled tissue with the highest σ_{max}/σ_0 ratio. Notice that a ratio above 3 or sharper transitions than $C < 50$ V/cm are not expected in most biological tissues. Thus, σ_{max}/σ_0 and C are limited to 5 and 50 V/cm, respectively.

Dirichlet boundary conditions are applied to the two active electrodes, setting one electrode to the applied voltage and grounding the other one (i.e., 0 V). When more than one electrode pairs are included, an individual simulation is computed for each pair. For multi-core CPUs, the different pairs are simulated in parallel. The overall electric field distribution is obtained by combining the maximum computed field from all individual simulated pairs.

Simulation of the temperature distribution

During the application of the electric pulses, high electric currents are induced which can significantly rise the temperature due to Joule heating. This effect is most prominent in IRE because a high number of pulses (> 70) are applied. This can have two effects on electroporation treatment planning. First, thermal damage can be assessed, as it is not uncommon to find thermally coagulated tissue around the electrodes [100]. Second, the dependence of the electrical conductivity on temperature can be modeled [103, 116]. It is estimated that electrical conductivity rises 2 % every degree Celsius in physiological tissues [101]. Such dependence can be modeled with this platform, although computation time is highly penalized because the temperature is time dependent, compared to the solution of the electric field alone which is stationary.

The Joule heating is derived from the electric potential with:

$$Q_J = \nabla\phi \cdot \sigma\nabla\phi \tag{5.8}$$

Because the electric field is only generated during the application of the pulse, the heat is scaled according to the duty cycle of the pulse

(pulse duration times pulse repetition frequency) to speed up the time-stepping solution [95]. The temperature distribution T is then obtained by solving the Penne's bioheat equation, which is the thermal model that best describes heat transfer in biological tissues [117]:

$$\rho c_p \frac{\partial T}{\partial t} = \nabla \cdot (k \nabla T) - \rho_B \omega_B c_B (T - T_B) + Q_M + Q_J \tag{5.9}$$

where ρ, c_p, and k are the tissue density, heat capacity and thermal conductivity, respectively. Tissue perfusion is determined by blood perfusion rate ω_B, blood density ρ_B, blood heat capacity c_B, and blood temperature $T_B = 37°C$. Q_M is the metabolic heat generation, but for electroporation modeling it can be neglected due to its minimal contribution to temperature rise [266].

The overall conductivity which models the dependence on the electric field and the temperature is given by:

$$\sigma(E,T) = \left(\sigma_0 + \frac{\sigma_{max} - \sigma_0}{1 + A \exp\left(-\frac{|E|-B}{C}\right)} \right) \cdot (1 + \alpha(T - T_{ref})) \tag{5.10}$$

where α is the temperature coefficient (2 %/°C) and T_{ref} is the reference temperature (37 °C).

5.3 Results

5.3.1 Platform features

With this platform, we combined all the required tools to perform treatment planning in electroporation based therapies. There are other platforms that can be used as well to model the electroporation volume, but compared to PIRET they either lack features to perform the whole

treatment planning process, or they do not consider novel modeling methodologies that have been proved to have a marked impact. In Table 5.1 we compare the features of such tools, including the web platform EView described in chapter 3, and PIRET.

		FEM software	ApiVizTEP [226]	EView [246]	OpenEP [227]	Visifield [97]	PIRET
Model	3D	Yes	No	Yes	Yes	Yes	Yes
	Multiple tissues	Yes	No	No	No	Yes	Yes
	Patient specific	*	No	No	No	Yes	Yes
	$\sigma(E)$	Yes	No	Yes	Yes	Yes	Yes
	$\sigma(E,T)$	Yes	No	No	Yes	No	Yes
Electrode	Predefined arrays	No	Yes	No	Yes	Yes	Yes
	Individual positioning	Yes	No	Yes	No	No	Yes
Workflow		Complex	Simple	Simple	Simple	Simple	Simple
Open source		Yes/No	Yes	Yes	Yes	Yes	Yes

* Models must be created with third-party software

Table 5.1: Comparison of software for modeling the electroporation volume and/or perform treatment planning.

5.3.2 Pilot study

Data acquisition

We used this platform to retrospectively model the electric field distribution to predict the treatment volume in three canine patients with hepatocellular carcinoma (HCC). The treatments are described in detail in Partridge *et al.* [267].

Three client-owned canines were recruited and treated at the Virginia-Maryland College of Veterinary Medicine Teaching Hospital, VA, USA, from January to March 2018. Canine 1 was a 15-year-old male toy poddle, canine 2 was a 13-year old mixed-breed female, and canine 3 was a 14-year-old male toy poddle. The goal of that study was to determine H-FIRE safety and feasibility, so a treat-and-resect procedure was established to minimize risks. Thus, the H-FIRE procedure was planned to only treat a small volume of malignant tissue, as the whole tumor was excised four days after. 300 biphasic bursts were delivered at an amplitude of 2250 V through a single 16-gauge bipolar electrode (AngioDynamics, Latham, New York) inserted percutaneously. The bursts consisted of a 2 µs pulse, followed by a 5 µs pause, and another 2 µs pulse of reversed polarity (on-off-on, 2-5-2 pulse). The waveform was repeated for a total *on* duration of 100 µs.

Canine model

Data consisted of pre-treatment and four-day post-treatment CT scans. Pre-treatment images were used to build the patient-specific models which included tumor, liver, vasculature, and adipose tissue. Liver and tumor segmentation were obtained semi-automatically by interpolating a few manually segmented slices using the provided radial basis interpolation function. Major vessels were included, such as the hepatic vein and the main branches, as well as small arteries near the treatment volume, which were segmented using region growing algorithm from manually placed seed points. Adipose tissue adjacent to liver and tumor surface was segmented with thresholding. The images and the segmentations are illustrated in Fig. 5.5.

In the work of Partridge *et al.*, the electrical conductivity of the treated tissue (i.e., tumor) was approximated by adapting the model of O'Brien *et al.* [268] with intra-procedural readings of the electric current. For the liver, we used the same model but modified the baseline conductivity σ_0 to

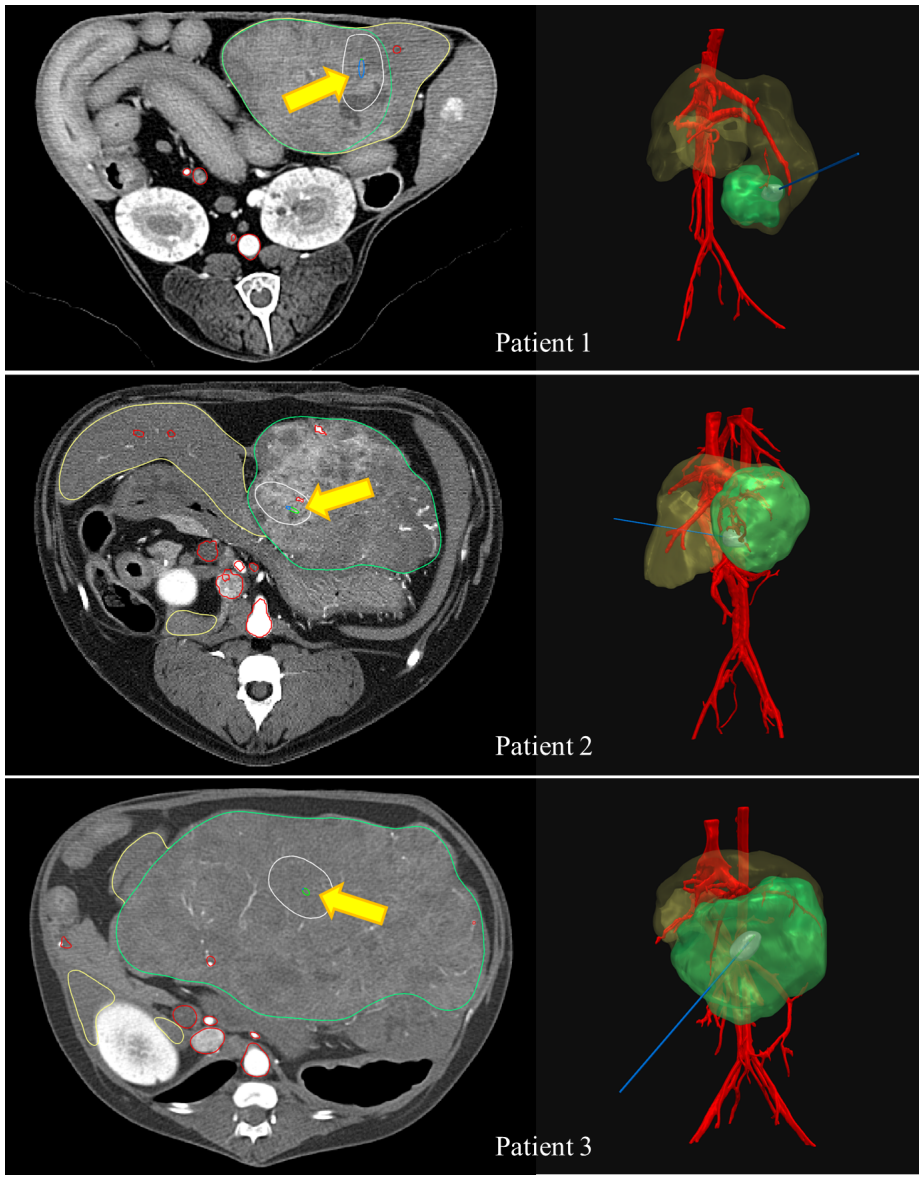

Figure 5.5: Left column: pre-treatment image with the segmentation of liver (yellow), tumor (green), and vessels (red) for the three patients. The region that was treated is delimited by the white contour, and the yellow arrow indicates the electrode. Right: 3D reconstruction of the tissues.

0.143 S/m to coincide with measurements from healthy canine liver [269]. This value seems reasonable since it is known that tumor conductivity tends to be higher than that of healthy liver (tumor baseline conductivity is 0.221 S/m) [270]. Such curves are described by a smoothed Heaviside function, but this platform uses the model described in eq. 5.10. Thus, the curves were fitted accordingly ($R^2 = 0.999$).

The electrode insertion angle was approximated from post-treatment CT. A 1.65 mm diameter bipolar electrode was used, with an active length of 7 mm and an insulator separation of 8 mm, with a voltage of 2250 V. Two simulations were computed, considering only the dependence of the electrical conductivity on the electric field ($\sigma(E)$) and additionally modeling its temperature dependence ($\sigma(E,T)$). Tissue electrical and thermal parameters can be found in Table 5.2.

	Unit	Blood	Fat	Liver	Tumor
σ_0	S/m	0.7	0.038	0.143	0.221
σ_{max}	S/m	—	—	0.322	0.497
A	—	—	—	1	1
B	V/cm	—	—	1000	1000
C	V/cm	—	—	163.6	163.6
ρ	kg/m^3	1020	911	1079	1079
c_p	J/kg/K	3617	2348	3540	3540
k	W/m/K	0.52	0.21	0.52	0.52
ρ_B	kg/m^3	1020	—	1020	1020
ω_B	1/s	0.17	—	7.15×10^{-3}	7.15×10^{-3}
c_B	J/kg/K	3617	—	3617	3617

Table 5.2: Electrical and thermal tissue properties. Blood and fat conductivity, as well as the thermal properties for all tissues were obtained from [116, 271, 272].

5.3.3 Evaluation of the predicted treatment volume

Figure 5.5 illustrates the segmented tissue geometry and the patient-specific model used to simulate the electric field distribution for patient 1. It also displays the predicted treatment volume and the segmented lesion.

The predicted TV was compared against the segmented lesion volume from post-treatment imaging by computing the Dice score and volume similarity (VS) coefficient:

$$\text{Dice} = \frac{2|X \cap Y|}{|X| + |Y|} \tag{5.11}$$

$$\text{VS} = \frac{|X - Y|}{|X| + |Y|} \tag{5.12}$$

where X and Y are the two compared volumes. Whereas VS only compares the absolute volume, the Dice score also measures the degree of overlap between the two samples. The two metrics are complementary and provide a good comprehension of the similarity between the lesion and the predicted volume.

Fig. 5.7 illustrates the metrics at different electric field magnitudes. For the $\sigma(E)$ case, the electric field threshold which maximized VS (>0.999) was 633 ± 61 V/cm, whereas the highest Dice score (0.845 ± 0.013) was found at a lower threshold of 609 ± 75 V/cm. Higher thresholds were found with the $\sigma(E, T)$ model. A maximum VS was found at an electric field of 704 ± 52 V/cm, and the largest Dice score of 0.869 ± 0.009 was found at 685 ± 61 V/cm. Similar electric field thresholds (710 ± 28 V/cm) were found by Partridge *et al.* [267]. Table 5.3 shows the electric field thresholds that maximized the similarity metrics for all three patients.

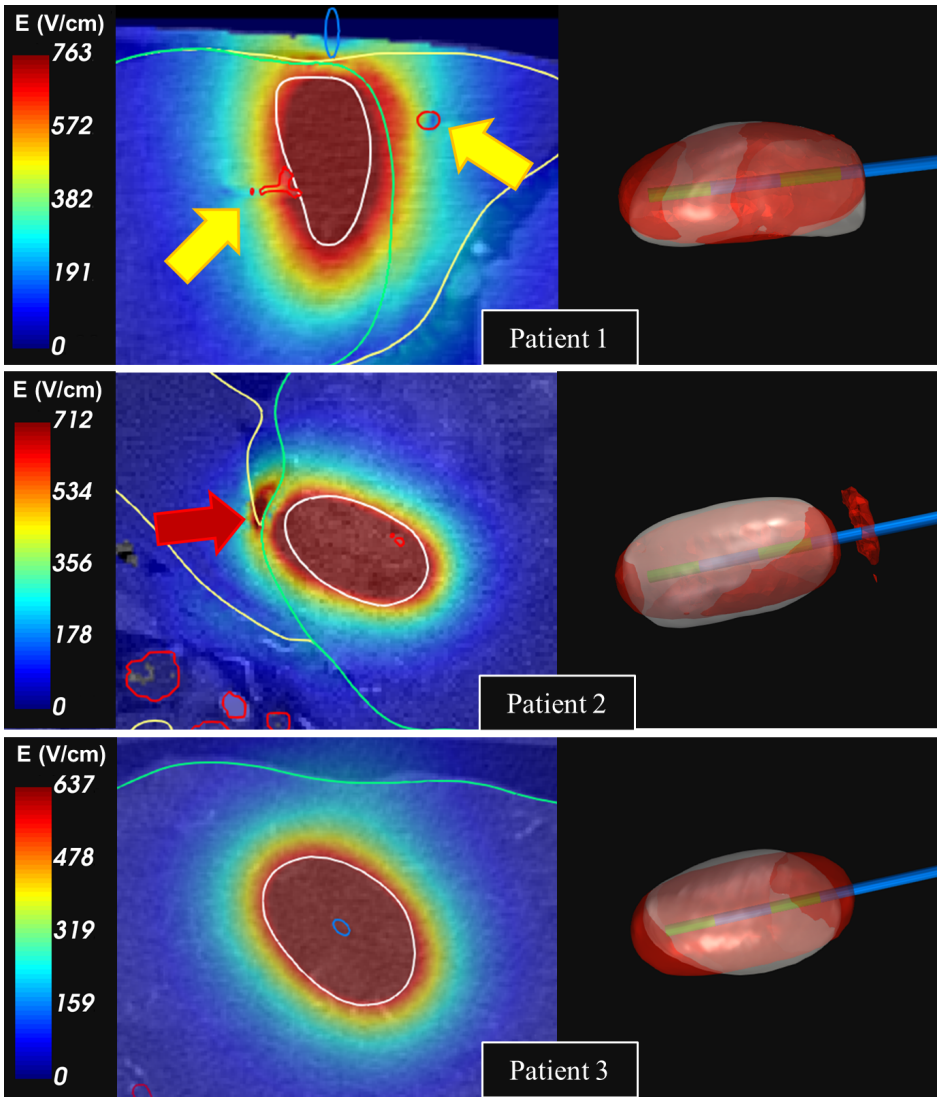

Figure 5.6: Left: simulation of the electric field distribution overlayed on top of the medical images for the three patients. The displayed contours are the same as in Fig. 5.5. Right: 3D representation of the electric field threshold (red) which best fitted the lesion (white). The yellow arrows indicate electric field inhomogeneities due to high conductivity of vessels, and the red arrow due to the low conductivity of fat.

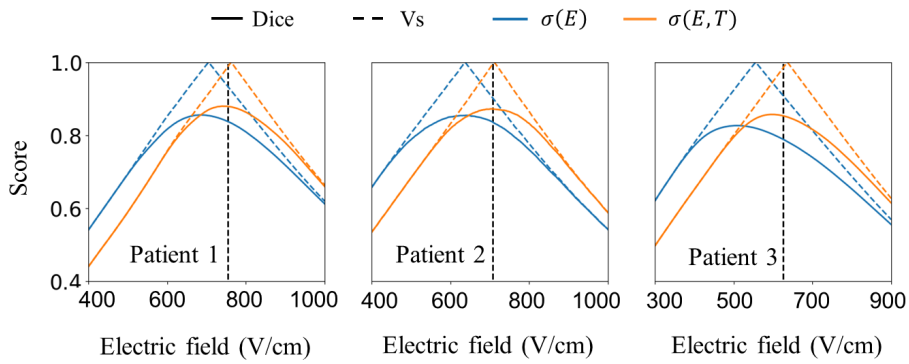

Figure 5.7: Similarity metrics between the predicted treatment volume and the lesion from the post-treatment image for the three patients. The continuous line shows the Dice score, and the dashed line represents VS. The scores are displayed for the two models: blue is $\sigma(E)$ and orange is $\sigma(E,T)$. The black vertical dashed line illustrates the electric field threshold found in [267].

	$\sigma(E)$		$\sigma(E,T)$		[267]
	Dice	VS	Dice	VS	
Patient 1	687	706	748	763	755
Patient 2	632	638	702	712	707
Patient 3	508	556	602	637	626

Table 5.3: Electric field thresholds (V/cm) that maximize the similarity metrics. The right column shows the thresholds found by Partridge *et al.*

5.4 Discussion

According to the obtained results on the three canine patients, and as expected, this platform can be used to accurately predict the electric field distribution and, thus, the treatment volume in electroporation-based therapies. Importantly, this platform reduces the complexity to perform treatment planning, as all the essential tools have been optimized and integrated for a simple interaction that can be used by non-technical users.

To the best of our knowledge, PIRET is the most complete platform for electroporation-based therapies treatment planning, as reported in Table 5.1.

5.4.1 Model accuracy

The obtained electric field thresholds in this study (704 ± 52 V/cm) are in line with the findings from Partridge *et al.* (710 ± 28 V/cm), which used a temperature dependent model similar to the one described here and solved in COMSOL Multiphysics, a general purpose FEM software. These small differences arise mainly from variations in the mesh building process and in numerical convergence criteria. Although in this pilot study we additionally modeled healthy liver tissue, vessels and adipose tissue, the influence on the overall volume is minimal. Nonetheless, the different tissues can substantially modify the electric field locally. This effect is clearly illustrated in Fig. 5.6 (patient 1, yellow arrows) where small vessels are near the outer boundary of the lesion and the electric field in its vicinity is much lower. Although small vessels do not seem to affect the treatment volume, larger ones can compromise treatment efficacy [273]. Instead, the electric field tends to "escape" to tissues with a lower electrical conductivity such as bone, fat or skin (Fig. 5.5, patient 2, red arrow).

Another important consideration that must be addressed during modeling is if the temperature distribution should also be simulated. In the three canine cases studied here, the two modeling methods (with $\sigma(E)$ and $\sigma(E,T)$) showed a significant difference of 10.1 % in the electric fields threshold that better described the lesion (p-value = 0.01, two-tailed paired t-test). Some numerical studies already observed that heat generation can enlarge the predicted electroporation volume, mainly in therapies where a high number of pulses are applied [103, 116]. Therefore, for NTIRE or H-FIRE, the time dependent model with $\sigma(E,T)$ should be preferred. Instead, in procedures such as ECT, the temperature

increase is minimal due to the application of less pulses with lower electric fields, and the simpler model will provide equally accurate results with significant time savings ($\times$15-20). Nevertheless, simulating the temperature distribution is also useful for evaluating thermal damage as it is not uncommon to find thermally ablated tissue around the electrodes [7, 95, 100, 274]. A good approach consists of initially computing the electric field with the non-thermal model to rapidly approximate the TV, and later simulating the temperature effects to fine-tune the planning.

The importance of using the appropriate model is clearly observed with overlap metrics. In the simulated canine models, we found a higher Dice score with the thermal model (0.869 vs 0.845), which means that the intersection between the predicted volume and the lesion was higher. In other words, the model that considered the electrical conductivity dependence on the temperature was more accurate. It is important to point out that VS alone cannot tell which model is better, as only the overall volumes are considered, regardless of the relative position and shape.

This can have some implications in studies which characterize the electric field threshold by comparing the volumes from experimental data and numerical simulations [79, 198, 199, 238]. Although we observed non-significant differences in the electric field threshold predicted by either metric (a difference of 10 to 35 V/cm, p-value > 0.12, two-tailed paired t-test), we believe that overlap metrics can provide a slightly better approximation of the electric field threshold as not only the overall volume is contemplated, but also their intersection.

5.4.2 Limitations and lines of improvement

The pilot retrospective study served to validate the accuracy of the modeling methodology by correlating the electric field distribution with the lesion. However, the electrode insertion was inferred from post-

treatment imaging and it was positioned in alignment with the lesion, which likely contributed to a good matching between the lesion and the predicted TV. Ideally, to properly assess the treatment planning capabilities of the platform, the electrode insertion should have been planned blindly, that is, without any prior knowledge of the lesion location, size or shape. Therefore, this platform should be tested on real cases to fully validate its accuracy in predicting the treatment volume.

In addition, physician feedback is needed to fine-tune the application, as it aims to be used in clinical practice. Nonetheless, we are confident that the proposed workflow is useful in clinical environments to predict the treatment volume in an easy-to-use way. And, although the study has been mostly focused around the treatment of solid tumors with IRE, PIRET can potentially be used for other electroporation-based therapies such as EGT and PFA when needle-shaped electrodes are used.

5.5 Conclusions

A platform for patient-specific treatment planning in electroporation-based therapies has been developed. Importantly, a simple workflow has been implemented which allows non-technical users plan electroporation procedures in a much simpler and faster way than previously available. A 3D model from patient medical images can be easily built to predict the treatment volume by simulating the electric field distribution. With this platform, we successfully retrospectively modeled three canine liver tumors. The predicted treatment volume accurately correlated to the lesion volume observed in post-treatment images, and the inferred IRE thresholds were in line with the findings of the original work by Partridge *et al.* [267].

Although this study only contemplated canine liver tumors treated with H-FIRE, the platform has been designed to be versatile. That is,

to treat solid tumors with ECT or NTIRE in any animal or human tissue. Additionally, it can potentially be used for other electroporation-based therapies such as EGT and PFA. Future work will further validate the platform with more retrospective cases, and, importantly, with *in situ* treatment planning. Workflow and interface will be improved from clinician feedback. Additional research should focus on coupling treatment planning with image guided interventions and surgical navigation. Hopefully, this platform will help to introduce electroporation-based therapies as standard clinical procedures.

Chapter 6

CONCLUSIONS

Computational tools for electroporation modeling and treatment planning in electroporation-based therapies have been developed in this thesis. Specifically, for the treatment of solid tumors with irreversible electroporation. The contributions are:

• The development of a web-platform which illustrates electroporation dependence on electrode number and positioning, the voltage applied between electrode pairs, and the tissue electrical conductivity.

• The characterization and modeling of cell death due to treatment overlap in irreversible electroporation therapies.

• The development of a patient-specific treatment planning platform for electroporation-based therapies which has a simple workflow that allows clinicians and non-expert users plan electroporation procedures.

6.1 Overview

Chapter 3 presented EView, a web platform which illustrates how treatment parameters affect the electric field distribution in electroporation-based therapies. Namely, the electrode number and positioning, the voltage applied between electrode pairs, and the tissue electrical conductivity. Currently available platforms for simulating the electric field either required much more sophisticated models, both computationally and in terms of the required user expertise, or they provided approximate results based on too simplistic models. Instead, EView provides a simple electroporation simulation workflow which is powerful enough to analyze complex geometries in just a few minutes which can be easily used by students, researchers and clinicians.

Chapter 4 reported an *in vitro* study which aimed at characterizing and modeling cell death in irreversible electroporation therapies due to treatment overlap. The results showed that treatment overlap could substantially reduce the electric field threshold needed to induce cell death and thus increase the efficacy of the overall treatment in certain conditions. However, in terms of overall treatment volume, minimal effects were expected in typical NTIRE procedures in which trains of 70 or more pulses are applied through multiple electrode pairs. It was shown that predicting the treatment volume by simply performing the geometrical union of the ablation volumes of each individual electrode pair was accurate enough, although probabilistic models could be used to also analyze the transition zone. At last, even if this study did not explicitly contemplate ECT, it could be inferred that the same general conclusions applied to treatment overlap in ECT procedures.

At last, chapter 5 described a newly developed treatment planning platform for electroporation-based therapies. The modeling methodology presented in chapter 3 was extended to simulate the electric field distribution on patient-specific models. Although the modeling methodology was more complex, a simple workflow was preserved to

allow clinicians and non-expert users plan electroporation procedures. Three canine liver tumors were retrospectively planned and the predicted treatment volume accurately correlated with post-treatment imaging. Even though this work only contemplated IRE, it could potentially be used for ECT and other electroporation-based therapies such as EGT and PFA. Hopefully, this platform will help in introducing electroporation-based therapies in standard clinical practice.

6.2 Future perspectives

Treatment planning has been of great interest since the beginning of electroporation-based therapies. However, due to its complexity it was mostly found in pre-clincical and clinical studies where the plan is performed by engineers, rather than by clinicians. Future research should focus on further validating the platforms developed in this thesis, and extending their capabilities to ensure more accurate simulations of the electric field and treatment plans.

Research for improving the two platforms developed here should focus on accurately characterizing tissue electrical conductivity, as it highly influences the electric field distribution. Not only conductivity differs between tissue types, but the rise induced due to electroporation is also dependent on the pulsing protocol. That is, the number of pulses, pulse length, and pulse repetition frequency. Therefore, to ensure that the electric field is accurately simulated, conductivity should be further characterized for each tissue and application.

Intraoperative monitoring is key in ensuring that the treatment is being executed as planned. Currently, image-guided interventions are used to assess electrode insertion. However, electrode endpoint deviations from the plan are not uncommon due to organ shifts between the imaging session and the intervention, and an extra safety margin must be added

during planning to ensure treatment efficacy. Therefore, future research should focus on surgical navigation systems that register the treatment plan with the intervention image-guiding system, which, potentially, could reduce the required safety margin.

In Chapter 4, cell death due to treatment overlap was characterized and it was revealed that obtaining the overall treatment volume as the geometric union of the treatment of individual pairs was accurate enough. However, the study was performed *in vitro* on a cell monolayer, so further *in vivo* validation should be performed to prove that the findings are also valid for NTIRE pre-clinical and clinical studies. Additionally, the study only contemplated IRE and it should be investigated if the same overall conclusions apply to RE. Finally, treatment overlap was analyzed in two scenarios with different electric field exposures. Whereas in one case cell membrane was always polarized in the same direction, in the other one polarization was induced at angles close to 90°. Cell death was slightly higher in the latter, probably because a larger membrane area was polarized during the treatments. Understanding this phenomenon is required to fully validate the implications of treatment overlap.

Bibliography

[1] Wild CP, Weiderpass E, et al. World Cancer Report: Cancer Research for Cancer Prevention. vol. 199; 2020.

[2] Howlader N, Noone A, et al. SEER Cancer Statistics Review, 1975-2018. National Cancer Institute; 2021.

[3] Schnipper LE, Davidson NE, et al. American Society of Clinical Oncology Statement: A Conceptual Framework to Assess the Value of Cancer Treatment Options. Journal of Clinical Oncology. 2015 aug;33(23):2563.

[4] Abbott DE, Tzeng CWD, et al. The Cost-Effectiveness of Neoadjuvant Chemoradiation is Superior to a Surgery-First Approach in the Treatment of Pancreatic Head Adenocarcinoma. Annals of Surgical Oncology 2013 20:3. 2013 feb;20(3):500–508.

[5] Ahmed M, Brace CL, et al. Principles of and Advances in Percutaneous Ablation. Radiology. 2011 feb;258(2):351–369.

[6] Kingham TP, Karkar AM, et al. Ablation of Perivascular Hepatic Malignant Tumors with Irreversible Electroporation. Journal of the American College of Surgeons. 2012 sep;215(3):379–387.

[7] Tasu JP, Vesselle G, et al. Irreversible electroporation for locally advanced pancreatic cancer: Where do we stand in 2017? Pancreas. 2017 mar;46(3):283–287.

[8] Nielsen K, Scheffer HJ, et al. Irreversible Electroporation of Liver Tumors. In: Irreversible Electroporation in Clinical Practice. Cham: Springer International Publishing; 2018. p. 139–166.

[9] Li YH, Elshafei A, et al. Salvage focal prostate cryoablation for locally recurrent prostate cancer after radiotherapy: Initial results from the cryo on-line data registry. The Prostate. 2015 jan;75(1):1–7.

[10] Lau WY, Leung TWT, et al. Percutaneous Local Ablative Therapy for Hepatocellular Carcinoma: A Review and Look Into the Future. Annals of Surgery. 2003 feb;237(2):171.

[11] Scheffer HJ. History of Image-Guided Tumor Ablation. In: Irreversible Electroporation in Clinical Practice. Cham: Springer International Publishing; 2018. p. 3–11.

[12] Ren H, Campos-Nanez E, et al. Treatment planning and image guidance for radiofrequency ablation of large tumors. IEEE Journal of Biomedical and Health Informatics. 2014;18(3):920–928.

[13] Ueno S, Sakoda M, et al. Surgical resection versus radiofrequency ablation for small hepatocellular carcinomas within the Milan criteria. Journal of Hepato-Biliary-Pancreatic Surgery. 2009;16(3):359–366.

[14] Nishikawa H, Inuzuka T, et al. Comparison of percutaneous radiofrequency thermal ablation and surgical resection for small hepatocellular carcinoma. BMC Gastroenterology 2011 11:1. 2011 dec;11(1):1–12.

[15] Narayanan G, Froud T, et al. Pain analysis in patients with hepatocellular carcinoma: Irreversible electroporation versus radiofrequency ablation - Initial observations. CardioVascular and Interventional Radiology. 2013 feb;36(1):176–182.

[16] Nielsen K, Scheffer HJ, et al. Anaesthetic management during open and percutaneous irreversible electroporation. BJA: British Journal of Anaesthesia. 2014 dec;113(6):985–992.

[17] Moris D, Machairas N, et al. Systematic Review of Surgical and Percutaneous Irreversible Electroporation in the Treatment of Locally Advanced Pancreatic Cancer. Annals of Surgical Oncology 2019 26:6. 2019 mar;26(6):1657–1668.

[18] Saldanha DF, Khiatani VL, et al. Current Tumor Ablation Technologies: Basic Science and Device Review. Seminars in Interventional Radiology. 2010 aug;27(03):247–254.

[19] Mir LM, Glass L, et al. Effective treatment of cutaneous and subcutaneous malignant tumours by electrochemotherapy. British Journal of Cancer. 1998 jun;77(12):2336–2342.

[20] Davalos RV, Mir LM, et al. Tissue ablation with irreversible electroporation. Annals of Biomedical Engineering. 2005 feb;33(2):223–231.

[21] Rubinsky B. Irreversible Electroporation in Medicine. Technology in Cancer Research Treatment. 2007 aug;6(4):255–259.

[22] Rubinsky B, Onik G, et al. Irreversible Electroporation: A New Ablation Modality – Clinical Implications. Technology in Cancer Research Treatment. 2007 feb;6(1):37–48.

[23] Wimmer T, Srimathveeravalli G, et al. Comparison of simulation-based treatment planning with imaging and pathology outcomes for percutaneous ct-guided irreversible electroporation of the porcine pancreas: A pilot study. Journal of Vascular and Interventional Radiology. 2013 nov;24(11):1709–1718.

[24] Marčan M, Kos B, et al. Effect of Blood Vessel Segmentation on the Outcome of Electroporation-Based Treatments of Liver Tumors. PLOS ONE. 2015 may;10(5):e0125591.

[25] Kos B, Voigt P, et al. Careful treatment planning enables safe ablation of liver tumors adjacent to major blood vessels by percutaneous irreversible electroporation (IRE). Radiology and Oncology. 2015;49(3):234–241.

[26] Wimmer T, Srimathveeravalli G, et al. Planning Irreversible Electroporation in the Porcine Kidney: Are Numerical Simulations Reliable for Predicting Empiric Ablation Outcomes? CardioVascular and Interventional Radiology. 2015 feb;38(1):182–190.

[27] Khan F, Gerbi B. Treatment Planning in Radiation Oncology; 2012.

[28] Beyer LP, Wiggermann P. Treatment Planning, Needle Insertion, Image Guidance, and Endpoint Assessment. In: Irreversible Electroporation in Clinical Practice. Cham: Springer International Publishing; 2018. p. 115–120.

[29] Miklavčič D, Pavšelj N, et al. Electric Properties of Tissues. Wiley Encyclopedia of Biomedical Engineering. 2006 apr;.

[30] Li Kh, Xin Yl, et al. Effects of direct current on dog liver: Possible mechanisms for tumor electrochemical treatment. Bioelectromagnetics. 1997;18(1):2–7.

[31] Yu SP, Canzoniero LMT, et al. Ion homeostasis and apoptosis. Current Opinion in Cell Biology. 2001 aug;13(4):405–411.

[32] Gouaux E, MacKinnon R. Principles of Selective Ion Transport in Channels and Pumps. Science. 2005 dec;310(5753):1461–1465.

[33] Gadsby DC. Ion channels versus ion pumps: the principal difference, in principle. Nature Reviews Molecular Cell Biology 2009 10:5. 2009 apr;10(5):344–352.

[34] Veech RL, Kashiwaya Y, et al. The resting membrane potential of cells are measures of electrical work, not of ionic currents. Integrative Physiological and Behavioral Science 1995 30:4. 1995 sep;30(4):283–307.

[35] Merla C, Pakhomov AG, et al. Frequency spectrum of induced transmembrane potential and permeabilization efficacy of bipolar electric pulses. Biochimica et Biophysica Acta (BBA) - Biomembranes. 2017 jul;1859(7):1282–1290.

[36] Reilly JP. Applied bioelectricity from electrical stimulation to electropathology. Springer Science Business Media; 2012.

[37] Platkiewicz J, Brette R. A threshold equation for action potential initiation. PLoS computational biology. 2010;6(7):e1000850.

[38] Horch KW, Kipke DR. Neuroprosthetics: theory and practice. vol. 8. World Scientific; 2017.

[39] Ivorra A. Tissue Electroporation as a Bioelectric Phenomenon: Basic Concepts. Springer, Berlin, Heidelberg; 2010. p. 23–61.

[40] Weaver JC, Powell KT. Theory of Electroporation. Electroporation and Electrofusion in Cell Biology. 1989;p. 111–126.

[41] Chen C, Smye SW, et al. Membrane electroporation theories: a review. Medical and Biological Engineering and Computing 2006 44:1. 2006 feb;44(1):5–14.

[42] Gissel H, Lee RC, et al. Electroporation and Cellular Physiology. Clinical Aspects of Electroporation. 2011;p. 9–17.

[43] Delemotte L, Tarek M. Molecular Dynamics Simulations of Lipid Membrane Electroporation. The Journal of Membrane Biology 2012 245:9. 2012 may;245(9):531–543.

[44] Kotnik T, Kramar P, et al. Cell membrane electroporation - Part 1: The phenomenon. IEEE Electrical Insulation Magazine. 2012;28(5):14–23.

[45] KINOSITA K, TSONG TY. Formation and resealing of pores of controlled sizes in human erythrocyte membrane. Nature 1977 268:5619. 1977;268(5619):438–441.

[46] Rols MP, Teissié J. Electropermeabilization of mammalian cells. Quantitative analysis of the phenomenon. Biophysical Journal. 1990 nov;58(5):1089–1098.

[47] Rols MP, Teissié J. Experimental evidence for the involvement of the cytoskeleton in mammalian cell electropermeabilization. Biochimica et Biophysica Acta (BBA) - Biomembranes. 1992 oct;1111(1):45–50.

[48] Pucihar G, Kotnik T, et al. Kinetics of Transmembrane Transport of Small Molecules into Electropermeabilized Cells. Biophysical Journal. 2008 sep;95(6):2837–2848.

[49] Saulis G, Lape R, et al. Changes of the solution pH due to exposure by high-voltage electric pulses. Bioelectrochemistry. 2005 sep;67(1):101–108.

[50] Milazzo G, Bombara G. Electrochemistry: Theoretical principles and practical applications. Elsevier,; 1963.

[51] Ivorra A. Electrochemical prevention of needle-tract seeding. Annals of biomedical engineering. 2011;39(7):2080–2089.

[52] Pliquett U. Joule heating during solid tissue electroporation. Medical and Biological Engineering and Computing 2003 41:2. 2003 mar;41(2):215–219.

[53] Jiang Y, Possebon R, et al. A methodology for constraining power in finite element modeling of radiofrequency ablation. International Journal for Numerical Methods in Biomedical Engineering. 2017 jul;33(7):e2834.

[54] Mir LM, Banoun H, et al. Introduction of definite amounts of non-permeant molecules into living cells after electropermeabilization: Direct access to the cytosol. Experimental Cell Research. 1988 mar;175(1):15–25.

[55] Weaver JC, Chizmadzhev YA. Theory of electroporation: A review. Bioelectrochemistry and Bioenergetics. 1996 dec;41(2):135–160.

[56] Rols MP, Teissié J. Electropermeabilization of mammalian cells to macromolecules: Control by pulse duration. Biophysical Journal. 1998 sep;75(3):1415–1423.

[57] Lebar AM, Troiano GC, et al. Inter-pulse interval between rectangular voltage pulses affects electroporation threshold of artificial lipid bilayers. IEEE Transactions on Nanobioscience. 2002;1(3):116–120.

[58] Pucihar G, Krmelj J, et al. Equivalent pulse parameters for electroporation. IEEE Transactions on Biomedical Engineering. 2011 nov;58(11):3279–3288.

[59] Dermol J, Miklavčič D. Mathematical Models Describing Chinese Hamster Ovary Cell Death Due to Electroporation In Vitro. The Journal of Membrane Biology. 2015 oct;248(5):865–881.

[60] Garcia PA, Davalos RV, et al. A numerical investigation of the electric and thermal cell kill distributions in electroporation-based therapies in tissue. PLoS ONE. 2014 aug;9(8):e103083.

[61] Demiryurek Y, Nickaeen M, et al. Transport, resealing, and re-poration dynamics of two-pulse electroporation-mediated molecular delivery. Biochimica et Biophysica Acta (BBA) - Biomembranes. 2015 aug;1848(8):1706–1714.

[62] Teissié J, Ramos C. Correlation between Electric Field Pulse Induced Long-Lived Permeabilization and Fusogenicity in Cell Membranes. Biophysical Journal. 1998 apr;74(4):1889–1898.

[63] Pavlin M, Miklavčič D. Theoretical and experimental analysis of conductivity, ion diffusion and molecular transport during cell electroporation – Relation between short-lived and long-lived pores. Bioelectrochemistry. 2008 nov;74(1):38–46.

[64] Fernández ML, Risk M, et al. Size-controlled nanopores in lipid membranes with stabilizing electric fields. Biochemical and Biophysical Research Communications. 2012 jun;423(2):325–330.

[65] Kotnik T, Rems L, et al. Membrane Electroporation and Electropermeabilization: Mechanisms and Models. https://doiorg/101146/annurev-biophys-052118-115451. 2019 may;48:63–91.

[66] Ryttsén F, Farre C, et al. Characterization of Single-Cell Electroporation by Using Patch-Clamp and Fluorescence Microscopy. Biophysical Journal. 2000 oct;79(4):1993–2001.

[67] Hibino M, Itoh H, et al. Time courses of cell electroporation as revealed by submicrosecond imaging of transmembrane potential. Biophysical Journal. 1993 jun;64(6):1789–1800.

[68] Pavlin M, Leben V, et al. Electroporation in dense cell suspension–Theoretical and experimental analysis of ion diffusion and cell permeabilization. Biochimica et Biophysica Acta (BBA) - General Subjects. 2007 jan;1770(1):12–23.

[69] Ben-Or A, Rubinsky B. Experimental Studies on Irreversible Electroporation of Cells. 2010;p. 63–83.

[70] J T, MP R. Fusion of mammalian cells in culture is obtained by creating the contact between cells after their electropermeabilization. Biochemical and Biophysical Research Communications. 1986 oct;140(1):258–266.

[71] Tekle E, Astumian RD, et al. Electro-permeabilization of cell membranes: Effect of the resting membrane potential. Biochemical and Biophysical Research Communications. 1990 oct;172(1):282–287.

[72] Tekle E, Astumian RD, et al. Selective and asymmetric molecular transport across electroporated cell membranes. Proceedings of the National Academy of Sciences. 1994 nov;91(24):11512–11516.

[73] Prausnitz MR, Corbett JD, et al. Millisecond measurement of transport during and after an electroporation pulse. Biophysical Journal. 1995 may;68(5):1864–1870.

[74] Teruel MN, Meyer T. Electroporation-induced formation of individual calcium entry sites in the cell body and processes of adherent cells. Biophysical journal. 1997;73(4):1785–1796.

[75] Gabriel B, Teissié J. Direct observation in the millisecond time range of fluorescent molecule asymmetrical interaction with the electropermeabilized cell membrane. Biophysical Journal. 1997 nov;73(5):2630–2637.

[76] Neumann E, Toensing K, et al. Mechanism of Electroporative Dye Uptake by Mouse B Cells. Biophysical Journal. 1998 jan;74(1):98–108.

[77] Puc M, Kotnik T, et al. Quantitative model of small molecules uptake after in vitro cell electropermeabilization. Bioelectrochemistry. 2003 aug;60(1-2):1–10.

[78] Silve A, Guimerà Brunet A, et al. Comparison of the effects of the repetition rate between microsecond and nanosecond pulses: Electropermeabilization-induced electro-desensitization? Biochimica et Biophysica Acta (BBA) - General Subjects. 2014 jul;1840(7):2139–2151.

[79] Miklavčič D, Šemrov D, et al. A validated model of in vivo electric field distribution in tissues for electrochemotherapy and for DNA electrotransfer for gene therapy. Biochimica et Biophysica Acta - General Subjects. 2000 sep;1523(1):73–83.

[80] Voyer D, Silve A, et al. Dynamical modeling of tissue electroporation. Bioelectrochemistry. 2018 feb;119:98–110.

[81] Kos B, Miklavčič D. Numerical Modelling for Prediction and Evaluation of Treatment Outcome. In: Irreversible Electroporation in Clinical Practice. Cham: Springer International Publishing; 2018. p. 67–80.

[82] Fricke H. A Mathematical Treatment of the Electric Conductivity and Capacity of Disperse Systems ii. The Capacity of a Suspension

of Conducting Spheroids Surrounded by a Non-Conducting Membrane for a Current of Low Frequency. Physical Review. 1925 nov;26(5):678.

[83] Esser AT, Smith KC, et al. Towards solid tumor treatment by irreversible electroporation: Intrinsic redistribution of fields and currents in tissue. Technology in Cancer Research and Treatment. 2007 jun;6(4):261–273.

[84] Neal RE, Garcia PA, et al. Experimental Characterization and Numerical Modeling of Tissue Electrical Conductivity during Pulsed Electric Fields for Irreversible Electroporation Treatment Planning. IEEE Transactions on Biomedical Engineering. 2012 apr;59(4):1076–1085.

[85] Mir LM, Poignard C, et al. Dynamic Modeling of Electroporation for the Computation of the Electric Field Distribution Inside Biological Tissues during the Application of the Pulse Voltage. IFMBE Proceedings. 2016;53:211–214.

[86] Ivorra A, Villemejane J, et al. Electrical modeling of the influence of medium conductivity on electroporation. Physical Chemistry Chemical Physics. 2010 aug;12(34):10055.

[87] Šel D, Cukjati D, et al. Sequential finite element model of tissue electropermeabilization. IEEE Transactions on Biomedical Engineering. 2005 may;52(5):816–827.

[88] Beitel-White N, Bhonsle S, et al. Electrical Characterization of Human Biological Tissue for Irreversible Electroporation Treatments. In: Proceedings of the Annual International Conference of the IEEE Engineering in Medicine and Biology Society, EMBS. vol. 2018-July. Institute of Electrical and Electronics Engineers Inc.; 2018. p. 4170–4173.

[89] Davalos RV, Otten DM, et al. Electrical Impedance Tomography for Imaging Tissue Electroporation. IEEE Transactions on Biomedical Engineering. 2004 may;51(5):761–767.

[90] Pavšelj N, Bregar Z, et al. The course of tissue permeabilization

studied on a mathematical model of a subcutaneous tumor in small animals. IEEE Transactions on Biomedical Engineering. 2005;52(8):1373–1381.

[91] Šel D, Lebar AM, et al. Feasibility of employing model-based optimization of pulse amplitude and electrode distance for effective tumor electropermeabilization. IEEE Transactions on Biomedical Engineering. 2007 may;54(5):773–781.

[92] Cukjati D, Batiuskaite D, et al. Real time electroporation control for accurate and safe in vivo non-viral gene therapy. Bioelectrochemistry. 2007 may;70(2):501–507.

[93] Ivorra A, Al-Sakere B, et al. In vivo electrical conductivity measurements during and after tumor electroporation: conductivity changes reflect the treatment outcome. Physics in Medicine and Biology. 2009 oct;54(19):5949–5963.

[94] Miklavcic D, Snoj M, et al. Towards treatment planning and treatment of deep-seated solid tumors by electrochemotherapy. BioMedical Engineering Online. 2010 feb;9(1):1–12.

[95] Garcia PA, Rossmeisl JH, et al. A Parametric Study Delineating Irreversible Electroporation from Thermal Damage Based on a Minimally Invasive Intracranial Procedure. BioMedical Engineering OnLine. 2011 apr;10(1):34.

[96] Cima LF, Mir LM. Macroscopic characterization of cell electroporation in biological tissue based on electrical measurements. In: Applied Physics Letters. vol. 85; 2004. p. 4520–4522.

[97] Marčan M, Pavliha D, et al. Web-based tool for visualization of electric field distribution in deep-seated body structures and planning of electroporation-based treatments. BioMedical Engineering Online. 2015;14.

[98] Latouche EL, Sano MB, et al. Irreversible electroporation for the ablation of pancreatic malignancies: A patient-specific methodology. Journal of Surgical Oncology. 2017 may;115(6):711–717.

[99] Ivorra A, Mir LM, et al. Electric Field Redistribution due to Con-

ductivity Changes during Tissue Electroporation: Experiments with a Simple Vegetal Model. In: IFMBE Proceedings. vol. 25. Springer, Berlin, Heidelberg; 2009. p. 59–62.

[100] Ruarus AH, Vroomen LGPH, et al. Conductivity Rise During Irreversible Electroporation: True Permeabilization or Heat? CardioVascular and Interventional Radiology. 2018 aug;41(8):1257–1266.

[101] Edd JF, Davalos RV. Mathematical Modeling of Irreversible Electroporation for Treatment Planning. Technology in Cancer Research Treatment. 2007 aug;6(4):275–286.

[102] Sadiku MNO. A Simple Introduction to Finite Element Analysis of Electromagnetic Problems. IEEE Transactions on Education. 1989;32(2):85–93.

[103] Beitel-White N, Lorenzo MF, et al. Multi-Tissue Analysis on the Impact of Electroporation on Electrical and Thermal Properties. IEEE Transactions on Biomedical Engineering. 2021 mar;68(3):771–782.

[104] Gallinato O, de Senneville BD, et al. Numerical modelling challenges for clinical electroporation ablation technique of liver tumors. Mathematical Modelling of Natural Phenomena. 2020;15:11.

[105] Amann D, Blaszczyk A, et al. Simulation of floating potentials in industrial applications by boundary element methods. Journal of Mathematics in Industry 2014 4:1. 2014 oct;4(1):1–15.

[106] Sale AJH, Hamilton WA. Effects of high electric fields on microorganisms: III. Lysis of erythrocytes and protoplasts. Biochimica et Biophysica Acta (BBA) - Biomembranes. 1968 aug;163(1):37–43.

[107] Miller L, Leor J, et al. Cancer cells ablation with irreversible electroporation. Technology in Cancer Research and Treatment. 2005 dec;4(6):699–705.

[108] Peleg M. Advanced quantitative microbiology for foods and biosystems: models for predicting growth and inactivation. CRC Press; 2006.

[109] Golberg A, Rubinsky B. A statistical model for multidimensional irreversible electroporation cell death in tissue. BioMedical Engineering OnLine. 2010 feb;9(1):13.

[110] Peleg M. A model of microbial survival after exposure to pulsed electric fields. Journal of the Science of Food and Agriculture. 1995 jan;67(1):93–99.

[111] Canatella PJ, Karr JF, et al. Quantitative study of electroporation-mediated molecular uptake and cell viability. Biophysical Journal. 2001 feb;80(2):755–764.

[112] Yang Y, Moser MAJJ, et al. Development of a statistical model for cervical cancer cell death with irreversible electroporation in vitro. PLOS ONE. 2018 apr;13(4):e0195561.

[113] Garcia PA, Kos B, et al. Predictive therapeutic planning for irreversible electroporation treatment of spontaneous malignant glioma. Medical Physics. 2017 sep;44(9):4968–4980.

[114] Ding L, Moser M, et al. Treatment Planning Optimization in Irreversible Electroporation for Complete Ablation of Variously Sized Cervical Tumors: A Numerical Study. Journal of Biomechanical Engineering. 2021 jan;143(1).

[115] Pintar M, Langus J, et al. Time-Dependent Finite Element Analysis of In Vivo Electrochemotherapy Treatment. Technology in Cancer Research Treatment. 2018 jan;17:153303381879051.

[116] Aycock KN, Zhao Y, et al. A Theoretical Argument for Extended Interpulse Delays in Therapeutic High-Frequency Irreversible Electroporation Treatments. IEEE Transactions on Biomedical Engineering. 2021 jun;68(6):1999–2010.

[117] Pennes HH. Analysis of Tissue and Arterial Blood Temperatures in the Resting Human Forearm. Journal of Applied Physiology. 1948 aug;1(2):93–122.

[118] Mir LM, Orlowski S. Mechanisms of electrochemotherapy. Advanced Drug Delivery Reviews. 1999 jan;35(1):107–118.

[119] Sersa G, Miklavcic D, et al. Electrochemotherapy in treatment of tumours. European Journal of Surgical Oncology. 2008 feb;34(2):232–240.

[120] Sadadcharam M, Soden DM, et al. Electrochemotherapy: an emerging cancer treatment. International journal of hyperthermia. 2008;24(3):263–273.

[121] Clover AJP, Salwa SP, et al. Electrochemotherapy for the treatment of primary basal cell carcinoma; A randomised control trial comparing electrochemotherapy and surgery with five year follow up. European Journal of Surgical Oncology. 2020 may;46(5):847–854.

[122] Orlowski S, Belehradek J, et al. Transient electropermeabilization of cells in culture: Increase of the cytotoxicity of anticancer drugs. Biochemical Pharmacology. 1988 dec;37(24):4727–4733.

[123] Serša G, Čemažar M, et al. Antitumor Effectiveness of Electrochemotherapy with cis-Diamminedichloroplatinum(II) in Mice. Cancer Research. 1995;55(15).

[124] Mir LM. Bases and rationale of the electrochemotherapy. European Journal of Cancer Supplements. 2006 nov;4(11):38–44.

[125] Bianchi G, Campanacci L, et al. Electrochemotherapy in the Treatment of Bone Metastases: A Phase II Trial. World Journal of Surgery 2016 40:12. 2016 jul;40(12):3088–3094.

[126] Edhemovic I, Brecelj E, et al. Intraoperative electrochemotherapy of colorectal liver metastases. Journal of Surgical Oncology. 2014 sep;110(3):320–327.

[127] Edhemovic I, Gadzijev EM, et al. Electrochemotherapy: A New Technological Approach in Treatment of Metastases in the Liver:. http://dxdoiorg/107785/tcrt2012500224. 2016 jun;10(5):475–485.

[128] Granata V, Fusco R, et al. Electrochemotherapy in locally advanced pancreatic cancer: Preliminary results. International Journal of Surgery. 2015 jun;18:230–236.

[129] Klein N, Gunther E, et al. Prostate cancer infiltrating the bladder sphincter successfully treated with Electrochemotherapy: a case report. Clinical Case Reports. 2017 dec;5(12):2127.

[130] Linnert M, Agerholm-Larsen B, et al. Treatment of Brain Tumors: Electrochemotherapy. Springer, Dordrecht; 2014. p. 247–259.

[131] Groselj A, Kos B, et al. Coupling treatment planning with navigation system: a new technological approach in treatment of head and neck tumors by electrochemotherapy. BioMedical Engineering OnLine 2015 14:3. 2015 aug;14(3):1–14.

[132] Egeland C, Baeksgaard L, et al. Endoscopic electrochemotherapy for esophageal cancer: a phase I clinical study. Endoscopy International Open. 2018 may;06(06):E727–E734.

[133] Hansen HF, Bourke M, et al. Electrochemotherapy for colorectal cancer using endoscopic electroporation: a phase 1 clinical study. Endoscopy International Open. 2020 jan;08(02):E124–E132.

[134] Mahmood F, Gehl J. Optimizing clinical performance and geometrical robustness of a new electrode device for intracranial tumor electroporation. Bioelectrochemistry. 2011 apr;81(1):10–16.

[135] Pavliha D, Kos B, et al. Patient-specific treatment planning of electrochemotherapy: Procedure design and possible pitfalls. Bioelectrochemistry. 2012 oct;87:265–273.

[136] Marcan M, Pavliha D, et al. Segmentation of hepatic vessels from MRI images for planning of electroporation-based treatments in the liver. Radiology and Oncology. 2014 sep;48(3):267.

[137] Maglietti F, Tellado M, et al. Minimally Invasive Electrochemotherapy Procedure for Treating Nasal Duct Tumors in Dogs using a Single Needle Electrode. Radiology and Oncology. 2017;51(4):422.

[138] Mir LM, Bureau MF, et al. High-efficiency gene transfer into skeletal muscle mediated by electric pulses. Proceedings of the National Academy of Sciences. 1999 apr;96(8):4262–4267.

[139] Mir LM, Moller PH, et al. Electric PulseâMediated Gene Delivery to Various Animal Tissues. Advances in Genetics. 2005 jan;54:83–114.

[140] Gothelf A, Gehl J. Gene Electrotransfer to Skin; Review of Existing Literature and Clinical Perspectives. Current Gene Therapy. 2010 jul;10(4):287–299.

[141] Luján E, Marino M, et al. Towards an optimal dose-response relationship in gene electrotransfer protocols. Electrochimica Acta. 2019 oct;319:1002–1011.

[142] Pavlin M, Kandušer M. New Insights into the Mechanisms of Gene Electrotransfer â Experimental and Theoretical Analysis. Scientific Reports 2015 5:1. 2015 mar;5(1):1–11.

[143] Rosazza C, Haberl Meglic S, et al. Gene Electrotransfer: A Mechanistic Perspective. Current Gene Therapy. 2016;16(2):98–129.

[144] Pasquet L, Chabot S, et al. Safe and efficient novel approach for non-invasive gene electrotransfer to skin. Scientific Reports 2018 8:1. 2018 nov;8(1):1–13.

[145] Martin RCG, McFarland K, et al. Irreversible electroporation in locally advanced pancreatic cancer: Potential improved overall survival. Annals of Surgical Oncology. 2013 dec;20(3 SUPPL.):443–449.

[146] Silk M, Tahour D, et al. The state of irreversible electroporation in interventional oncology. Seminars in interventional radiology. 2014 jun;31(2):111–7.

[147] Van Den Bos W, Scheffer HJ, et al. Thermal Energy during Irreversible Electroporation and the Influence of Different Ablation Parameters. Journal of Vascular and Interventional Radiology. 2016 mar;27(3):433–443.

[148] Cannon R, Ellis S, et al. Safety and early efficacy of irreversible electroporation for hepatic tumors in proximity to vital structures. Journal of Surgical Oncology. 2013 apr;107(5):544–549.

[149] rossmeisl Jr J, paulo Garcia, et al. Safety and feasibility of the NanoKnife system for irreversible electroporation ablative treatment of canine spontaneous intracranial gliomas. J Neurosurg laboratory iNvestigatioN J Neurosurg. 2015;123(123):1008–1025.

[150] Haemmerich D, Staelin ST, et al. ¡i¿In vivo¡/i¿ electrical conductivity of hepatic tumours. Physiological Measurement. 2003 may;24(2):251–260.

[151] Deodhar A, Monette S, et al. Percutaneous irreversible electroporation lung ablation: Preliminary results in a porcine model. CardioVascular and Interventional Radiology. 2011 dec;34(6):1278–1287.

[152] Martin RCG, Kwon D, et al. Treatment of 200 Locally Advanced (Stage III) Pancreatic Adenocarcinoma Patients With Irreversible Electroporation. Annals of Surgery. 2015 sep;262(3):486–494.

[153] Meijerink MR, Nilsson A, et al. Irreversible Electroporation of Pancreatic Tumors. In: Irreversible Electroporation in Clinical Practice. Cham: Springer International Publishing; 2018. p. 167–190.

[154] Guenther E, Klein N, et al. Prostate cancer treatment with Irreversible Electroporation (IRE): Safety, efficacy and clinical experience in 471 treatments. PLOS ONE. 2019 apr;14(4):e0215093.

[155] Ansari D, Kristoffersson S, et al. The role of irreversible electroporation (IRE) for locally advanced pancreatic cancer: a systematic review of safety and efficacy. Scandinavian Journal of Gastroenterology. 2017 nov;52(11):1165–1171.

[156] Miklovic T, Latouche EL, et al. A Comprehensive Characterization of Parameters Affecting High-Frequency Irreversible Electroporation Lesions. Annals of Biomedical Engineering. 2017 nov;45(11):2524–2534.

[157] Siddiqui IA, Kirks RC, et al. High-Frequency Irreversible Electroporation: Safety and Efficacy of Next-Generation Irreversible Electroporation Adjacent to Critical Hepatic Structures. Surgical Innovation. 2017 jun;24(3):276–283.

[158] Mercadal B, Beitel-White N, et al. Dynamics of Cell Death After Conventional IRE and H-FIRE Treatments. Annals of Biomedical Engineering. 2020 may;48(5):1451–1462.

[159] Rogers WR, Merritt JH, et al. Strength-duration curve an electrically excitable tissue extended down to near 1 nanosecond. IEEE Transactions on Plasma Science. 2004 aug;32(4 II):1587–1599.

[160] Arena CB, Sano MB, et al. High-frequency irreversible electroporation (H-FIRE) for non-thermal ablation without muscle contraction. BioMedical Engineering OnLine. 2011;10.

[161] Sano MB, Fan RE, et al. Reduction of Muscle Contractions during Irreversible Electroporation Therapy Using High-Frequency Bursts of Alternating Polarity Pulses: A Laboratory Investigation in an ExÂ Vivo Swine Model. Journal of Vascular and Interventional Radiology. 2018 jun;29(6):893–898.e4.

[162] Sano MB, Fan RE, et al. Asymmetric Waveforms Decrease Lethal Thresholds in High Frequency Irreversible Electroporation Therapies. Scientific Reports 2017 7:1. 2017 jan;7(1):1–13.

[163] Sano MB, DeWitt MR, et al. Optimization of a single insertion electrode array for the creation of clinically relevant ablations using high-frequency irreversible electroporation. Computers in Biology and Medicine. 2018 apr;95:107–117.

[164] Dong S, Wang H, et al. First Human Trial of High-Frequency Irreversible Electroporation Therapy for Prostate Cancer:. https://doiorg/101177/1533033818789692. 2018 jul;17.

[165] Latouche EL, Arena CB, et al. High-Frequency Irreversible Electroporation for Intracranial Meningioma: A Feasibility Study in a Spontaneous Canine Tumor Model:. https://doiorg/101177/1533033818785285. 2018 aug;17.

[166] Van Es R, Konings MK, et al. High-frequency irreversible electroporation for cardiac ablation using an asymmetrical waveform. BioMedical Engineering Online. 2019 jun;18(1):1–13.

[167] J L, G O, et al. A novel nonthermal energy source for surgical epicardial atrial ablation: irreversible electroporation. The Heart Surgery Forum. 2007 jan;10(2):E162–7.

[168] Neven K, van Driel V, et al. Epicardial linear electroporation ablation and lesion size. Heart Rhythm. 2014 aug;11(8):1465–1470.

[169] Hong J, Stewart MT, et al. Cardiac ablation via electroporation.

Proceedings of the 31st Annual International Conference of the IEEE Engineering in Medicine and Biology Society: Engineering the Future of Biomedicine, EMBC 2009. 2009;p. 3381–3384.

[170] Sugrue A, Maor E, et al.. Irreversible electroporation for the treatment of cardiac arrhythmias. Taylor and Francis Ltd; 2018.

[171] Wojtaszczyk A, Caluori G, et al. Irreversible electroporation ablation for atrial fibrillation. Journal of Cardiovascular Electrophysiology. 2018 apr;29(4):643–651.

[172] Phillips M, Rubinsky L, et al. Combining Electrolysis and Electroporation for Tissue Ablation:. https://doiorg/101177/1533034614560102. 2014 nov;14(4):395–410.

[173] Stehling MK, Guenther E, et al. Synergistic Combination of Electrolysis and Electroporation for Tissue Ablation. PLOS ONE. 2016 feb;11(2):e0148317.

[174] Lv Y, Zhang Y, et al. Molecular and histological study on the effects of electrolytic electroporation on the liver. Bioelectrochemistry. 2019 feb;125:79–89.

[175] Klein N, Guenther E, et al. Single exponential decay waveform; a synergistic combination of electroporation and electrolysis (E2) for tissue ablation. PeerJ. 2017 apr;5(4):e3190.

[176] Klein N, Mercadal B, et al. In vitro study on the mechanisms of action of electrolytic electroporation (E2). Bioelectrochemistry. 2020 jun;133:107482.

[177] Widesott L, Pierelli A, et al. Intensity-modulated proton therapy versus helical tomotherapy in nasopharynx cancer: planning comparison and NTCP evaluation. International journal of radiation oncology, biology, physics. 2008 oct;72(2):589–96.

[178] Good D, Lo J, et al. A Knowledge-Based Approach to Improving and Homogenizing Intensity Modulated Radiation Therapy Planning Quality Among Treatment Centers: An Example Application to Prostate Cancer Planning. International Journal of Radiation Oncology*Biology*Physics. 2013 sep;87(1):176–181.

[179] Wang MH, Ji Y, et al. Impact Factors for Microinvasion in Patients With Hepatocellular Carcinoma: Possible Application to the Definition of Clinical Tumor Volume. International Journal of Radiation Oncology*Biology*Physics. 2010 feb;76(2):467–476.

[180] Weiss E, Hess CF. The Impact of Gross Tumor Volume (GTV) and Clinical Target Volume (CTV) Definition on the Total Accuracy in Radiotherapy. Strahlentherapie und Onkologie 2003 179:1. 2003 jan;179(1):21–30.

[181] Pavliha D, Mušič MM, et al. Electroporation-based treatment planning for deep-seated tumors based on automatic liver segmentation of MRI images. PloS one. 2013 aug;8(8):e69068.

[182] Rhim H, Lee MH, et al. Planning Sonography to Assess the Feasibility of Percutaneous Radiofrequency Ablation of Hepatocellular Carcinomas. American Journal of Roentgenology. 2008 may;190(5):1324–1330.

[183] Malicki J. The importance of accurate treatment planning, delivery, and dose verification. Urban and Partner; 2012.

[184] Villard C, Soler L, et al. Radiofrequency ablation of hepatic tumors: simulation, planning, and contribution of virtual reality and haptics. Computer Methods in Biomechanics and Biomedical Engineering. 2005 aug;8(4):215–227.

[185] Zupanic A, Kos B, et al. Treatment planning of electroporation-based medical interventions: Electrochemotherapy, gene electrotransfer and irreversible electroporation. Physics in Medicine and Biology. 2012 sep;57(17):5425–5440.

[186] Schumann C, Rieder C, et al. Interactive multi-criteria planning for radiofrequency ablation. International Journal of Computer Assisted Radiology and Surgery. 2015 jun;10(6):879–889.

[187] Yang Y, Moser M, et al. Optimization of Electrode Configuration and Pulse Strength in Irreversible Electroporation for Large Ablation Volumes Without Thermal Damage. Journal of Engineering and Science in Medical Diagnostics and Therapy. 2018 jan;1(2):021002.

[188] Puc M, Rebersek S, et al. Requirements for a clinical electrochemotherapy device-electroporator. RADIOLOGY AND ONCOLOGY. 1997;31:368–373.

[189] Marty M, Sersa G, et al. Electrochemotherapy â An easy, highly effective and safe treatment of cutaneous and subcutaneous metastases: Results of ESOPE (European Standard Operating Procedures of Electrochemotherapy) study. European Journal of Cancer Supplements. 2006 nov;4(11):3–13.

[190] Simčič P, Lowe R, et al. Electrochemotherapy in treatment of canine oral non-tonsillar squamous cell carcinoma. A case series report. Veterinary and Comparative Oncology. 2020 sep;18(3):428–432.

[191] Miklavcic D, Semrov D, et al. In vivo electroporation threshold determination. In: Annual International Conference of the IEEE Engineering in Medicine and Biology - Proceedings. vol. 4; 2000. p. 2815–2818.

[192] Al-Sakere B, André F, et al. Tumor Ablation with Irreversible Electroporation. PLoS ONE. 2007 nov;2(11):e1135.

[193] Davalos RV, Rubinsky B. Temperature considerations during irreversible electroporation. International Journal of Heat and Mass Transfer. 2008 nov;51(23-24):5617–5622.

[194] Garcia PA, Rossmeisl JH, et al. Pilot study of irreversible electroporation for intracranial surgery. In: 2009 Annual International Conference of the IEEE Engineering in Medicine and Biology Society. IEEE; 2009. p. 6513–6516.

[195] Dollinger M, Zeman F, et al. Bile Duct Injury after Irreversible Electroporation of Hepatic Malignancies: Evaluation of MR Imaging Findings and Laboratory Values. Journal of Vascular and Interventional Radiology. 2016 jan;27(1):96–103.

[196] van den Bos W, de Bruin DM, et al. MRI and contrast-enhanced ultrasound imaging for evaluation of focal irreversible electroporation treatment: results from a phase I-II study in patients undergoing IRE followed by radical prostatectomy. European Radiology 2015 26:7. 2015 oct;26(7):2252–2260.

[197] den Bos W, De Bruin DM, et al. The correlation between the electrode configuration and histopathology of irreversible electroporation ablations in prostate cancer patients. World journal of urology. 2016;34(5):657–664.

[198] Campelo S, Valerio M, et al. An evaluation of irreversible electroporation thresholds in human prostate cancer and potential correlations to physiological measurements. APL Bioengineering. 2017 dec;1(1):016101.

[199] Neal RE, Millar JL, et al. In vivo characterization and numerical simulation of prostate properties for non-thermal irreversible electroporation ablation. The Prostate. 2014 may;74(5):458–468.

[200] Thomson KR, Kavnoudias H, et al. Introduction to Irreversible Electroporation–Principles and Techniques. Techniques in Vascular and Interventional Radiology. 2015 sep;18(3):128–134.

[201] Ruarus AH, Barabasch A, et al. Irreversible Electroporation for Hepatic Tumors: Protocol Standardization Using the Modified Delphi Technique. Journal of Vascular and Interventional Radiology. 2020 nov;31(11):1765–1771.e15.

[202] Jarm T, Krmac T, et al. Investigation of safety for electrochemotherapy and irreversible electroporation ablation therapies in patients with cardiac pacemakers. BioMedical Engineering OnLine 2020 19:1. 2020 nov;19(1):1–18.

[203] Gong L, Yao C, et al. The optimization of the treatment planning for achieving complete ablation of tumor during irreversible electroporation by genetic algorithm. In: 2017 IEEE 21st International Conference on Pulsed Power (PPC). IEEE; 2017. p. 1–6.

[204] Wang L, Wu H, et al. Region-based image segmentation with local signed difference energy. Pattern Recognition Letters. 2013 apr;34(6):637–645.

[205] Ghosh P, Mitchell M, et al. Incorporating priors for medical image segmentation using a genetic algorithm. Neurocomputing. 2016 jun;195:181–194.

[206] Niedworok CJ, Brown APY, et al. aMAP is a validated pipeline for registration and segmentation of high-resolution mouse brain data. Nature Communications 2016 7:1. 2016 jul;7(1):1–9.

[207] Yushkevich PA, Piven J, et al. User-guided 3D active contour segmentation of anatomical structures: Significantly improved efficiency and reliability. NeuroImage. 2006 jul;31(3):1116–1128.

[208] Wolf I, Vetter M, et al. The Medical Imaging Interaction Toolkit. Medical Image Analysis. 2005 dec;9(6):594–604.

[209] Kikinis R, Pieper SD, et al. 3D Slicer: A Platform for Subject-Specific Image Analysis, Visualization, and Clinical Support. Intraoperative Imaging and Image-Guided Therapy. 2014;p. 277–289.

[210] Kankaanpää P, Paavolainen L, et al. BioImageXD: an open, general-purpose and high-throughput image-processing platform. Nature Methods 2012 9:7. 2012 jun;9(7):683–689.

[211] de Chaumont F, Dallongeville S, et al. Icy: an open bioimage informatics platform for extended reproducible research. Nature Methods 2012 9:7. 2012 jun;9(7):690–696.

[212] Pereira S, Pinto A, et al. Brain Tumor Segmentation Using Convolutional Neural Networks in MRI Images. IEEE Transactions on Medical Imaging. 2016 may;35(5):1240–1251.

[213] Moeskops P, Viergever MA, et al. Automatic Segmentation of MR Brain Images with a Convolutional Neural Network. IEEE Transactions on Medical Imaging. 2016 may;35(5):1252–1261.

[214] Havaei M, Davy A, et al. Brain tumor segmentation with Deep Neural Networks. Medical Image Analysis. 2017 jan;35:18–31.

[215] Christ PF, Elshaer MEA, et al. Automatic Liver and Lesion Segmentation in CT Using Cascaded Fully Convolutional Neural Networks and 3D Conditional Random Fields. Lecture Notes in Computer Science (including subseries Lecture Notes in Artificial Intelligence and Lecture Notes in Bioinformatics). 2016 oct;9901 LNCS:415–423.

[216] Gordienko Y, Gang P, et al. Deep Learning with Lung Segmentation and Bone Shadow Exclusion Techniques for Chest X-Ray Analysis of Lung Cancer. Advances in Intelligent Systems and Computing. 2018 jan;754:638–647.

[217] Yu L, Yang X, et al. Volumetric ConvNets with mixed residual connections for automated prostate segmentation from 3D MR images. In: Thirty-first AAAI conference on artificial intelligence. AAAI press; 2017. p. 66–72.

[218] Roth HR, Lu L, et al. DeepOrgan: Multi-level Deep Convolutional Networks for Automated Pancreas Segmentation. Lecture Notes in Computer Science (including subseries Lecture Notes in Artificial Intelligence and Lecture Notes in Bioinformatics). 2015;9349:556–564.

[219] Fu M, Wu W, et al. Hierarchical combinatorial deep learning architecture for pancreas segmentation of medical computed tomography cancer images. BMC Systems Biology 2018 12:4. 2018 apr;12(4):119–127.

[220] Cai J, Lu L, et al. Improving Deep Pancreas Segmentation in CT and MRI Images via Recurrent Neural Contextual Learning and Direct Loss Function. 2017 jul;.

[221] Prasoon A, Petersen K, et al. Deep Feature Learning for Knee Cartilage Segmentation Using a Triplanar Convolutional Neural Network. Lecture Notes in Computer Science (including subseries Lecture Notes in Artificial Intelligence and Lecture Notes in Bioinformatics). 2013;8150 LNCS(PART 2):246–253.

[222] Wolterink JM, Leiner T, et al. Automatic Coronary Calcium Scoring in Cardiac CT Angiography Using Convolutional Neural Networks. Lecture Notes in Computer Science (including subseries Lecture Notes in Artificial Intelligence and Lecture Notes in Bioinformatics). 2015;9349:589–596.

[223] Trullo R, Petitjean C, et al. Joint Segmentation of Multiple Thoracic Organs in CT Images with Two Collaborative Deep

Architectures. Lecture Notes in Computer Science (including subseries Lecture Notes in Artificial Intelligence and Lecture Notes in Bioinformatics). 2017;10553 LNCS:21–29.

[224] Zhou X, Takayama R, et al. Deep learning of the sectional appearances of 3D CT images for anatomical structure segmentation based on an FCN voting method. Medical Physics. 2017 oct;44(10):5221–5233.

[225] Gallinato O, de Senneville BD, et al. Numerical workflow of irreversible electroporation for deep-seated tumor. Physics in Medicine Biology. 2019 mar;64(5):055016.

[226] Mahnič-Kalamiza S, Kotnik T, et al. Educational application for visualization and analysis of electric field strength in multiple electrode electroporation. BMC Medical Education. 2012 dec;12(1):102.

[227] Marino M, Luján E, et al. OpenEP : an open-source simulator for electroporation-based tumor treatments. Scientific Reports 2021 11:1. 2021 jan;11(1):1–15.

[228] Pavliha D, Kos B, et al. Planning of Electroporation-Based Treatments Using Web-Based Treatment-Planning Software. 2013 nov;246(11):833–842.

[229] Thorwarth D, Geets X, et al.. Physical radiotherapy treatment planning based on functional PET/CT data; 2010.

[230] Zhang L, Hub M, et al. Software for quantitative analysis of radiotherapy: Overview, requirement analysis and design solutions. Computer Methods and Programs in Biomedicine. 2013 jun;110(3):528–537.

[231] Jin C, He Z, et al. MRI-based finite element simulation on radiofrequency ablation of thyroid cancer. Computer Methods and Programs in Biomedicine. 2014 feb;113(2):529–538.

[232] Polak A, Bonhenry D, et al. On the electroporation thresholds of lipid bilayers: Molecular dynamics simulation investigations. Journal of Membrane Biology. 2013;246(11):843–850.

[233] Schroeder W, Martin K, et al. The visualization toolkit, 4th edn. Kitware. New York. 2006;.

[234] The CGAL Project. CGAL User and Reference Manual. 4th ed. CGAL Editorial Board; 2013.

[235] Alliez P, Rineau L, et al. 3D Mesh Generation. In: CGAL User and Reference Manual. 4th ed. CGAL Editorial Board; 2013. .

[236] Paul Chew L. Constrained delaunay triangulations. Algorithmica. 1989 jun;4(1-4):97–108.

[237] Sugrue A, Vaidya V, et al. Irreversible electroporation for catheter-based cardiac ablation: a systematic review of the preclinical experience. Journal of Interventional Cardiac Electrophysiology 2019 55:3. 2019 jul;55(3):251–265.

[238] Garcia PA, Rossmeisl JH, et al. Intracranial nonthermal irreversible electroporation: In vivo analysis. Journal of Membrane Biology. 2010 jul;236(1):127–136.

[239] Neal RE, Davalos RV. The feasibility of irreversible electroporation for the treatment of breast cancer and other heterogeneous systems. Annals of Biomedical Engineering. 2009 dec;37(12):2615–2625.

[240] Sharabi S, Kos B, et al. A statistical model describing combined irreversible electroporation and electroporation-induced blood-brain barrier disruption. Radiology and Oncology. 2016;.

[241] Schindelin J, Arganda-Carreras I, et al.. Fiji: An open-source platform for biological-image analysis. Nature Publishing Group; 2012.

[242] Schneider CA, Rasband WS, et al.. NIH Image to ImageJ: 25 years of image analysis. Nature Publishing Group; 2012.

[243] Sankur B. Survey over image thresholding techniques and quantitative performance evaluation. Journal of Electronic Imaging. 2004 jan;13(1):146.

[244] Bernsen J. Dynamic Thresholding of Gray Level Image. In: Proceedings of International Conference on Pattern Recognition. Berlin; 1986. p. 1251–1255.

[245] Wilkinson M. Automated and manual segmentation techniques in image analysis of microbes. In: Digital Image Analysis of Microbes: Imaging, Morphometry, Fluorometry and Motility Techniques and Applications. John Wiley Sons; 1998. .

[246] Perera-Bel E, Yagüe C, et al. EView: An electric field visualization web platform for electroporation-based therapies. Computer Methods and Programs in Biomedicine. 2020 dec;197:105682.

[247] R Core Team. R: A Language and Environment for Statistical Computing. Vienna, Austria; 2021.

[248] Dobson AJ, Barnett AG. An introduction to generalized linear models. CRC press; 2018.

[249] Taha AA, Hanbury A. Metrics for evaluating 3D medical image segmentation: Analysis, selection, and tool. BMC Medical Imaging. 2015 aug;15(1):29.

[250] Yao C, Lv Y, et al. Irreversible electroporation ablation area enhanced by synergistic high- and low-voltage pulses. PLOS ONE. 2017 mar;12(3):e0173181.

[251] Marszalek P, Liu DS, et al. Schwan equation and transmembrane potential induced by alternating electric field. Biophysical Journal. 1990 oct;58(4):1053–1058.

[252] Serša G, Čemažar M, et al. Changing electrode orientation improves the efficacy of electrochemotherapy of solid tumors in mice. Bioelectrochemistry and Bioenergetics. 1996 feb;39(1):61–66.

[253] Kim HB, Sung CK, et al. Changes of apoptosis in tumor tissues with time after irreversible electroporation. Biochemical and Biophysical Research Communications. 2013 jun;435(4):651–656.

[254] Guo Y, Zhang Y, et al. Irreversible electroporation therapy in the liver: Longitudinal efficacy studies in a rat model of hepatocellular carcinoma. Cancer Research. 2010 feb;70(4):1555–1563.

[255] Weinert R, Pereira E, et al. Inclusion of memory effects in a dynamic model of electroporation in biological tissues. Artificial Organs. 2019 jul;43(7):688–693.

[256] Ramos A, Weinert RL. Mathematical and computational method for electrical analysis of biological tissues. Journal of Computational Electronics. 2018 mar;17(1):382–391.

[257] Leguèbe M, Silve A, et al. Conducting and permeable states of cell membrane submitted to high voltage pulses: Mathematical and numerical studies validated by the experiments. Journal of Theoretical Biology. 2014 nov;360:83–94.

[258] Langus J, Kranjc M, et al. Dynamic finite-element model for efficient modelling of electric currents in electroporated tissue. Scientific Reports. 2016 sep;6(1):26409.

[259] Zhao Y, Zheng S, et al. Development of a Multi-Pulse Conductivity Model for Liver Tissue Treated With Pulsed Electric Fields. Frontiers in Bioengineering and Biotechnology. 2020 may;0:396.

[260] Carr JC, Richard Fright W, et al. Surface interpolation with radial basis functions for medical imaging. IEEE Transactions on Medical Imaging. 1997;16(1):96–107.

[261] Field DA. Laplacian smoothing and Delaunay triangulations. Communications in Applied Numerical Methods. 1988 nov;4(6):709–712.

[262] Maleike D, Nolden M, et al. Interactive segmentation framework of the Medical Imaging Interaction Toolkit. Computer Methods and Programs in Biomedicine. 2009 oct;96(1):72–83.

[263] McCormick MM, Liu X, et al. ITK: enabling reproducible research and open science. Frontiers in Neuroinformatics. 2014 feb;0(FEB):13.

[264] Yoo TS, Ackerman MJ, et al. Engineering and Algorithm Design for an Image Processing API: A Technical Report on ITK - the Insight Toolkit. Studies in Health Technology and Informatics. 2002;85:586–592.

[265] Zhao Y, Bhonsle S, et al. Characterization of conductivity changes during high-frequency irreversible electroporation for treatment planning. IEEE Transactions on Biomedical Engineering. 2018 aug;65(8):1810–1819.

[266] Davalos RV, Rubinsky B, et al. Theoretical analysis of the thermal effects during in vivo tissue electroporation. Bioelectrochemistry. 2003 oct;61(1-2):99–107.

[267] Partridge BR, O'Brien TJ, et al. High-Frequency Irreversible Electroporation for Treatment of Primary Liver Cancer: A Proof-of-Principle Study in Canine Hepatocellular Carcinoma. Journal of Vascular and Interventional Radiology. 2020 mar;31(3):482–491.e4.

[268] O'Brien TJ, Passeri M, et al. Experimental High-Frequency Irreversible Electroporation Using a Single-Needle Delivery Approach for Nonthermal Pancreatic Ablation In Vivo. Journal of Vascular and Interventional Radiology. 2019 jun;30(6):854–862.e7.

[269] Geddes LA, Baker LE. The specific resistance of biological material–A compendium of data for the biomedical engineer and physiologist. Medical and biological engineering 1967 5:3. 1967 may;5(3):271–293.

[270] Adeyanju OO, Al-Angari HM, et al. The optimization of needle electrode number and placement for irreversible electroporation of hepatocellular carcinoma. Radiology and Oncology. 2012 jun;46(2):126.

[271] Gabriel C. Compilation of the Dielectric Properties of Body Tissues at RF and Microwave Frequencies.; 1996.

[272] Hasgall PA, Di Gennaro F, et al. IT'IS Database for thermal and electromagnetic parameters of biological tissues, Version 4.0. IT'IS. 2018;.

[273] Qasrawi R, Silve L, et al. Anatomically Realistic Simulations of Liver Ablation by Irreversible Electroporation: Impact of Blood Vessels on Ablation Volumes and Undertreatment:. https://doiorg/101177/1533034616687477. 2017 jan;16(6):783–792.

[274] Dunki-Jacobs EM, Philips P, et al. Evaluation of thermal injury to liver, pancreas and kidney during irreversible electroporation in an in vivo experimental model. British Journal of Surgery. 2014 aug;101(9):1113–1121.

List of publications

Journal papers

Perera-Bel E, Yagüe C, Mercadal B, Ceresa M, Beitel-White N, Davalos RV, González Ballester MA, Ivorra A. EView: An electric field visualization web platform for electroporation-based therapies. *Computer Methods and Programs in Biomedicine*. 2020; 197:105682.
DOI: 10.1016/j.cmpb.2020.105682
URL: *https://doi.org/10.1016/j.cmpb.2020.105682*

Perera-Bel E, Mercadal B, García-Sánchez T, González Ballester MA, Ivorra A. Modeling methods for treatment planning in overlapping electroporation treatments. *IEEE Transactions on Biomedical Engineering*. 2021.
DOI: 10.1109/TBME.2021.3115029
URL: *https://doi.org/10.1109/TBME.2021.3115029*

Minguillon J, Tudela-Pi J, Becerra-Fajardo L, **Perera-Bel E**, del-Ama AJ, Gil-Agudo A, Megía-García A, García-Moreno A, Ivorra A. Powering electronic implants by high frequency volume conduction: in human validation [Under review]

Perera-Bel E, Aycock KN, Salameh ZS, Davalos RV, Ivorra A, González Ballester MA. A platfrom for patient-specific treatment planning in electroporation-based therapies [In preparation]

Conference and workshop presentations

Perera-Bel E, Ivorra A, González Ballester MA. Platfrom for treatment planning in irreversible electroporation therapy. *Workshop on Electroporation-Based Technologies and Treatments*. Ljubljana, Slovenia, 2018. Poster and oral presentation.

Perera-Bel E, Ivorra A, González Ballester MA. A platform for irreversible electroporation treatment planning. *33rd International Congress on Computer Assisted Radiology and Surgery*. Rennes, France, 2019. Oral presentation.

Perera-Bel E, Beitel-White N, Mercadal B, Davalos RV, González Ballester MA, Ivorra A. A web platform for 3D simulation of electroporation-based treatments in homogeneous tissues. *3rd World Congress on Electroporation and Pulsed Electric Fields in Biology, Medicine and Food & Environmental Technologies*. Toulouse, France, 2019. Oral presentation.